SCALABLE MANUFACTURING OF FLEXIBLE ELECTRONIC SYSTEMS AND SMART TEXTILES

by

Marina Sala de Medeiros

A Dissertation

Submitted to the Faculty of Purdue University

In Partial Fulfillment of the Requirements for the degree of

Doctor of Philosophy

School of Industrial Engineering

West Lafayette, Indiana

August 2021

THE PURDUE UNIVERSITY GRADUATE SCHOOL
STATEMENT OF COMMITTEE APPROVAL

Dr. Ramses V. Martinez, Chair

School of Industrial Engineering and Weldon School of Biomedical Engineering

Dr. Juan Wachs

School of Industrial Engineering

Dr. Jacqueline Linnes

Weldon School of Biomedical Engineering

Dr. Lia Stanciu-Gregory

School of Materials Engineering

Approved by:

Dr. Abhijit Deshmukh

Dedicated to my mom for her unconditional support and encouragement.

ACKNOWLEDGMENTS

This document is the fruit of years of guidance and support of many great people I have met at Purdue and around the world. First, I want to thank my advisor Dr. Ramses Martinez for the opportunity to join his lab. Prof. Martinez has shaped my research profile to be attentive to details and challenged me to always perform better. I am grateful for all the research discussions and material we designed and built as a team. His guidance led me to become a rigorous and ambitious researcher and I will treasure the countless hours spent in his office amending figures and text before submitting my papers.

A sincere thanks to my thesis committee members, Dr. Juan Wachs, Dr. Lia Stanciu-Gregory, and Dr. Jacqueline Linnes. Dr. Juan Wachs readily agreed to help me towards graduation and provided me with insightful directions towards better usability of wearable devices. I would like to thank Dr. Lia Stanciu-Gregory for teaching me so much about biomaterials at Purdue and during a study abroad in Spain. I would also like to thank her for the emotional support during my journey at Purdue. A special dedication to Dr. Jacqueline Linnes for reviewing and discussing my preliminary results, carefully reviewing my thesis, and giving me the opportunity to join her lab after the PhD. I hope this is the start of a beautiful collaboration!

I would like to acknowledge all the lab members and exchange students I met at FlexiLab. Aniket, Ben and Deb for their collaboration and friendship throughout my PhD. 'Gracias' to Vanessa for inviting me to collaborate with her on new projects, and for all the supportive and insightful conversations we have had since she joined the lab. I also wanted to thank EIA University (Colombia, Medellin) for their exchange program with FlexiLab. I had opportunity to mentor and eventually become friends with some of their students including Daniela Chanci, Carolina, Daniela Arias and Maria del Mar. They brought so much energy to all the lab, worked hard and I will cherish those warm moments. I am grateful to the countless friends at Purdue that made and still make me feel I have a family while being far away from my relatives.

I am also grateful for Prof. Morin's guidance and financial support towards most of my PhD. I highly appreciated his trust, the late-night hours grading together with him, friendship, and I knew I could 100% count on him and his wife Susan. I will forever remember him, and together with me, multiple generations of Industrial Engineering students he passionately educated.

I would like to thank Dr. Patrick Brunese (Doc B) for his support and recognition of my teaching efforts and skills while teaching graduate and undergraduate students at the School of Industrial Engineering. I would like to acknowledge the Flex Lab staff members, Reid Schmidt and Dr. Dave Kish, for always promptly answering any requests I had for the lab, to ensure a safe and nice laboratory environment for all students at Flex Lab, the friendly laughter and small talk that would make my day.

I am extremely grateful to my mother, Sonia Maria Sala de Medeiros, for her unconditional love, wonderful friendship and for teaching me the values of education and humility from early on. She would have loved reading these lines, and she is missed every day of my life. ‘Obrigada’ to my father, Orivaldo Baptista de Medeiros (aka Toco), my brother, Marcos Sala de Medeiros, my favorite cousins (Fernanda, Fabio, Bruno and Gabriel), and all of my extended family. They gave me the confidence to achieve my goals and ensured their support wherever I end up. Finally, ‘bedankt’ or ‘merci’ to my husband, Prof. James Braun for bringing me so much joy and for making me part of his wonderful family. We met when we were both PhD students, it all started with some soup with wine, and I could not be prouder of all we have achieved since then.

TABLE OF CONTENTS

LIST OF TABLES 10
LIST OF FIGURES 11
ABSTRACT 14
1. INTRODUCTION 16
1.1 Motivation 16
1.2 Structure of the document 17
1.3 Background and Literature Review 17
1.3.1 Paper Electronics 17
1.3.2 Smart Textiles 18
1.3.3 Challenges in Powering Printable Electronics and Smart Textiles 18
1.3.4 Novel Self-powered Approaches for Powering Printable Electronics and Smart Textiles 19
1.3.5 Need for Triboelectric Nanogenerators as Power-sources for Printable Electronics and Smart Textiles 20
1.3.6 Wireless Power Transfer Technologies as Power-sources for Smart Textiles 21
2. MOISTURE-INSENSITIVE, SELF-POWERED PAPER-BASED FLEXIBLE ELECTRONICS 23
2.1 Introduction 23
2.2 Materials and Methods 25
2.2.1 Fabrication of R^F-SPEs 25
2.2.2 Charge separation and triboelectric performance of TENGs printed on R^F-SPEs 26
2.2.3 Characterization of wettability of different papers using fluorinated and non-fluorinated silanes 29
2.2.4 Rapid printing of flexible R^F-SPE keypads 30
2.2.5 Rectification of the triboelectric voltage and current peaks generated in R^F-SPEs 31
2.2.6 Analog signal acquisition and wireless signal processing 33
2.2.7 Pressure sensitivity of the R^F-SPE keypad 33
2.2.8 Stability of R^F-SPEs upon washing and drying. 35
2.2.9 Triboelectric areas in the R^F-SPEs wireless music player 35

2.2.10 Fabrication costs 36
2.3 Results and Discussion 38
2.3.1 Design and fabrication of R^F-SPEs 38
2.3.2 Resistance to Fold Damage 40
2.3.3 Dependence of the triboelectric performance on the type of paper and silane used to fabricate the R^F-SPEs 40
2.3.4 Conversion of Mechanical Energy into Electric Energy using C_{12}^F-treated RF-SPEs 42
2.3.5 R^F-SPEs as human-machine interfaces—flexible keypad 45
2.3.6 R^F-SPEs as human-machine interfaces—wireless music player 47
2.4 Conclusions 49
3. WATERPROOF, BREATHABLE, AND ANTIBACTERIAL SELF-POWERED E-TEXTILES BASED ON OMNIPHOBIC TRIBOELECTRIC NANOGENERATORS 50
3.1 Introduction 50
3.2 Materials and Methods 51
3.2.1 Fabrication of the R^F-TENGs 51
3.2.2 Bacterial Quantification Assay 53
3.2.2.1 Bacterial Incubation 53
3.2.2.2 Luminescence Measurements 53
3.2.2.3 Quantification of Colony Forming Units 53
3.2.2.4 Statistical Analysis 54
3.2.3 Scanning Electron Microscopy 54
3.2.4 Characterization of Wettability of Different Textiles Using Polar and Non-polar Solvents 55
3.2.5 Effect of Relative Humidity on the Performance of R^F-TENGs. 57
3.2.6 Production and Storage of Electric Energy Using R^F-TENGs 58
3.2.7 Fabrication of Self-Powered Human-Machine Interfaces based on R^F-TENGs 61
3.2.8 Analog Signal Acquisition and Signal Processing 62
3.2.9 Fabrication Cost 63
3.3 Results and Discussion 64
3.3.1 Design and Fabrication of R^F-TENGs 64

3.3.2 Working Principle of Flexible and Stretchable R^F-TENGs. 68
3.3.3 Conversion of Mechanical Energy into Electric Energy using R^F-TENGs 69
3.3.4 Stain Repellency and Machine-Washing Resistance of R^F-TENGs 72
3.3.5 Harvesting Biomechanical Energy using R^F-TENGs 74
3.3.6 R^F-TENGs as Human-Machine Interfaces 77
3.4 Conclusions 79
4. WASHABLE, BREATHABLE, AND STRETCHABLE E-TEXTILES WIRELESSLY POWERED BY OMNIPHOBIC SILK-BASED COILS 80
4.1 Introduction 80
4.2 Materials and Methods 81
4.2.1 Fabrication of OSCs using SF/MWCNTs/ChC Microfibers 81
4.2.2 Structural Characterization of OSCs and Omniphobic E-textiles 86
4.2.2.1 Scanning Electron Microscopy 86
4.2.2.2 Fourier-Transform Infrared Spectroscopy 87
4.2.3 Mechanical Characterization of OSCs 87
4.2.4 Electrical Characterization of OSCs 90
4.2.5 Safety of Use of OSC-based e-textiles with respect to Human Exposure to Electromagnetic Fields 92
4.2.6 OSC-powered wearable non-contact voltage detector 93
4.2.7 Wireless, Battery-free, PPG Wristband 96
4.2.8 Fabrication Costs 98
4.3 Results and Discussion 99
4.3.1 Design and Fabrication of OSCs 99
4.3.2 Materials Characterization of OSCs 100
4.3.3 Working Principle of Flexible and Stretchable OSCs 102
4.3.4 Electrical Characterization of OSCs 104
4.3.5 Battery-free, Wirelessly-powered, Photoplethysmography Wristband 106
4.3.6 Wearable Non-contact Voltage Detection Glove 107
4.4 Conclusions 110
5. CONCLUSIONS 111
REFERENCES 114

PUBLICATIONS 130

LIST OF TABLES

Table 1. Itemized cost of the silanization and printing of wireless R^F-SPE keypads.....37

Table 2. Itemized cost of the silanization and printing of the wireless R^F-SPE music player.....37

Table 3. Bill of materials to fabricate R^F-TENGs 63

Table 4. Itemized cost of 6.25 cm^2 R^F-TENGs.....64

Table 5. Power and power density levels of OSC-based e-textiles, and maximum allowed safe power density level according to IEEE standard for safety with respect to human exposure to electromagnetic fields (1–30MHz). 93

Table 6. Itemized cost of the materials needed to fabricate OSCs. These prices correspond to small quantities and could be further reduced by volume discounts. 98

LIST OF FIGURES

Figure 2.1 Fibrous structure of paper substrates rendered omniphobic by silanization with C_{12}^F. 26

Figure 2.2 RF-SPE displaying "Purdue" by powering 48 SMD LEDs with the triboelectric energy generated from human-interaction. 28

Figure 2.3. Open-circuit voltage peaks generated by gently tapping the TENGs printed over the surface of R^F-SPEs treated with a fluorinated silane (C_{12}^F) and a non-fluorinated silane (C_1^H). ..29

Figure 2.4 S4. Images of NiNPs conductive electrodes spray-deposited through a stencil on C_{12}^F-silanized and unmodified Whatman #1 paper substrate. 30

Figure 2.5 Stencil mask and resulting conductive layout of the flexible R^F-SPE keypad. a) Image and dimensions of stencil mask obtained by laser cutting transparency films with a CO_2 laser cutter. 31

Figure 2.6 Rectification of the open-circuit voltages generated by tapping a 6.25 cm^2 triboelectric area in a C_{12}^F-treated R^F-SPE. 32

Figure 2.7 Rectification of the short-circuit currents generated by tapping a 6.25 cm^2 triboelectric area in a C_{12}^F-treated R^F-SPE. 32

Figure 2.8 Pressure sensitivity of the flexible R^F-SPE keypad shown in Figure 2.15. 34

Figure 2.9. Self-powered, paper-based, wireless R^F-SPE keypad. 34

Figure 2.10 Stability of the maximum open-circuit voltage and short-circuit current peaks generated by the 0-9 keys of R^F-SPE keypad shown in Figure 2.15 after 50 cleaning cycles. 35

Figure 2.11 Self-powered, paper-based, wireless R^F-SPE music player interface. 36

Figure 2.12 Process to fabricate R^F-SPEs on a single sheet of paper. 39

Figure 2.13 Foldability and silane dependence of the triboelectric performance of R^F-SPEs. 42

Figure 2.14 Production and storage of electric energy in C_{12}^F-treated R^F-SPEs. 44

Figure 2.15 Flexible and wireless R^F-SPE keypad. 46

Figure 2.16 Wireless R^F-SPE music player interface. 48

Figure 3.1 Embroidery process steps for the top layer of the R^F-TENG. 52

Figure 3.2 Wetting characterization of cotton rendered omniphobic using C_{12}^F organosilane. 56

Figure 3.3 Stability of R^F-TENGs to prolonged immersion in water. 56

Figure 3.4 Open-circuit voltage and short-circuit current characteristics of 2.25 cm^2 R^F-TENGs at different values of relative humidity and a constant temperature T = 22 ± 1 °C. 57

Figure 3.5. Production and storage of electric energy using different R^F-TENG sizes and capacitors with different capacitances. 59

Figure 3.6. Charging curves of a 2 mF capacitor embedded in R^F-TENGs of different sizes (I- cherry design ~2.25 cm^2; II- fish design ~4.5 cm^2; III- cat design ~6.25 cm^2) fabricated in cotton, after 50 cycles of standard machine washing. 60

Figure 3.7 Voltage peaks generated by tapping R^F-TENGs (area = 6.25 cm^2) made with different fabrics: 61

Figure 3.8 Layers of the audio control interface described in Figure 3.14. Right side of the collar: 62

Figure 3.9 Fabric-based R^F-TENG fabrication process. 66

Figure 3.10 Production of electric energy and bacteria repellency of omniphobic e-textiles powered by R^F-TENGs. 69

Figure 3.11 Production of electric energy using a 6.25 cm^2 R^F-TENG. 71

Figure 3.12 Washing durability of e-textiles powered by R^F-TENGs. 74

Figure 3.13 Biomechanical energy harvesting using R^F-TENGs. 76

Figure 3.14 Self-powered audio control interface based on R^F-TENGs. 78

Figure 4.1. Serpentine design used in the fabrication of OSCs. 82

Figure 4.2 a) Image of the thread tension mechanism used to keep the SF/MWCNT/ChC thread at ~4 N tension during sewing. b) Image of the thread as it travels through a stitch, showing how the low sewing tension reduces the bending experienced by the conductive thread as it is sewn on the textile. 83

Figure 4.3 High-resolution SEM images of the fibers of a cotton textile rendered omniphobic by silanization with C_{12}^F 84

Figure 4.4 Covalent modifications of OSC and e-textile fibers [128]. 85

Figure 4.5 Gas permeability of an omniphobic OSC-powered e-textile (smart glove shown in Figure 4.16d and e, Figure 4.20c and d). 86

Figure 4.6 Comparison between the FTIR spectra of SF/MWCNTs/ChC microfibers and pure silk microfibers. 87

Figure 4.7 Stress-strain curves generated during the tensile testing of eight different 100-mm-long OSC threads. 88

Figure 4.8 Stretchability and bendability of omniphobic OSC-based e-textiles. 89

Figure 4.9 Schematics of the experimental set-up used to maintain the OSC axis collinear with the primary coil during the stretching characterization experiments. 90

Figure 4.10 Frequency-dependent electrical characteristics of the wirelessly powered OSC-based e-textile (acquired passively from the primary coil side) shown in Figure 4.17b: 91

Figure 4.12 Image of the primary coil used for MRC WPT with OSCs presented in this work. ..92

Figure 4.12 Laundry resistance of the wearable non-contact voltage detection glove. 95

Figure 4.14. Dependence of voltage detected with the non-contact voltage detection glove shown in Figure 4.22 and Figure 4.13 on its separation from the cable before (a) and after (b) 50 cleaning cycles. 96

Figure 4.14 Information extractable from the PPG waveforms collected with the wearable OSC-based PPG sensor (single cardiac cycle). 97

Figure 4.15. OSC-powered PPG wristband. 98

Figure 4.16 Process to fabricate OSC-powered e-textiles. 100

Figure 4.17 Materials characterization of the SF/MWCNTs/ChC thread.....102

Figure 4.18 Stretchability and water repellency of OSC-powered omniphobic e-textiles. 104

Figure 4.19 Electrical Characterization of the WPT performance of OSC-based e-textiles. 105

Figure 4.20 OSC-powered PPG wristband. 107

Figure 4.21 OSC-powered wearable non-contact voltage detector. 109

ABSTRACT

The transition from conventional rigid and battery-based electronics into flexible and self-powered circuitry will pave the way toward future wearable technologies. Flexible electronics, when fabricated using low-cost materials and mass production technologies, will be able to augment the functionality of everyday items, enhancing the way humans interact with machines. Unfortunately, the manufacturing approaches commonly used to prototype and fabricate flexible electronics are often based on materials and processes appropriate for rigid electronics. Expanding the range of low-cost materials, scalable fabrication techniques, and lightweight and wireless powering strategies applicable to flexible electronics will be desirable to lower current manufacturing barriers.

Paper, due to its low cost, biodegradability, and availability 10^{12} tons of cellulose are produced annually), has gained considerable attention as a substrate for the development of printable electronics. These paper-based devices are flexible and even foldable, facilitating their conformability to other objects, and their use in a variety of applications, from packaging to healthcare. Similarly, the ubiquitous use of textiles in daily life and the recent miniaturization of electronic systems fostered the development of a fast-growing interdisciplinary research field that aims to incorporate wearable electronics into garments. These electronic textiles—called "e-textiles"—have demonstrated to serve as convenient platforms for personalized medicine and human-machine interfacing.

Several energy harvesting and wireless power transfer approaches have been proposed as lightweight and flexible alternatives to power e-textiles and paper-based devices. Triboelectric nanogenerators (TENGs)—capable of converting user-device interaction into electrical outputs via contact electrification—have been explored as a battery-less strategy to power wearable devices. Wireless power transmission (WPT) using resonant inductive coupling has also demonstrated to be a promising strategy to continuously power e-textiles in closed environments without significantly increasing their rigidity or weight.

This PhD dissertation focuses on the development of new cost-effective and scalable methods to design and manufacture self-powered paper-based electronics and to transform conventional fabrics into e-textiles. The resulting low-cost flexible electronics and wearables are

lightweight, insensitive to moisture, and compatible with large-scale production processes, serving as a foundation for the future development and commercialization of smart garments and paper-based electronics devices that do not depend on batteries for their use.

1. INTRODUCTION

1.1 Motivation

Paper-based electronics benefits from their mechanically flexible nature, low-cost, and environmental friendliness to enable the creation of low-power, lightweight and multifunctional electronics. Ideally, these paper-based electronics can be rapidly fabricated by simple ubiquitous printing processes and used as a platform to expand the development of the internet of things (IoT). Unfortunately, the widespread use of printed paper-based electronics is limited by the hygroscopic nature of cellulose paper and the tendency of paper to absorb solvents, which induces the wicking of inks through its thickness, reducing the lateral resolution of the printing process and causing the short-circuit of electrical connections when printed on both sides of the paper. To expand the use of paper-based printed electronics, there is a need for the development of cost-effective methods to fabricate insensitive to environmental moisture electronics without affecting both the mechanical and electrical performance of these printed paper-based electronics.

Smart textiles, similarly, due to their mechanically flexible nature, low-cost, and ubiquitous presence in daily lives, enable the creation of novel wearable technologies such as human-machine interfaces[1,2] and multifunctional wearable sensors[3,4]. Expanding the functionality of this smart garments while maintaining their look, feel, safety, and washability are currently active fronts of research at the academia and industry levels.[5] The approaches for fabricating these smart textiles, however, are mostly dependent on complex and manual processes that are not compatible with current textile industry technologies. The development of scalable manufacturing processes to create e-textiles using low-cost materials would lead to the ubiquitous expansion of this technology.

The range of applications of flexible paper-based electronics and smart textiles is hindered by their dependence on conventional and uncomfortable batteries. While several electrochemical and lithium-based approaches have been proposed to fabricate rechargeable paper-based or wearable batteries capable of effectively power low-cost electronic devices [6,7], the materials required are often costly and environmentally harmful [8]. Additionally, the active components of these batteries require proper encapsulation [8] to avoid moisture-induced short-circuits and to prevent the decrease in performance caused by their rapid degradation when exposed to air when made of paper. The thickness of this encapsulation often compromises the flexibility, foldability

and practical usage of these batteries, hampering their applicability towards flexible paper-based electronics and smart textiles [9]. Thus, the practical adoption of these technologies would benefit from new cost-effective solutions to power flexible electronics without compromising their bendability and large-scale fabrication capabilities.

1.2 Structure of the document

My PhD dissertation is organized as follows: Chapter 1 introduces the research, describes its significance, and provides the reader with a literature review on the design, fabrication, and powering of paper-based electronics and smart textiles. Chapter 2 describes the development of self-powered and moisture-insensitive paper-based electronic devices. Chapters 3 describe the manufacturing of washable and self-powered smart garment and 4 describes a sewing process to create e-textiles that can be wirelessly powered using wireless power transfer. Finally, Chapter 5 summarizes the conclusions and future applications of the work developed in this dissertation.

1.3 Background and Literature Review

1.3.1 Paper Electronics

The great development of printable electronics in the recent years has demonstrated a cost-effective alternative path for the fabrication of electronics,[10,11] sensors,[12,13] and microfluidic devices[14–16] using paper, PDMS, and other polymers as a substrate.[17,18] Paper-based electronics—electronics using cellulose paper as a substrate—have raised as an excellent candidate to fabricate green and low-cost user interfaces and devices that can be easily disposed with a minimal generation of solid byproducts [18,19]. The low weight and thickness of these paper-based devices make them flexible and even foldable, facilitating their conformability to other objects [20,21], and their use as smart packaging [22,23]. Unfortunately, the hygroscopic nature of cellulose paper promotes the rapid degradation of both the mechanical and electrical performance of paper-based electronics in environments with high relative humidity [24]. Moreover, the tendency of paper to absorb solvents induces the wicking of inks through its thickness, reducing the lateral resolution of the printing process and causing the short-circuit of electrical connections when printed on both sides of the paper. While several electrochemical and lithium-based approaches have been proposed to fabricate rechargeable paper-based batteries capable of effectively power low-cost

electronic devices [6,7], the materials required are often costly and environmentally harmful. Additionally, the active components of these paper-based batteries require proper encapsulation to avoid moisture-induced short-circuits and to prevent the decrease in performance caused by their rapid degradation when exposed to air. The thickness of this encapsulation often compromises the flexibility and foldability of these paper-based batteries, hampering their applicability [9]. The development of new scalable and low-cost methods to fabricate self-powered paper-based electronics insensitive to environmental moisture would therefore be desirable to promote the commercialization and ubiquitous adoption of paper-based human-machine interfaces.

1.3.2 Smart Textiles

The ubiquity of textiles in daily life and the recent miniaturization of electronic systems using flexible substrates have led to a fast-growing and advanced interdisciplinary research field that aims to incorporate wearable devices into electronic textiles called "e-textiles" [25–27]. E-textiles have demonstrated to serve as convenient platforms for human-machine interfacing [1,2], the embedding of wearable sensors [3,4], and the development of conformable robotic sensory skin [28]. While e-textiles are commonly powered using conventional rechargeable batteries, their weight and rigidity often compromise the bendability and stretchability of the textile, reducing the comfort of the user. To circumvent this limitation, several researchers have demonstrated the fabrication of flexible, fiber-shaped batteries such as coaxial or twinned yarn-like Li-ion [29] and Zn-ion [30] rechargeable batteries equipped with bendable carbon or metal-based anodes. Unfortunately, these fiber-shaped batteries require to be encapsulated to prevent the evaporation and leakage of their liquid electrolytes, incrementing their radius and making them difficult to interface with conventional sewing equipment [8]. Simple and scalable methods to transform conventional garments or textiles into comfortable, washable, and battery-independent e-textiles would be desirable to enable the expansion of a new generation of wearable devices and human-machine interfaces.

1.3.3 Challenges in Powering Printable Electronics and Smart Textiles

The recent miniaturization of electronic systems into wearable devices and IoT (Internet of Things) have increased the amount of devices embedded in printable electronics and smart textiles,

augmenting their energy consumption and making this technologies highly dependent on the development of lightweight rechargeable batteries as a sustainable power source.[31–33] Several methods have been explored to print flexible batteries to power printable electronics. However, these batteries are often expensive and require complex manufacturing processes.[3] Similarly, the use of batteries to power e-textiles is often perceive as uncomfortable by the user and require frequent re-charging, limiting the usage time and the adoption of this emerging technology.[34] To address these energy problems, a variety of energy harvesting mechanisms have been proposed to continuously power paper electronics and e-textiles by converting the energy scavenged from the environment or the user into electric energy, or by creating mechanisms to provide power wirelessly by wireless power transfer.[35–38]

1.3.4 Self-Powering Approaches for Printable Electronics and Smart Textiles

Several flexible photovoltaic systems,[39,40] photoactive materials,[41] and fibrous perovskite solar cells[42] have been proposed to use sunlight to power paper electronics and e-textiles.[33,42] Unfortunately, environmental limitations such as night-time, cloudy days, or dimly illuminated rooms significantly reduce power generation efficiency and continuity, frequently hampering e-textile and printed electronics applications. Thermoelectric effects have been exploited to continuously supply power to e-textiles by converting thermal gradients in the textile into electric energy.[43–45] Similarly, flexible pyroelectric generators have exploited the pyroelectric effect to harvest energy from temperature fluctuations due to thermal diffusion.[46,47] At the typical temperature gradients generated between the human body and the environment, thermoelectric generators have demonstrated a better performance powering e-textiles than pyroelectric materials.[27] The difficulty to obtain flexible and high-performance thermoelectric materials, however, has led to the fabrication of thermoelectric generators consisting of a large number of thermoelectric units connected in series or parallel, compromising the flexibility and comfort of the e-textile.[48]

The conversion of the biomechanical energy—generated during the natural motion of the wearer or the interaction of the user with the electronics—into electrical energy has attracted increasing attention as a strategy to power e-textiles and other electronics carried by the user.[15,49–51] Exploiting the piezoelectric effect, several piezoelectric materials (such as safe and stable ZnO

nanowires or polyvinylidene difluoride, PVDF, fibers) have been layered or directly grown onto conductive electrodes to fabricate piezoelectric generators.[2,52,53] The high-output voltage performance of flexible piezoelectric generators has enabled their use not only to power wearable[52,54] and implantable[55,56] devices, but also as self-powered biosensors to monitor respiration[57,58] and arterial pulse.[58,59] Unfortunately, piezoelectric generators often require complex fabrication processes that are not favorable for continuous production.[2,47,54] Additionally, the prolonged exposure of piezoelectric materials and metal wire electrodes to moisture can deteriorate the performance of the piezoelectric generators,[47] limiting their practical utility in e-textile and paper electronics applications.

Flexible and lightweight wireless power systems have emerged as an ideal battery-free strategy to power e-textiles [60,61]. Radio frequency identification (RFID) antennas have been extensively attached to consumable products [62,63], textiles [64], and even human skin as a cost-effective approach for the real-time collection of wireless measurements [65]. The relatively low distance range of operation of RFID technology, however, has limited its applicability to continuously powering wearables and e-textiles. Additionally, the laminating materials often required to protect RFID antennas and circuits from oxidation hamper the breathability of these sensors [64].

1.3.5 Triboelectric Nanogenerators as Power-sources for Printable Electronics and Smart Textiles

Exploiting the triboelectric effect, triboelectric nanogenerators (TENGs) are capable of converting mechanical energy into electrical energy using triboelectrification and electrostatic induction.[31,66] TENGs have been used as energy harvesters,[66–68] self-powered sensors,[17,66,69,70] and power sources for low-power electronics and wearable devices.[3,49,71] When compared with other energy harvesting devices, TENGs offer several advantages, such as high efficiency, large output power, low cost, excellent reliability, and the compatibility with a wide range of materials and simple fabrication processes.[18,72,73] TENGs with multilayered electrodes demonstrated to effectively provide steady and high output power to paper electronics and to the smart garments to which they are attached.[74–76] Unfortunately, the non-porous film materials commonly used to fabricate multilayered TENGs and the elastomeric encapsulation typically used to protect them from environmental moisture often limit the breathability of the textiles.[3,77] Additionally, the high output

voltage produced by multilayered TENGs is frequently achieved by nanotexturizing the triboelectric interface where contact electrification occurs, which significantly increases the complexity and production costs of these paper-based or e-textiles TENGs.[78]

Previous examples of TENGs using paper and other porous materials have been proposed to power low-power electronics,[79–81] however, the tendency of paper to absorb solvents limits its usage for powering portable paper-based electronic devices in which humidity have deleterious effect on the mechanical and electrical properties. Moreover, the hygroscopic nature of the paper makes conductive inks to wick through the paper during the printing process, impeding isolated electrical connections to be printed on both sides of the paper. For textiles, other researches explored entwining fibers of opposite triboelectric polarities to enable the fabrication of flexible textile-based TENGs with high air permeability but limited stretchability.[31] Recently, coaxial fiber-shaped TENGs—comprising an electropositive core fiber, conducting nanomaterials, and a highly electronegative coating layer—have demonstrated higher stability under continuous bending and stretching than entwined or two-fiber twisted TENGs.[31,82,83] Unfortunately, due to the hygroscopic nature of many textiles, environmental moisture and the sweat of the wearer promote bacterial proliferation[84] and compromise the electrical output of textile-based TENGs.[85] The mechanical damage caused by repetitive usage and washing also exacerbates the efficiency of fiber-based TENGs.[86] Furthermore, the radius of the yarns often utilized in textile-based TENGs are greater than the ones used in traditional embroidery, therefore making them difficult to manufacture using industrial embroidery systems.[83]

1.3.6 Wirelessly Powering Strategies for Smart Textiles

RFID antennas power a variety of sensor attached to textiles and other consumable products [62,64]. Unfortunately, due to their low distance of operation, this technology finds challenging the continuous powering of e-textiles, particularly when the wearer is moving. Wireless power transmission (WPT) using resonant inductive coupling has demonstrated to be a promising strategy to continuously power e-textiles without significantly increasing their rigidity or weight [87,88]. To maximize WPT efficiency, the coils embedded into e-textiles require to both exhibit low ohmic losses and match the impedance of the external resonant coil [89,90]. Several nanomaterial-based inks with high electrical conductivity have been used to rapidly pattern—*via* inkjet [91,92] or screen

printing [93,94]—WPT 2D coils over the surface of different e-textiles. While these conductive inks exhibit a high degree of flexibility and adhesion to the surface of fibrous textiles, the prolonged exposure of e-textiles to mechanical strains from wearer use often cause ink cracking and delamination, compromising WPT performance [95]. Silk fibroin protein, due to its biocompatibility, low-cost, and high mechanical strength and toughness, has served as support and reinforcement for conductive nanomaterials in a variety of stretchable wearable sensors [96,97], biodegradable thread-like conductors [98], and transient implantable electronics [99,100]. Unfortunately, the degradation of silk fibroin composites after prolonged contact with water has limited their application in washable e-textiles.[101] To benefit from the intrinsic flexibility and stretchability of textiles, a variety of thread-based WPT coils incorporating highly conductive metallic filaments have been directly knitted [102], embroidered [103], or sewn [104,105] onto e-textiles. Unfortunately, the hygroscopic behavior of most textiles and garments makes the metallic components of these thread-based coils susceptible to moisture-induced corrosion in humid environments, upon contact with the sweat of the user, or during washing cycles [104]. A rapid, cost-effective, and scalable process to transform conventional fabrics into e-textiles would therefore be desirable to accelerate the development and commercialization of smart garments that do not depend on batteries for their power and are robust enough to be washed with everyday laundry.

Along this thesis, I will describe scalable fabrication strategies for the development of self-powered and moisture-insensitive paper-based electronic devices, and then apply those strategies to the manufacturing of washable and self-powered smart garments, exploiting WPT using sewn coils as an efficient strategy to power e-textiles.

2. MOISTURE-INSENSITIVE, SELF-POWERED PAPER-BASED FLEXIBLE ELECTRONICS

Motivation and rationale: The fabrication of multifunctional electronic devices on ubiquitous paper substrates is gaining considerable attention due to their low cost, environmental friendliness, light weight, and flexibility. Unfortunately, the development of paper-based electronics is subject to significant challenges, such as rapid degradation with moisture, battery dependence, and limited compatibility with existing mass production technologies. This work describes omniphobic, self-powered paper-based electronics (R^F-SPEs), completely wireless paper-based electronic devices insensitive to moisture, liquid stains, and dust. R^F-SPEs can be rapidly fabricated through the sequential spray-deposition of alkylated organosilanes, conductive nanoparticles, polytetrafluoroethylene (strong electron affinity), and ethyl cellulose (weak electron affinity) over the surface of cellulose paper. R^F-SPEs are lightweight, inexpensive to print (<$0.25 per device), and capable of generating power densities up to 300 $\mu W/cm^2$. Additionally, R^F-SPEs are flexible and exhibit excellent stability upon folding (0.3 mm radius of curvature). The simple printing process and relative low cost of R^F-SPEs enable the large-scale production of self-powered paper-based electronics towards the ubiquitous integration of human-machine interfaces.

2.1 Introduction

Several approaches have been proposed to mitigate the battery dependence of paper-based electronics. Paper-based solar cells built by combining transparent cellulose nanofibrils with thin perovskite [23,107], dye-sensitized [108,109], or thin silicon films [110,111] have demonstrated to successfully power printed electronics using sunlight. Unfortunately, the use of paper-based solar cells in dimly illuminated rooms, at nighttime, or on cloudy days leads to inconsistent power generation, which compromises the efficient and continuous operation of portable electronics. Piezoelectric energy harvesters, capable of generating electricity during the mechanical stress induced by the user, have demonstrated to serve as an efficient power source for portable electronic devices [52,112,113]. Particularly, biologically safe and stable piezoelectric materials such as ZnO nanorods or

polypropylene piezoelectrets have been deposited on paper to fabricate paper-based piezoelectric nanogenerators exhibiting superior charge scavenging performance and high thermal stability [114]. The cost and complexity of the processes required to produce flexible films of piezoelectric nanomaterials, however, limit their application in low-cost paper-based electronics [115]. Triboelectric nanogenerators (TENGs)—devices capable of converting mechanical energy from the user or the environment into electricity by coupling triboelectrification and electrostatic induction—have gained considerable interest as a potential self-powered alternative to operate wearable devices [116]. Several paper-based TENGs have been proposed to harvest energy, efficiently and at a low cost, from a variety of sources, including human body motions [51,117], wind [118], and acoustic waves [119,120]. While the flexibility [121], and foldability [81] of paper-based TENGs makes them ideal to power flexible electronics and wearable devices, the fabrication methods used to make paper-based TENGs are often not suitable for large scale manufacturing [122]. Additionally, the prolonged exposure of paper, piezoelectric materials, and printed electrodes to environmental moisture often degrade the performance of paper-based solar cells, piezoelectric generators, and TENGs, limiting their practical utility as power sources for portable and wearable electronics in settings with high relative humidity [3,77].

Here, we propose a scalable and cost-effective fabrication method to create the first moisture-insensitive, self-powered, paper-based flexible electronics (R^F-SPEs). R^F-SPEs are easy to design and rapid to fabricate by the sequential spray-deposition of alkylated organosilanes, ethyl cellulose (EC), conductive nickel nanoparticles (NiNPs), and polytetrafluoroethylene (PTFE). We demonstrate that R^F-SPEs are lightweight, foldable, and capable of powering other paper-mounted electronics using the electrostatic energy harvested from their interaction with the user. The omniphobic surface of R^F-SPEs enables the rapid cleaning of these devices by simply wiping them with a paper towel or running them under a stream of water to remove solid residues. The high output power densities of the triboelectric areas in R^F-SPEs enable single touch-based wireless data transmission, paving the way towards the use of R^F-SPEs in a variety of low-cost, self-powered human-machine interfaces.

2.2 Materials and Methods

2.2.1 Fabrication of R^F-SPEs

We fabricated the R^F-SPEs on the following commercially available paper substrates: Whatman #1, Whatman #50, Blot (all from GE Healthcare Inc.), and copy paper procured from Boise Inc. We placed these papers on top of a hot plate at 85 °C, inside a chemical hood, and silanized them by spraying, with an airbrush at a pressure of 1.5 to 2.0 psi, a 5% v/v solution of alkylated silane in isopropanol, which evaporated from the surface of the paper in ~1 min.

The following alkylated silanes were used in this study (all procured from Gelest Inc. and used without further purification):

i) tricholoromethylsilane (CH_3SiCl_3; "C_1^H"),

ii) trichlorodecylsilane ($CH_3(CH_2)_9SiCl_3$; "C_{10}^H"),

iii) Trichloro(3,3,4,4,5,5,6,6,7,7,8,8,8-tridecafluorooctyl)silane ($CF_3(CF_2)_5CH_2$-CH_2SiCl_3; "C_8^F"),

iv) trichloro(3,3,4,4,5,5,6,6,7,7,8,8,9,9,10,10,10-heptadecafluorodecyl)silane ($CF_3(CF_2)_7CH_2$-CH_2SiCl_3; "C_{10}^F"),

v) trichloro(3,3,4,4,5,5,6,6,7,7,8,8,9,9,10,10,11,11,12,12,12-henicosafluorododecyl)silane ($CF_3(CF_2)_9CH_2$-CH_2SiCl_3; "C_{12}^F").

We fabricated stencil masks by laser cutting transparency films (VWO100C-BE; Apollo Inc.) with a CO_2 laser cutter (MT3050D; Morntech Inc.). We used the stencil masks to print the conductive layout of the R^F-SPEs by spraying a ~10-µm-thick layer of PTFE (20% v/v solution of PTFE-N UV in N-Ethyl-2-Pyrrolidone, both from Molykote Inc.) and a ~10-µm-thick layer of NiNPs (7440-02-0; Sigma Aldrich Inc.). We incorporated triboelectric areas to power the R^F-SPEs by sequentially spraying the conductive electrodes with a ~10-µm-thick layer of Ethyl cellulose (9004-57-3; Sigma Aldrich Inc.), a ~10-µm-thick layer of NiNPs, and applying a final coat with the silanizing solution. Waiting for 1 min between each spray deposition ensures the complete drying of the deposited layers. On the opposite side of the R^F-SPE, we printed visual guidelines to facilitate human-interaction using a conventional inkjet printer (HP Deskjet 2540 series). We attached the electronic SMD components to the R^F-SPE using electrically conductive epoxy (AA-DUCT 902; Atom Adhesives Inc.).

We used high-resolution SEM (scanning electron microscope) images of silanized paper to investigate potential changes in the structure of the cellulose fibers after spraying the papers with the silanizing solution of our choice (C_{12}^F). We found no visible changes in structure when the paper is silanized at 85 °C in 1 min, which is the time required for the silane solution to dry (**Figure 2.1** c–f). Multi-layer texturing of the paper substrate is expected, however, when the reaction is performed at higher temperatures (>95 °C) or for longer times (>30 min), due to the accumulation of small polymeric clusters over the surface of the cellulose fibers [123].

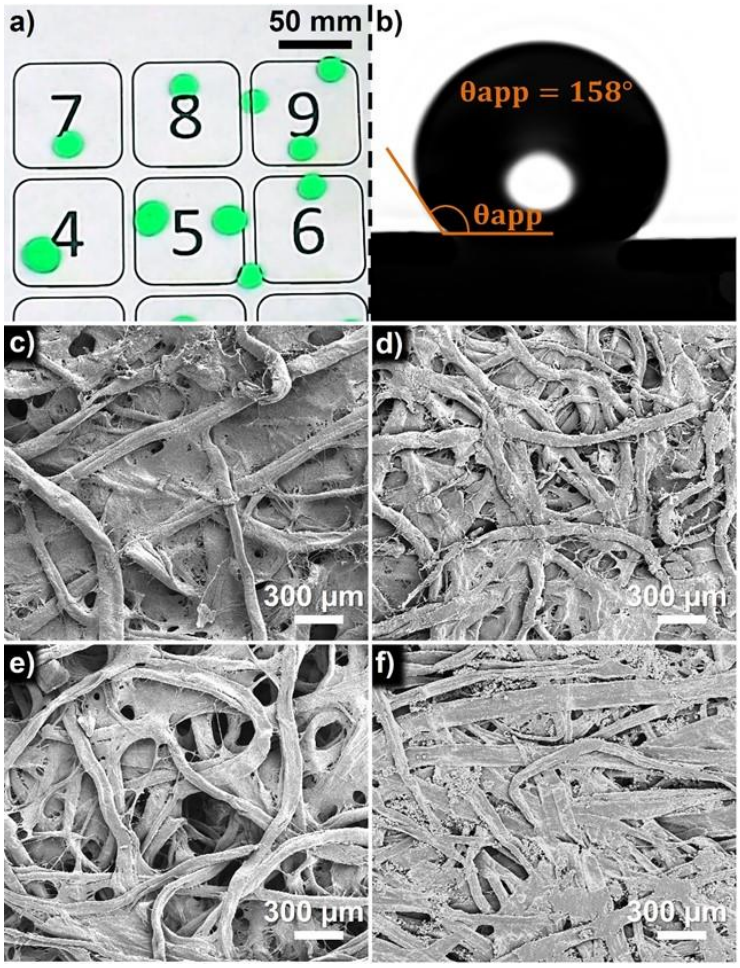

Figure 2.1 Fibrous structure of paper substrates rendered omniphobic by silanization with C_{12}^F. a) Droplets of green-dyed water on top of a flexible RF-SPE keypad rendered omniphobic using the fluoroalkylated silane C12F. b) Apparent static contact angle of a 10µL water droplet on omniphobic Whatman #1 paper. c) High-resolution SEM images of C12F-silanized Whatman #1, Whatman #50 (d), Blot paper (e), and conventional copy paper (f)Charge separation and triboelectric performance of TENGs printed on R^F-SPEs

The tribo-responsive areas in R^F-SPEs owe their self-powered behavior to the paper-mounted triboelectric nanogenerators (TENGs) printed on the back of these devices (**Figure 2.2**). When the user gently compresses, bends, or rubs the surface of these TENGs, the pressure exerted over the silanized cellulose fibers induces their friction and the subsequent generation of negative charges, which are trapped by the PTFE layer [74]. As shown in **Figure 2.13**, both the open-circuit voltages and short-circuit currents generated by R^F-SPEs increase with the length of the fluorosilane used in the functionalization, since the amount of negative charges trapped by the PTFE layer is proportional to the level fluorination of the organosilane. **Figure 2.2**b shows a R^F-SPE displaying "Purdue" through the activation of 48 SMD LEDs when the user taps the surface of its triboelectric area.

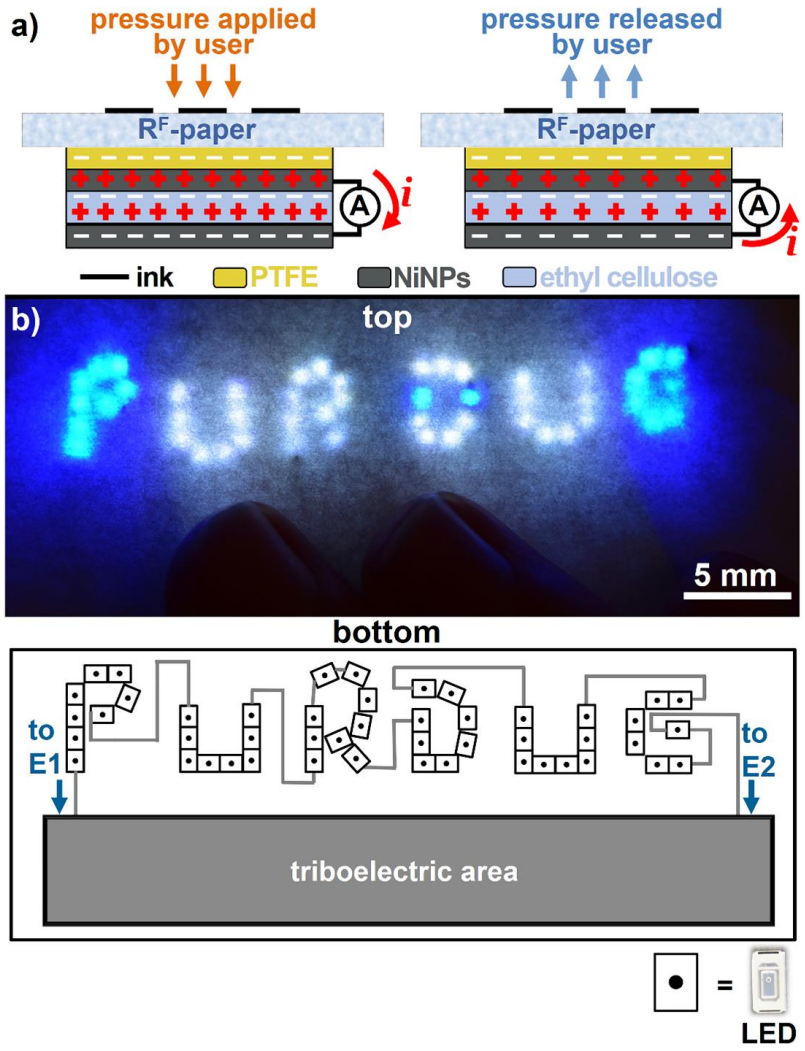

Figure 2.2 R^F-SPE displaying "Purdue" by powering 48 SMD LEDs with the triboelectric energy generated from human-interaction. Note that changes in uniformity of LED intensity is due to the use of LEDs of 2 different colors. a) Schematics of the charge generation process in the TENG printed on the back of a RF-SPE. b) Top: snapshot of the RF-SPE while tapped by the user. Bottom: top-view schematics of the RF-SPE, showing the layout of the paper-mounted LEDs at the bottom of the sheet of paper serving as a substrate for this device. E1 and E2 correspond to the top and bottom electrodes of the triboelectric generator powering this RF-SPE, respectively.

The electrical output characteristics of the triboelectric areas of the R^F-SPEs were collected using a mixed signal Infinii Vision MSO-X-3104T oscilloscope (Keysight Technologies) at a rate of 3×10^5 samples per second. The electrical measurements consisted of open-circuit voltage, short-circuit current, and the output voltage and current across different applied loads (**Figure 2.12**,

Figure 2.13). **Figure 2.3** shows the open-circuit voltage peaks generated by R^F-SPEs treated with fluorinated (C_{12}^F) and non-fluorinated silanes (C_1^H).

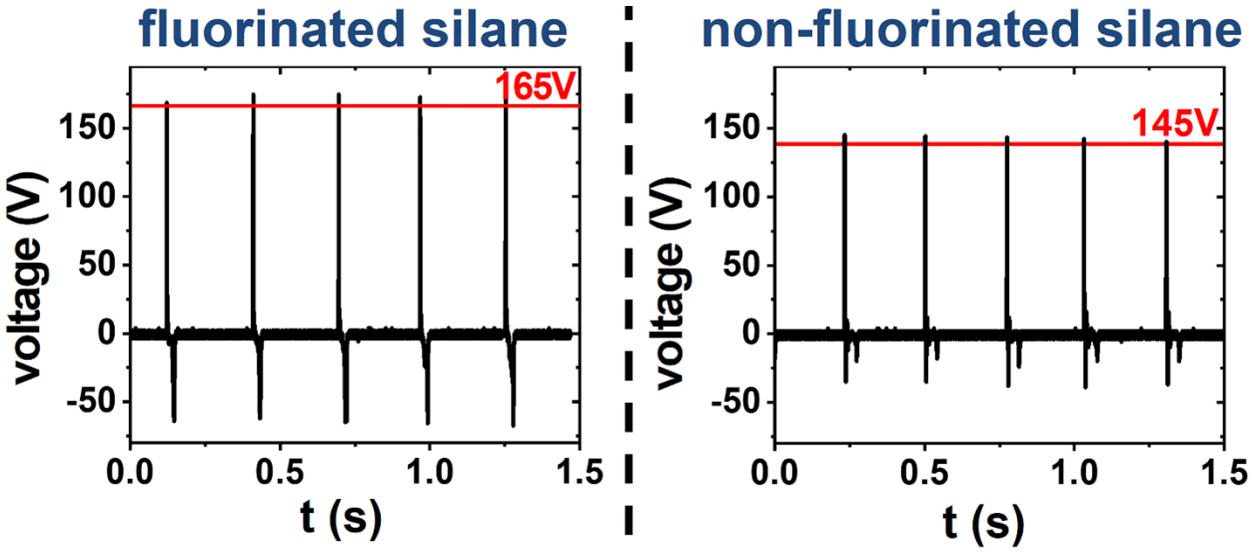

Figure 2.3. Open-circuit voltage peaks generated by gently tapping the TENGs printed over the surface of R^F-SPEs treated with a fluorinated silane (C_{12}^F) and a non-fluorinated silane (C_1^H).

2.2.2 Characterization of wettability of different papers using fluorinated and non-fluorinated silanes

To measure the static contact angle, we used a goniometer system (Krüss Drop Shape Analyzer DSA25) at room temperature (20–25 ℃). The volume of the droplets used in the measurement was ~10 µL to avoid gravity effects. Ten different droplets were used for each measurement, the average of those measurements was reported as the result, and the error bars correspond to the standard deviation of ten samples (**Figure 2.13**b).

The preferred silane to render the R^F-SPEs omniphobic was C_{12}^F as the lateral resolution of printing is directly proportional to the static contact angle of the ink over the surface of the silanized paper [124]. Since C_{12}^F-silanized cellulose paper exhibits high contact angles (> 120°) against liquids with surface tensions greater than 27.05 mN/m, this functionalization prevents the smearing of the conductive NiNPs ink under the stencil mask and its wetting across the cross section of the paper (**Figure 2.4**, **Figure 2.5**).

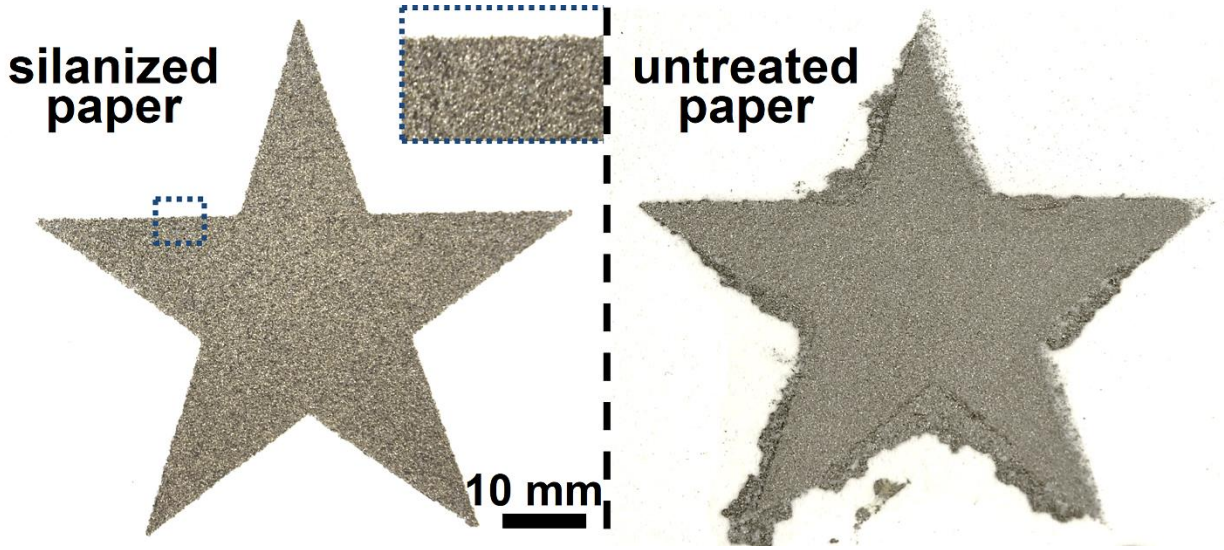

Figure 2.4 S4. Images of NiNPs conductive electrodes spray-deposited through a stencil on C_{12}^F-silanized and unmodified Whatman #1 paper substrate. The inset in the left panel shows the 87µm lateral resolution achieved after spray-coating omniphobic paper with NiNPs/isopropanol cross a flexible stencil mask obtained by laser cutting transparency films.

2.2.3 Rapid printing of flexible R^F-SPE keypads

The wireless flexible keypad reported in this manuscript has an overall area of ~124 cm^2. The stencil mask used for its spray-printing and the dimensions of its electrodes and tribosensitive areas are depicted in **Figure 2.5**b demonstrates the high lateral resolution of the electrodes sprayed through a stencil mask when using C_{12}^F-silanized cellulose paper as a substrate. We incorporated TENGs under each key of the flexible R^F-SPE keypad capable of generating ~5V peaks per keystroke, which was enough to power the wireless module and transmitting the key value to the paired Bluetooth device (**Figure 2.9**).

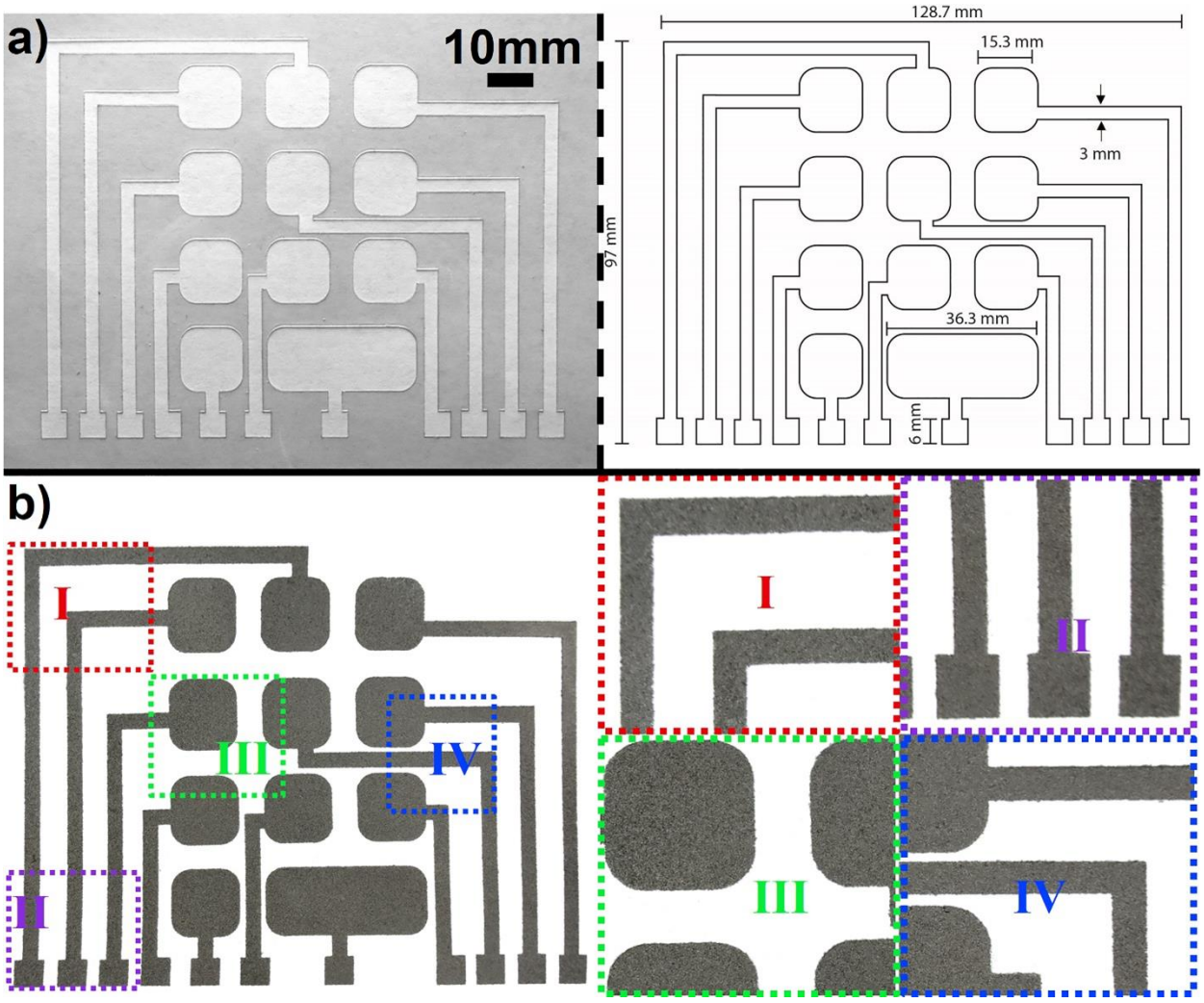

Figure 2.5 Stencil mask and resulting conductive layout of the flexible R^F-SPE keypad. a) Image and dimensions of stencil mask obtained by laser cutting transparency films with a CO_2 laser cutter. b) NiNPs conductive layout of the flexible keypad. The inset shows the high lateral resolution achieved by spray-printing on $C_{12}{}^F$-silanized cellulose paper.

2.2.4 Rectification of the triboelectric voltage and current peaks generated in R^F-SPEs

When the user presses a triboelectric area in the R^F-SPE, the TENG generates a high (positive) voltage peaks (see **Figure 2.6**a). When the user releases the TENG, the system reacts with a change in polarity, which leads to the formation of a second (smaller) peak in the opposite direction. The same occurs during the formation of the current peaks (**Figure 2.7**). By attaching a diode bridge

rectifier to the electrodes of TENG, we are able to harvest these two peaks to power the electronics mounted on the R^F-SPE (see **Figure 2.6**b, **Figure 2.7**b).

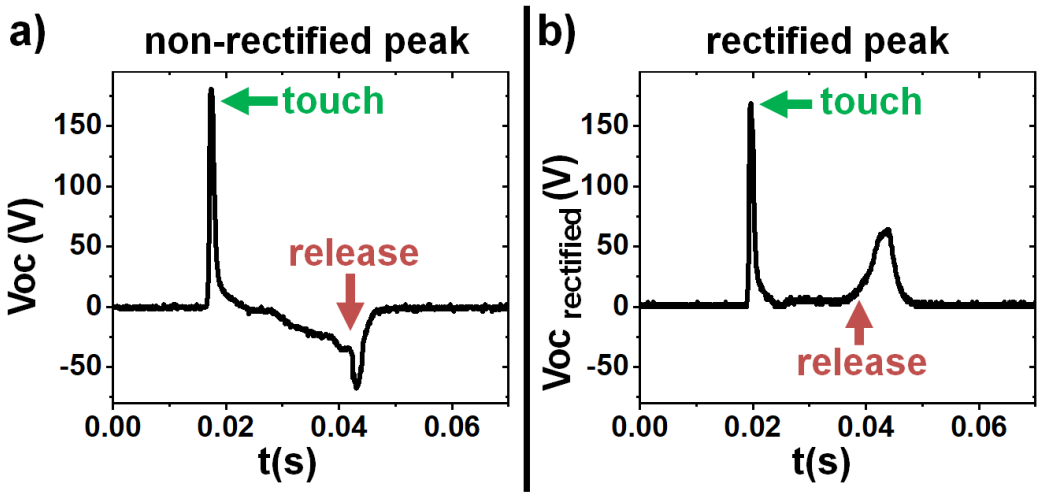

Figure 2.6 Rectification of the open-circuit voltages generated by tapping a 6.25 cm^2 triboelectric area in a $C_{12}F$-treated R^F-SPE. Non-rectified open-circuit voltage peaks generated by pressing and releasing the TENG printed on the R^F-SPE. b) Rectified open-circuit voltage peaks.

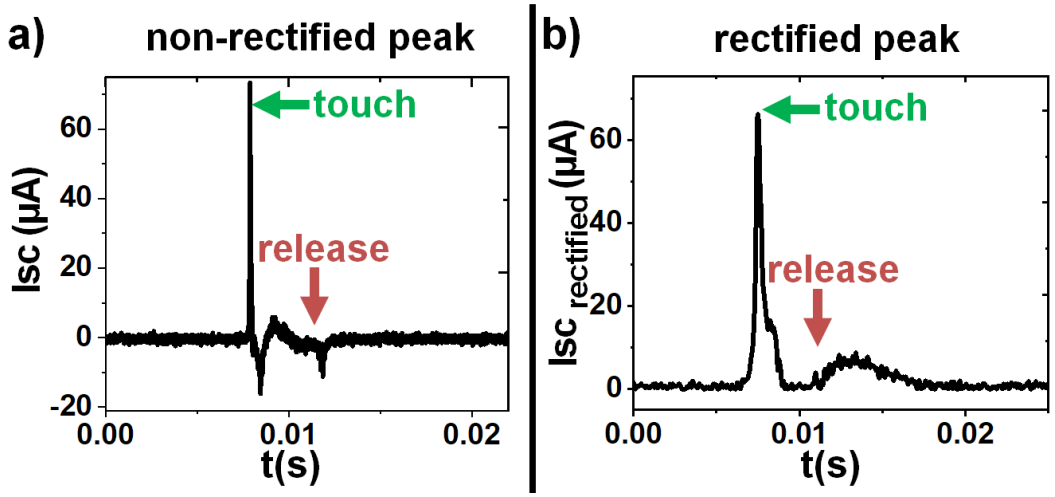

Figure 2.7 Rectification of the short-circuit currents generated by tapping a 6.25 cm^2 triboelectric area in a $C_{12}F$-treated R^F-SPE. a) Non-rectified short-circuit current peaks generated by pressing and releasing the TENG printed on the R^F-SPE. b) Rectified short-circuit current peaks.

2.2.5 Analog signal acquisition and wireless signal processing

We acquired the triboelectric voltage peaks generated during user interaction using a paper-mounted microcontroller (Bluefruit; Adafruit Inc.), which incorporates a rapid capacitive charging module and a low-power analog to digital converter with a quantization capacity of 8 bits. We specified minimum threshold voltages (~4.9V) for each tribosensitive area in R^F-SPE to ensure that the microcontroller would not transmit analog voltages generated by the accidental bending of the device or by rubbing the device against its supporting wood table.

2.2.6 Pressure sensitivity of the R^F-SPE keypad

Most flat-screen capacitive interfaces (cellphones, tablets…) operate upon contact; that is, no external pressure is needed, only physical contact with a material capable to locally discharge the capacitive surface of the interface. The keys of laptop keyboards and keypads, on the other hand, rely on reversibly bucking mechanisms that provide a force threshold that needs to be surpassed in order to register a keystroke. These force thresholds (8 to 13N)[125] are necessary to avoid undesired accidental inputs. Similarly, R^F-SPEs can be subject to accidental readouts due to the voltages generated by the friction the cellulose fibers when the device is bent or slide over a surface. To ensure that those unintended events are not identified as inputs from the user, we introduced a voltage threshold of 5V to the electronics in the R^F-SPE keypad. This voltage threshold is the equivalent of imposing a force threshold of 1.2N. We performed all our experiments on the R^F-SPE keypad were performed applying a compression force of 3N, which is the equivalent of a pressure of 7.83kPa.

We used a force meter to characterize the dependence of the V_{OC} generated by the keys in the R^F-SPE keypad shown in **Figure 2.15** as a function of the applied compression force [126]. **Figure 2.8** shows that the lowest compression force needed to input a keystroke on the R^F-SPE keypad is 1.2 N, which generates a voltage pulse greater than the threshold voltage (V_{OC}=5V) required to transmits the input data to the paired device.

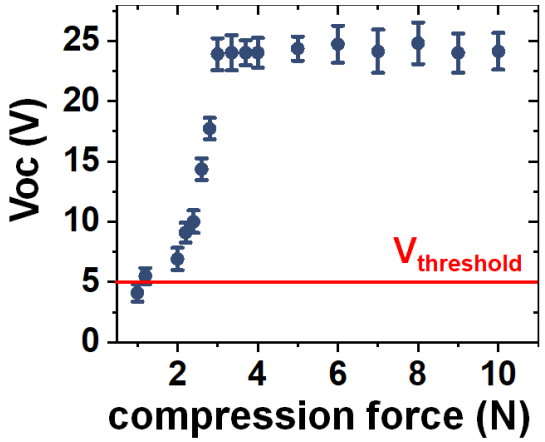

Figure 2.8 Pressure sensitivity of the flexible R^F-SPE keypad shown in Figure 2.15. Open-circuit voltage obtained while typing in the keypad with a compression force varying from 1–10 N.

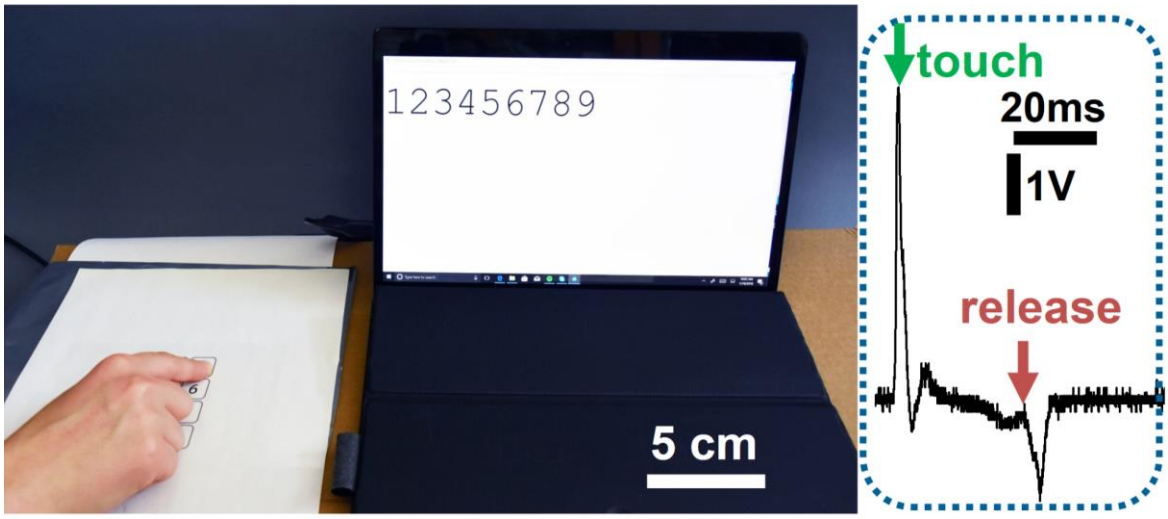

Figure 2.9. Self-powered, paper-based, wireless R^F-SPE keypad. The ~5V peak generated by each keystroke is enough to activate the low-power wireless module and wirelessly transmit the key value to the paired laptop, which keyboard is disabled.

2.2.7 Stability of R^F-SPEs upon washing and drying.

Figure 2.10 shows the stability upon washing and drying of the triboelectric output of the 0-9 keys of the R^F-SPE keypad shown in **Figure 2.15**. Each cleaning cycle consisted on full water immersion for 20s, followed by drying upon contact with absorbent paper.

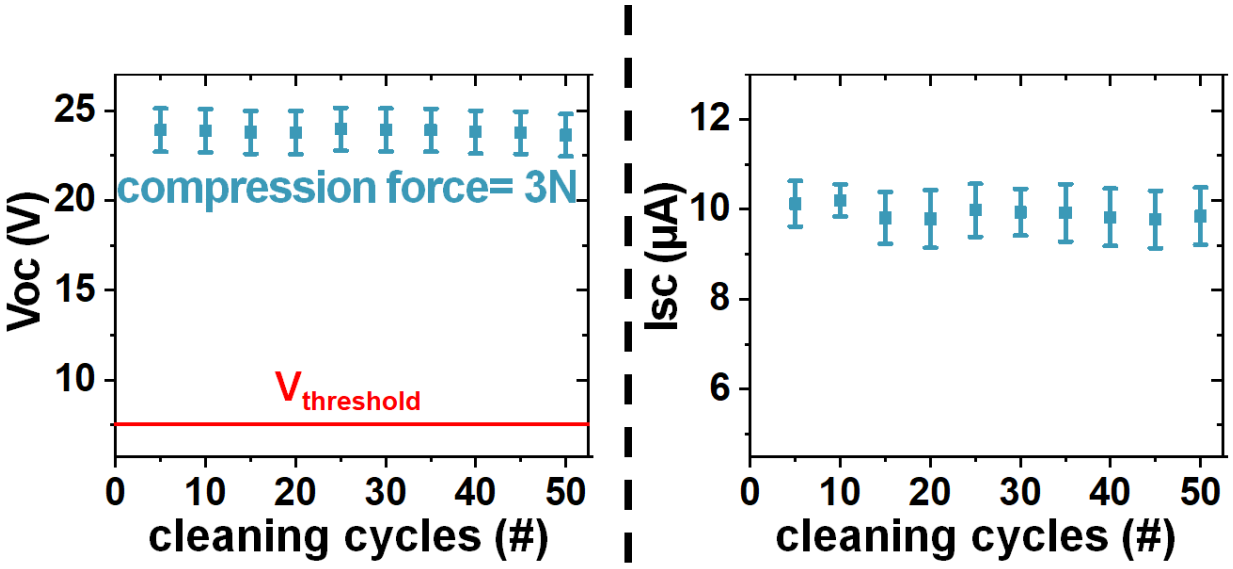

Figure 2.10 Stability of the maximum open-circuit voltage and short-circuit current peaks generated by the 0-9 keys of R^F-SPE keypad shown in Figure 2.15 after 50 cleaning cycles.

2.2.8 Triboelectric areas in the R^F-SPEs wireless music player

Figure 2.11 shows the schematic diagram of the TENGs underneath the functional areas of the R^F-SPE music player interface. The volume slider of this R^F-SPE music player interface can recognize the location and motion of the fingers, distinguishing "*drag to right*" from "*drag to left*" since the area of the TENGs and their corresponding generated triboelectric voltages increase towards the right side of the R^F-SPE.

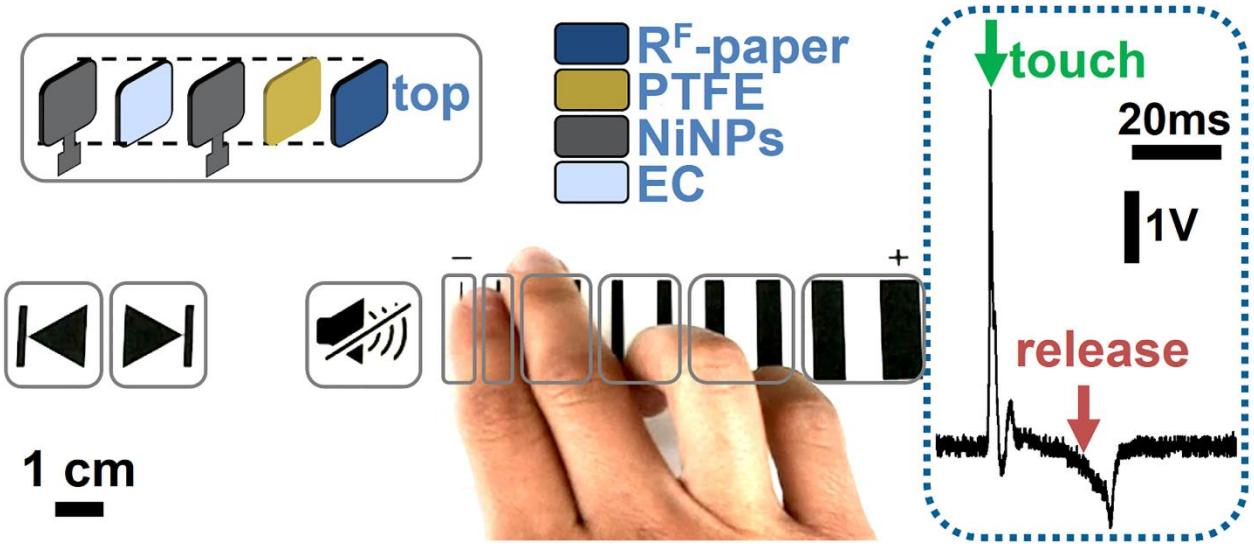

Figure 2.11 Self-powered, paper-based, wireless R^F-SPE music player interface. Schematic diagram of the tribosensitive areas of the wireless R^F-SPE music player interface. The inset shows the voltage peak generated when the user passes his fingers from the TENG in the volume slider with the lowest surface area.

2.2.9 Fabrication costs

We estimate the cost to print R^F-SPE human-machine interfaces, without considering labor or capital expenses, to be less than $ 0.25 for the keypad and less than $ 0.22 for the volume controller. This cost does not include paper-mounted electronics, such as SMD LEDs (~$0.05 per piece), or the reusable microcontroller chip with Bluetooth connectivity (~$4.00). Additionally, the total cost itemized in Table 1 and Table 2, is based on costs of small quantities of material and reagents and could be subject to lower prices based on volume discounts.

Table 1. Itemized cost of the silanization and printing of wireless R^F-SPE keypads.

NiNPs spray coating	$ 0.090
PTFE spray coating	$ 0.055
Omniphobic spray coating	$ 0.042
EC spray	$ 0.049
W#1 Paper	$ 0.004
Total cost	$ 0.24

Table 2. Itemized cost of the silanization and printing of the wireless R^F-SPE music player.

NiNPs spray coating	$ 0.079
PTFE spray coating	$ 0.049
Omniphobic spray coating	$ 0.040
EC spray	$ 0.047
W#1 Paper	$ 0.003
Total cost	$ 0.215

2.3 Results and Discussion

2.3.1 Design and fabrication of R^F-SPEs

Figure 2.12a shows the fabrication process followed to fabricate R^F-SPEs. First, we place a single layer of cellulose paper on a hot plate at 85 °C and rendered it omniphobic by spraying a 5%v/v solution of fluoroalkylated organosilane in isopropanol inside a chemical hood. After the paper is dry (1 min), we pattern triboelectric nanogenerators (TENGs) on the active areas of the device by sequentially spraying through a stencil mask a ~10-µm-thick layer of PTFE, ~10-µm-thick layer of NiNPs, ~10-µm-thick layer of EC, and a second ~10-µm-thick layer of NiNPs waiting for 1 min between each coating to ensure their complete drying. A final coating with the organosilane solution rendered omniphobic the surface of these tribo-responsive areas (**Figure 2.12**a_{vi}). After the stencil mask is removed, a design to facilitate user interaction is printed on the opposite side of the paper using a conventional inkjet printer (**Figure 2.12**b). The paper substrate used to fabricate R^F-SPEs maintains, even after the silanization process, its original fibrous structure **Figure 2.1**) [127,128], gas permeability [14], and mechanical properties [129], exhibiting an apparent contact angle with water of $\theta_{app}^{H_2O} \approx 158°$ (see **Figure 2.12**c, left).

When the user touches any of the TENGs printed on the R^F-SPE, the shear between the omniphobic cellulose fibers and their PTFE coating across the thickness of the paper leads to the generation of triboelectric voltage peaks with a magnitude proportional to the difference between the work functions of EC and the silane/PTFE layers (**Figure 2.2**) and the thickness of the paper (**Figure 2.13**c) [130]. The top and bottom NiNP-electrodes of the TENGs transfer these voltage peaks to the electronics mounted on the R^F-SPE. The charge generated by each keystroke is enough to power the LED mounted on the back of each key (**Figure 2.12**c).

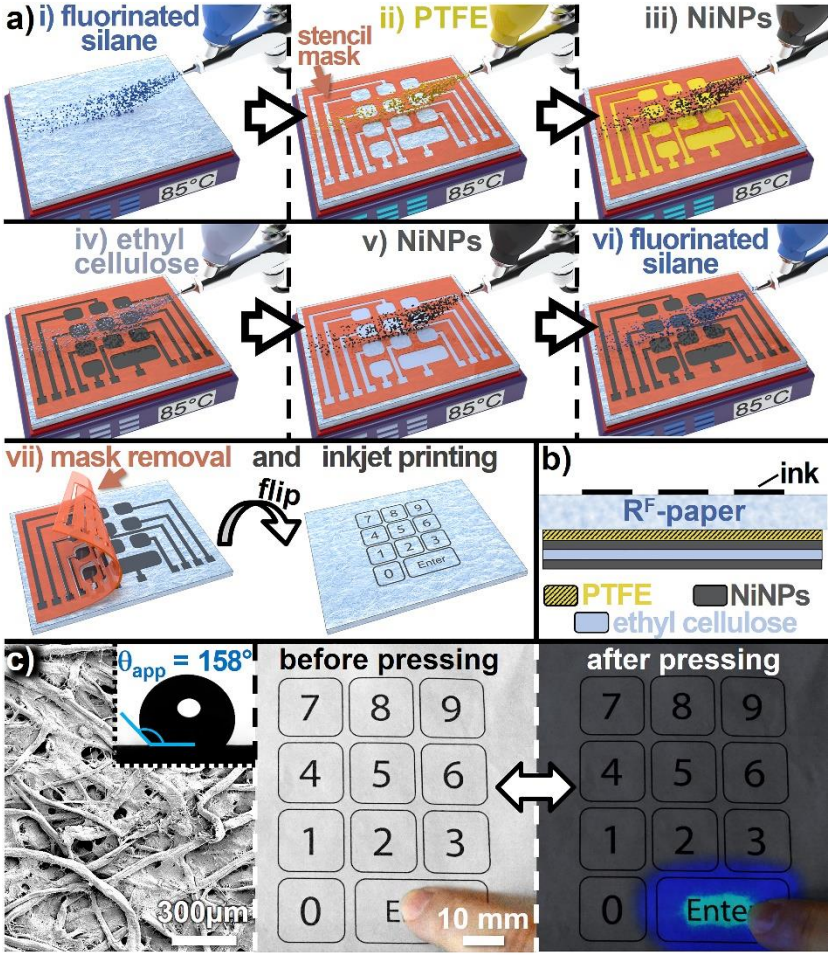

Figure 2.12 Process to fabricate R^F-SPEs on a single sheet of paper. Schematics of the fabrication process used to transform regular cellulose paper into an R^F-SPE keypad: i) the sheet of paper is rendered omniphobic by spraying a fluoroalkylated solution over its surface. After 1 min at 85ºC, the paper is dry and omniphobic, which facilitates the patterning of a TENG by sequentially spraying layers of PTFE (ii), NiNPs (iii), EC (iv), NiNPs (v), and $C_{12}F$ (vi) through a stencil mask, waiting 1 min between coatings to ensure their complete drying; vii) after the stencil mask is removed, visual cues are printed on the opposite side of the paper with a conventional inkjet printer. b) Schematics of the cross section of the ~1 cm^2 paper-based TENG under each of the keys of the R^F-SPE keypad. c) SEM images of the silanized cellulose fibers of this RF-SPE keypad, which remains permeable to gases and exhibits a contact angle with water of $\theta_{app}^{H_2O} \approx 158°$. The SMD LEDs attached under each key of the RF-SPE keypad illuminate with the charge generated by each keystroke."

2.3.2 Resistance to Fold Damage

The NiNP ink used to print the conductive electrodes of R^F-SPEs (**Figure 2.12**a_{iii}) exhibits a strong adhesion to the silanized cellulose fibers of the paper substrate, allowing R^F-SPEs to be repeatedly folded without significantly degrading the electrical performance of the printed electrodes (**Figure 2.13**a). We analyzed the electrical performance of a 10-cm-long, 500-μm-thick, printed NiNP interconnect after 500 folding cycles, each cycle consisting of two perpendicular folds, and obtained relative changes in resistance ($\Delta R/R_0$) below 2%. We attribute the resilience of R^F-SPEs to fold damage be due to both the great conformability of NiNPs inks[18] and the choice of the solvent used to facilitate the spray-based deposition of this ink: isopropanol, which exhibits a surface tension of only 21.7 mN/m and readily spreads over the surface of silanized paper. The principles of origami can therefore be applied to R^F-SPEs in order to augment the functionality and usability of these paper-based devices (see floating origami boat in **Figure 2.13**a).

2.3.3 Dependence of the triboelectric performance on the type of paper and silane used to fabricate the R^F-SPEs

Figure 2.13b, c describe the dependence of the wetting and triboelectric performance of R^F-SPEs on the type of silane used during their fabrication. We chose two non-fluorinated ("C_1^H", "C_{10}^H") and three fluorinated ("C_8^F", "C_{10}^F", "C_{12}^F") organosilanes with different chain-lengths for this study, all commercially available. We used four types of paper with different profile root mean square (RMS) roughness values (copy paper ($2.0 \pm 0.5\mu m$), Whatman #50 ($3.3 \pm 0.8\mu m$), Whatman #1 ($6.4 \pm 1.2\mu m$), and Blot ($9.6 \pm 1.6\mu m$) as substrates for the fabrication of R^F-SPEs. **Figure 2.13**b shows that non-fluorinated silanes generate R^F-SPEs capable to repel fluids with surface tensions greater than 54 mN/m, such as water. These hydrophobic R^F-SPEs, however, cannot repel most oils (surface tension <35 mN/m), which readily wick through their surface [129]. On the other hand, R^F-SPEs silanized with fluorinated silanes are omniphobic: repellent to aqueous, organic, and inorganic solutions with surface tensions as low as 27.05 mN/m [131]. The apparent static contact angle of water ($\theta_{app}^{H_2O}$) on the surface of silanized R^F-SPEs ranges from 130°–165°, increasing with the roughness of the paper (**Figure 2.13**b). The experimental variability induced by the fibrous structure of the paper, however, impedes the clear observation of a monotonic increase of the apparent static contact angle of water with the length of the silane [129]. **Figure 2.13**c

shows how the open-circuit voltages and short-circuit currents generated by R^F-SPEs increase proportionally with the length of the fluorosilane due to the enhancement of the electron affinity of the negative triboelectric electrodes of the R^F- SPEs (**Figure 2.3**) [132]. Additionally, the power output of R^F-SPEs is proportional to the thickness of the paper, since the shear between the omniphobic cellulose fibers and their PTFE coating across the thickness of the paper is responsible for the generation of triboelectric charges. These R^F-SPEs exhibit power densities over 250 $\mu W/cm^2$ when an impedance matching load of 1.5MΩ is applied to the ends of their tribo-responsive areas. C_{12}^F, the fluorinated silane with the longest chain we could find commercially available, maximizes both the power density and the omniphobic behavior of the R^F-SPEs. Additionally, C_{12}^F prevents the smear of the sprayed conductive ink under the stencil mask, enabling the printing of conductive electrodes on the R^F-SPEs with a lateral resolution of ~87µm (**Figure 2.4**, **Figure 2.5**) [124].

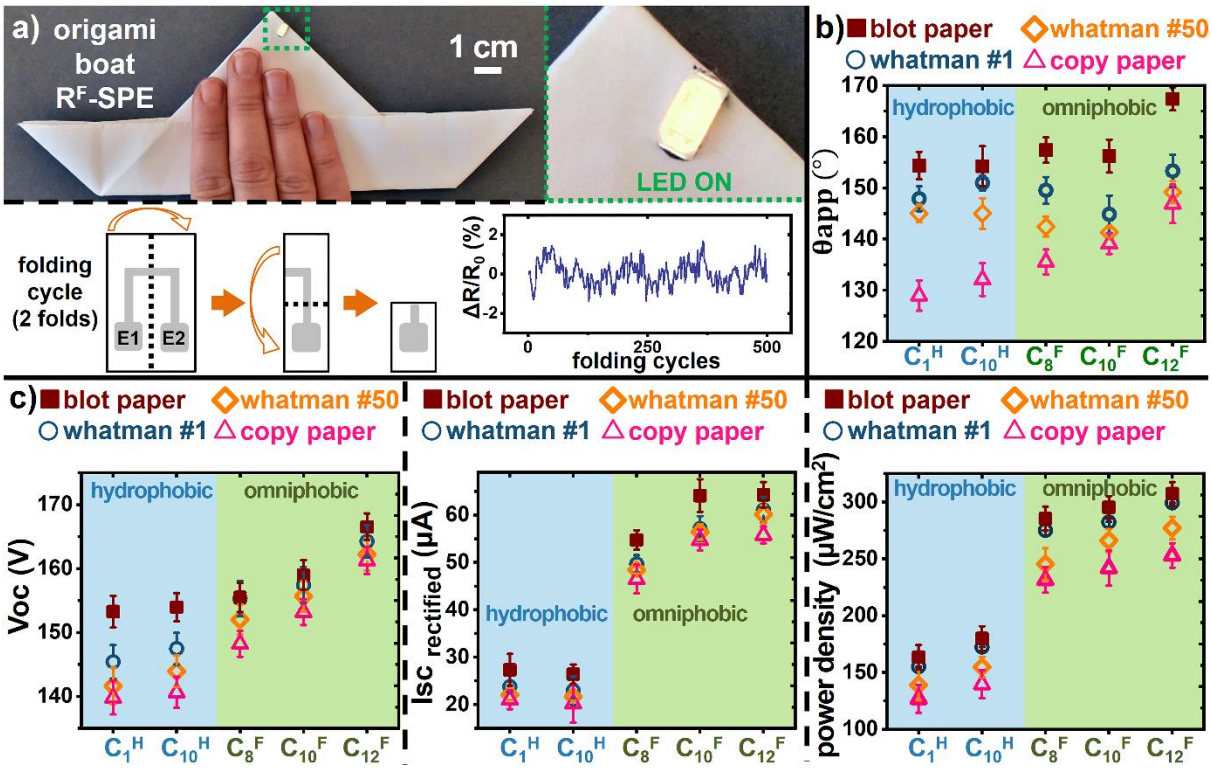

Figure 2.13 Foldability and silane dependence of the triboelectric performance of R^F-SPEs. a) Top: R^F-SPE origami boat using contact with the user to illuminate a paper-mounted LED. The printed circuit of this R^F-SPE is folded 10 times (radius of curvature ~0.3 mm). Bottom: Relative change in resistance experienced by a printed 10-cm-long 500-µm-thick electrical contact joining two electrodes (E1 and E2) after 500 folding cycles, each cycle consisting of two perpendicular folds. b) Apparent static contact angle of water (10µL drops) on the surface of the R^F-SPE. The error bars correspond to the standard deviation of 10 samples. c) Dependence of the open-circuit voltage, rectified short-circuit current, and output power density on the type of paper and silane used to fabricate R^F-SPEs with a 6.25cm^2 tribo-responsive area.

2.3.4 Conversion of Mechanical Energy into Electric Energy using $C_{12}{}^F$-treated RF-SPEs

Figure 2.14 shows the electrical output characteristics of a R^F-SPE with a triboelectric zone of 6.25 cm^2. This R^F-SPE has been fabricated using $C_{12}{}^F$-treated Whatman #1, the combination of paper and silane that optimizes flexibility and power output (**Figure 2.13**c). When the user gently taps the surface of these paper-based devices an open-circuit voltage of ~165 V is generated (**Figure 2.14**a and **Figure 2.6**). By connecting the electrodes of the triboelectric areas to a diode bridge rectifier, short-circuit current peaks of ~60 µA were produced and easily stored in a 2 mF capacitor (**Figure 2.14**b and **Figure 2.7**). We characterized the electrical output performance of the triboelectric areas of the R^F-SPEs by connecting different loads to the diode bridge rectified

attached to the electrode of the paper-based triboelectric generators (**Figure 2.14**c). $C_{12}{}^{F}$-treated R^{F}-SPEs fabricated with Whatman #1 paper can produce current densities up to ~10 μA/cm^2, when paired with small loads, and output power densities up to 300 μW/cm^2 (**Figure 2.14**d, e). The output power and current densities of these R^{F}-SPEs are comparable to those of previously reported TENGs relying on multiple nanotexturized electrodes complex and costly to manufacture [130,133].

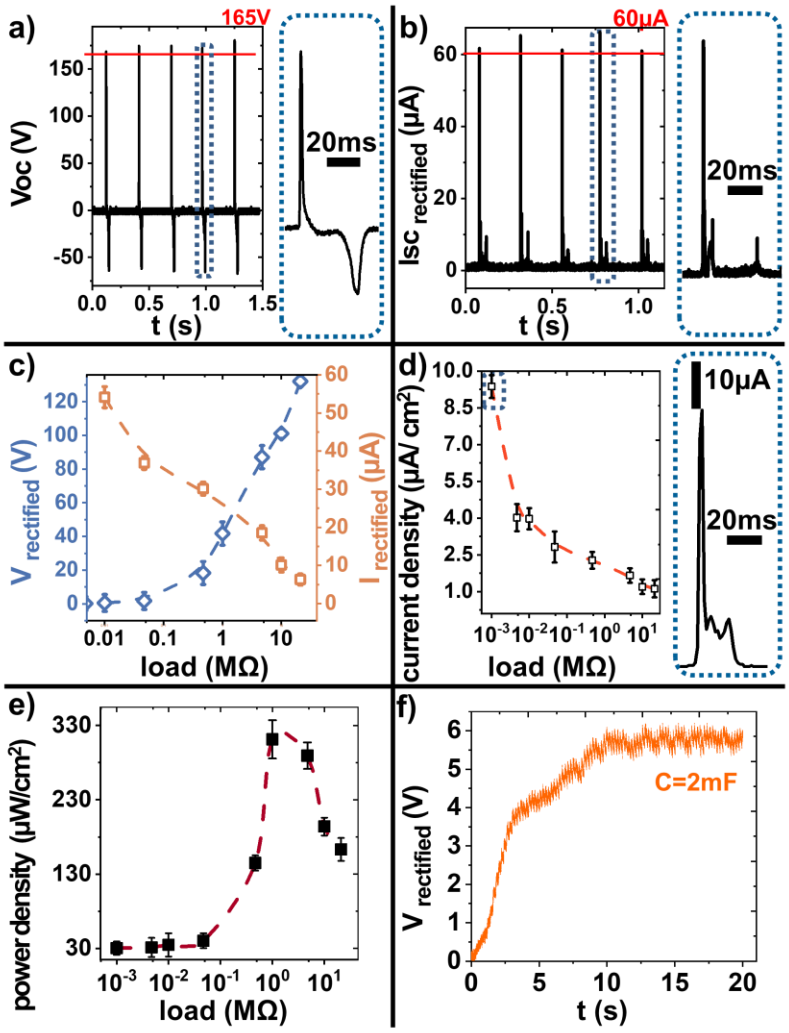

Figure 2.14 Production and storage of electric energy in C_{12}^F-treated R^F-SPEs.
a) Open-circuit voltage peaks generated by gently tapping with two fingers a 6.25 cm^2 paper-based TENG printed on the R^F-SPE. b) Rectified short-circuit current peaks generated by tapping the paper-based TENG. c) Dependence of the rectified open-circuit voltage and the short-circuit current outputs on the coupling load applied to the R^F-SPE. d) Dependence of the current density on the load applied to the R^F-SPE. e) Output power density as a function of the load connected to the R^F-SPE. f) Rectified voltage output stored in a 2 mF capacitor when tapping/typing on a 1 cm^2 TENG.

2.3.5 R^F-SPEs as human-machine interfaces—flexible keypad

Figure 2.15a shows a flexible R^F-SPE keypad that can be wirelessly paired with laptops, tablets, or desktop computers via Bluetooth. Users can type with this R^F-SPE keypad by gently pressing any of the keys (pressure sensitivity < 8 kPa/key, **Figure 2.8**) [126]. The TENGs under each key of the keypad generate a voltage peak (~5 V; **Figure 2.9**) after each keystroke capable of transmitting the key value to the paired device (**Figure 2.15**b)

The omniphobic surface of R^F-SPE devices renders them insensitive to accidental liquid spills with surface tensions as low as 27.05 mN/m (hexadecane) or the accumulation of dust. Liquid droplets formed over the surface of the R^F-SPE can be easily removed by shaking the device or covering it with a piece of absorbent paper (**Figure 2.15**c, d). Dust and solid residues (particle size > 20μm) accumulated on the surface of R^F-SPE devices can be rapidly removed under a stream of running water (**Figure 2.15**e). After more than 50 cleaning cycles by water immersion for 20s and drying by contact with absorbent paper, the omniphobicity and the self-powered pressure-to-text conversion capabilities of the R^F-SPE keypad in **Figure 2.15** remained unaffected, demonstrating the reliability of these paper-based wireless electronic devices (**Figure 2.10**).

Figure 2.15 Flexible and wireless R^F-SPE keypad. a) Flexible R^F-SPE keypad fabricated on a single sheet of paper and integrating a SSHI and a low-power wireless module. b) Snapshots demonstrating the self-powered wireless communication between the R^F-SPE keypad and a laptop with the keyboard disabled. The omniphobic behavior of R^F-SPEs provides this keypad stain repellency to dyed water (c), hexadecane (d), and dust (e). Stained R^F-SPEs can be easily cleaned by wiping them with a paper towel (for liquid stains) or by placing them under a stream of running water (to remove solid residues).

2.3.6 R^F-SPEs as human-machine interfaces—wireless music player

Figure 2.16 shows a flexible R^F-SPE music player interface that can be wirelessly paired with any Bluetooth compatible music player. This paper-based human-machine interface comprises several touch-responsive areas and a slider capable of recognizing the gestures "*drag to left*" and "*drag to right*". Upon user interaction, the TENGs under the responsive areas of the R^F-SPE music player interface (identified with symbols printed on the paper) generate electric voltage peaks of 5V (**Figure 2.11**). These voltage peaks power the low energy Bluetooth chip integrated on this paper-based device and trigger the wireless transmission of the following signals to the music player: "play song", "move to previous", "next song", "stop song" (when the "move to previous" and "next song" responsive areas are pressed at the same time), and "mute song" (**Figure 2.16**b,c). The gesture recognition on the slider of this R^F-SPE music player interface is capable of recognizing the location and direction of motion of the fingers of the user thanks to the gradient in area of the TENGs printed under its surface. This self-powered, paper-based volume controller exhibits a delay response of ~120ms, which enables the monotonic increase and decrease of the volume of the playing song according to the user preferences (**Figure 2.16**d).

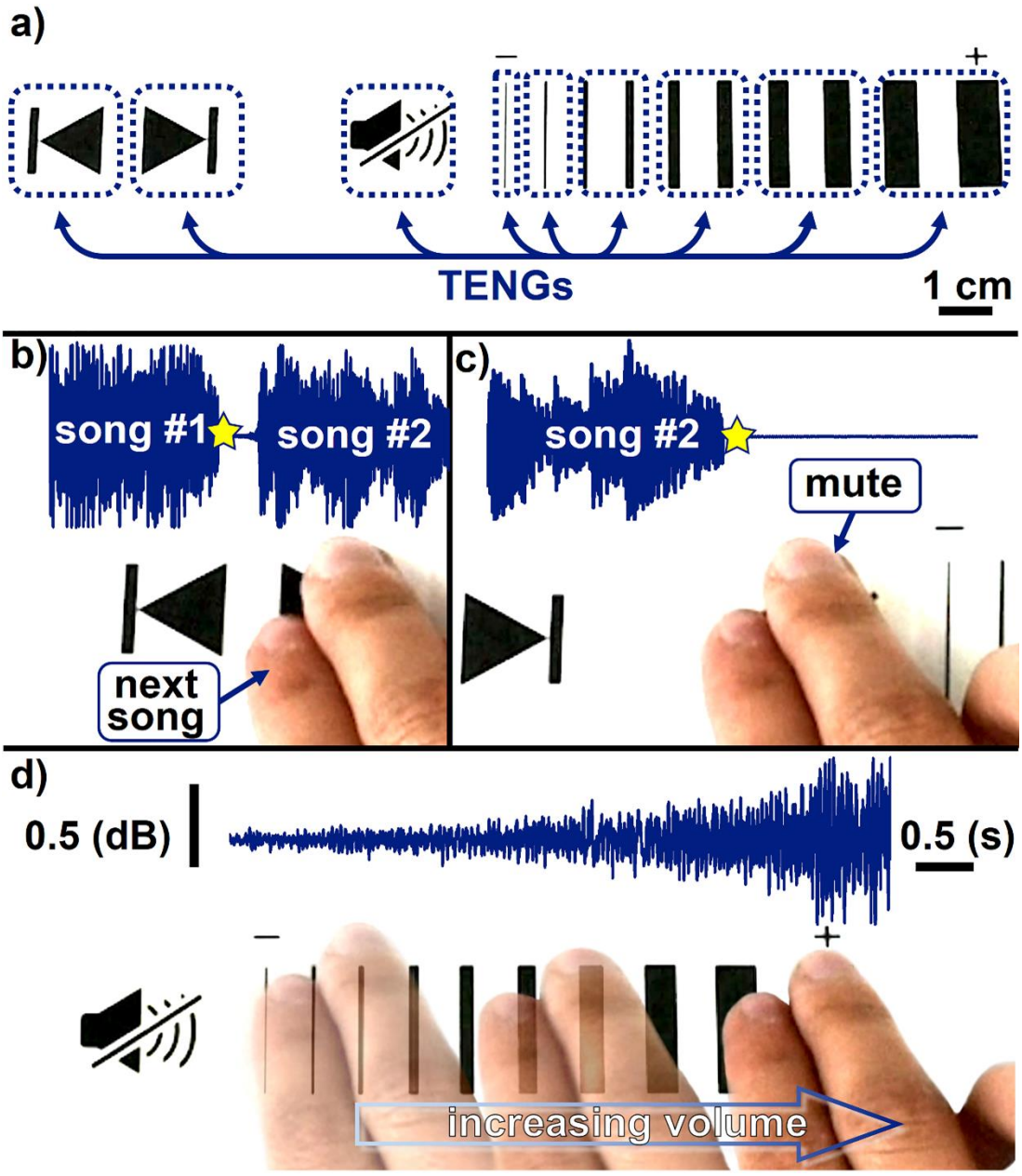

Figure 2.16 Wireless R^F-SPE music player interface. a) Schematic diagram of the triboelectric areas of the wireless R^F-SPE music player interface. b) Gently tapping the "next song" button (event marked with a yellow star) changes the music being played. c) Gently tapping the "mute" button turns the volume to zero. d) Gesture recognition is demonstrated as dragging two fingers from left to right of the volume controller gradually increases the volume of the playing song with a delay response of ~120ms. The sound spectrum illustrates the monotonic volume change. Similarly, moving the fingers from right to left gradually decreases the music volume.

2.4 Conclusions

In summary, this work demonstrates a versatile, cost-effective, and scalable method to fabricate moisture-insensitive and self-powered paper-based electronics devices (R^F-SPEs) that can be used as flexible and wireless human-machine interfaces. R^F-SPEs are simple to design and rapid to print, at a low cost (<$0.25 per device), by simply exposing any cellulose-based paper to the sequential spray-deposition of fluoroalkylated organosilanes, PTFE, EC, and conductive NiNPs. The resulting R^F-SPEs are lightweight, flexible, and even foldable. The omniphobic behavior of R^F-SPEs confers these paper-based electronics with remarkable water, oil, and dust repellency. This omniphobicity preserves the mechanical properties of the cellulose paper substrate upon contact with aqueous solutions and organic liquids with surface tensions as low as 27.05 mN/m and prevents the corrosion of printed electrodes and the electronic components mounted on their surface. R^F-SPEs harvest electrostatic energy from the user during user interaction, generating power densities up to 300 $\mu W/cm^2$, which enables their use as wireless and battery-free human-machine interfaces. The need of a physical separation between neighboring triboelectric areas to prevent current leakage, impedes continuous 2D tactile sensing over a surface with high resolution. However, after simple customization, R^F-SPEs are capable of recreating the key-based and drag-based controllers most commonly found in human machine interfaces. We envision that the simplicity, low material cost, and compatibility with large-scale manufacturing processes of the proposed fabrication method to create R^F-SPEs will pave the way towards the cost-effective fabrication of self-powered paper-based electronics and the ubiquitous integration of human-machine interfaces.

3. WATERPROOF, BREATHABLE, AND ANTIBACTERIAL SELF-POWERED E-TEXTILES BASED ON OMNIPHOBIC TRIBOELECTRIC NANOGENERATORS

Motivation and rationale: Multifunctional electronic textiles (e-textiles) incorporating miniaturized electronic devices will pave the way toward a new generation of wearable devices and human-machine interfaces. Unfortunately, the development of e-textiles is subject to critical challenges, such as battery dependence, breathability, satisfactory washability, and compatibility with mass production techniques. This work describes a simple and cost-effective method to transform conventional garments and textiles into waterproof, breathable, and antibacterial e-textiles for self-powered human-machine interfacing. Combining embroidery with the spray-based deposition of fluoroalkylated organosilanes and highly networked nanoflakes, omniphobic triboelectric nanogenerators (R^F-TENGs) can be incorporated into any fiber-based textile to power wearable devices using energy harvested from human motion. R^F-TENGs are thin, flexible, breathable (air permeability 90.5 mm/s), inexpensive to fabricate (<0.04$/cm^2), and capable of producing a high power density (600 μW/cm^2). E-textiles based on R^F-TENGs repel water, stains, and bacterial growth, and show excellent stability under mechanical deformations and remarkable washing durability under standard machine-washing tests. Moreover, e-textiles based on R^F-TENGs are compatible with large-scale production processes and exhibit high sensitivity to touch, enabling the cost-effective manufacturing of wearable human-machine interfaces.

3.1 Introduction

Here we present a scalable method to transform any conventional garment or textile into a self-powered e-textile capable of harvesting electrostatic energy from a variety of human body motions to power wearable electronic devices. We created omniphobic (both hydrophobic and oleophobic) triboelectric nanogenerators (R^F-TENGs) over the surface of a variety of textiles and garments by combining embroidery with the spray-deposition of conductive nanoflakes, polytetrafluoroethylene (PTFE), and fluoroalkylated organosilanes. We demonstrate that self-powered e-textiles based on R^F-TENGs are flexible, stretchable, breathable, and effectively

repel water, stains, and bacterial proliferation. We also demonstrate that the power output of these e-textiles remains stable after repeated mechanical deformations and standard machine-washing tests. Furthermore, we expect the high touch sensitivity of R^F-TENGs and their compatibility with large-scale production processes to enable the cost-effective fabrication of robust e-textiles for emerging human-machine interface applications.

3.2 Materials and Methods

3.2.1 Fabrication of the R^F-TENGs

The triboelectric nanogenerator is a wearable two-part structure (bottom and top electrodes) made of R^F-fabric, PTFE, and AgNFs. For the top electrode, we rendered the textile omniphobic by spraying a 4.76% v/v solution of a fluorinated organosilane, trichloro(3,3,4,4,5,5,6,6,7,7,8,8,9,9,10,10,11,11,12,12,12-henicosafluorododecyl)silane ($CF_3(CF_2)_9CH_2$-CH_2SiCl_3; "$C_{12}{}^F$") in isopropanol inside a chemical hood. We then sprayed a 5 wt.% suspension of Ag nano-flakes (AgNFs) in toluene over the fabric through a laser cut Teflon stencil mask and let it dry in a desiccator at 36 Torr for 20 min. The omniphobic fabric patterned with the AgNF electrode is then embroidered with an omniphobic shape-matching design (**Figure 3.9**a). This completes the fabrication of the top electrode of the R^F-TENG. We fabricated the bottom electrode of the R^F-TENG by rendering the surface of a stretchable textile (spandex) omniphobic and spraying AgNFs over its silanized fibers. After the suspension of AgNFs dried, we encapsulated the nano-flakes by spraying an ~8μm-thick layer of PTFE (20% v/v solution of PTFE-N UV in N-Ethyl-2-Pyrrolidone, both from Molykote Inc.) and curing it at room temperature for 2 h. The top and bottom electrodes of the R^F-TENG are assembled by sewing them together along the contour of the embroidered design. The surface area of the R^F-TENG used for the measurements shown in **Figure 3.11** of the main manuscript is ~6.25 cm^2.

We used a commercial embroidery machine (EverSewn Hero; EverSewn Inc.) with a USB port to import any customized embroidery design with different sizes up to 110 × 170 mm. The cat design shown in **Figure 3.1** has an area of ~6.25 cm^2 and is the device used to characterize the electrical output of R^F-TENGs (**Figure 3.11**). The embroidery process is automatic: the user only needs to change the color of the thread whenever advised by the machine.

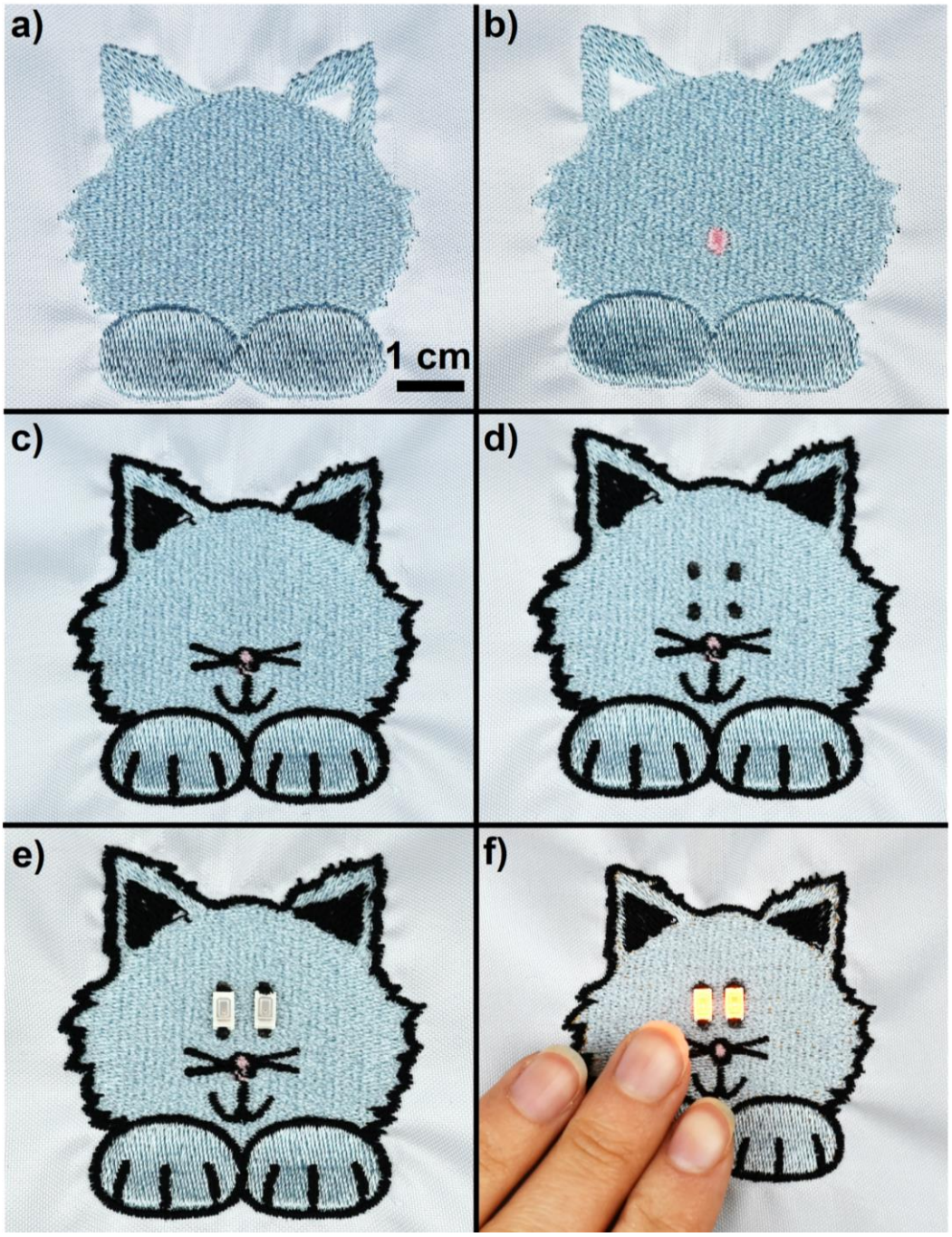

Figure 3.1 Embroidery process steps for the top layer of the R^F-TENG. Droplets of conductive paint are used as a glue to fix the LEDs. LEDs light up on tapping the R^F-TENG fabricated.

3.2.2 Bacterial Quantification Assay

3.2.2.1 Bacterial Incubation

Staphylococcus aureus (*S. aureus*, strain USA300; Sigma Aldrich, VT000326) was cultivated in sterile 50 mL glass tubes containing untreated cotton (control sample) or omniphobic R^F-cotton samples. We grew the *S. aureus* colonies in 10 mL potato dextrose broth (Teknova Inc., Hollister, CA) for 3 h at 37 °C, shaking the colony at 200 rpm. We diluted the *S. aureus* colony 1:100 in fresh potato dextrose broth and used this solution to fill the glass tubes until the samples were fully submerged. After shaking the glass tubes for 3 h at 37 °C, we removed the media by aspiration and added fresh potato dextrose broth. We replaced the media with new fresh potato dextrose broth every 24 h during 7 days.

3.2.2.2 Luminescence Measurements

We followed the protocol provided with the Bactiter-Glo Microbial Cell Viability Assay Kit (Promega Corporation, Madison, WI) to quantify the number of viable *S. aureus* cells on the samples. First, we placed the samples on different well plates and then added Bactiter reagent to each well plate until all the samples were covered. We incubated the samples at room temperature and dark conditions for 5 mins. After the incubation, we transferred 200 µL of the Bactiter reagent covering each sample to an opaque 96-well plate. We measured luminescence using a BioTek Synergy™ 4 Hybrid Microplate Reader (BioTek Instruments, Inc.) and converted the values of luminescence to concentrations using a standard curve of *S. aureus* grown in solution to an optical density (OD) at 600 nm of OD_{600}= 0.8.

3.2.2.3 Quantification of Colony Forming Units

We quantified colony forming units (CFU) of *S. aureus* by spiral plating (Spiral Biotech, Inc.) and used counting grids that relate the colonies on the spiral plate to the volume deposited in the area. *S. aureus* colonies were counted according to the instructions provided by the manufacturer of the Bactiter-Glo Microbial Cell Viability Assay Kit and the guidelines outlined in the *Bacteriological Analytical Manual*.[135]

3.2.2.4 Statistical Analysis

We analyzed the CFU data with the R language for statistical computing (v. 3.5.3), identifying statistically significant differences between the control samples (untreated cotton) and omniphobic cotton using the Non-Parametric Mann-Whitney U test.[136] We considered *p*-values lower than 0.05 as statistically significant. A total of seven sample pairs (control and omniphobic) were used for the graph in **Figure 3.10**b.

3.2.3 Scanning Electron Microscopy

We used a scanning electron microscope (SEM; FEI Nova NanoSEM 200) to characterize the structure of the cotton and spandex substrates and the AgNFs (**Figure 3.9**c) used in the fabrication of the R^F-TENGs. Before imaging of the bare and PTFE-encapsulated fabric substrates, we deposited a ~20 nm layer of platinum using a sputter coater (208HR, Cressington Scientific Instruments, UK) at 40 mA filament current during 60 s. AgNF-coated fabric samples (not yet encapsulated) and individual AgNFs were imaged without any additional conductive coating. We used electron accelerating potentials of 5.0 kV, spot-size of 3, and an Everhart-Thornley detector (ETD) to acquire images of all fabric samples at a working distance of 5–6 mm. High-resolution SEM images of individual AgNFs were obtained using a through-lens detector (TLD) in magnetic immersion mode at a working distance of 3.5 mm.

Control and omniphobic cotton samples cultured with *S. aureus* for 7 days were removed from the cell culture plate and dried under a gentle stream of nitrogen. Note that omniphobic cotton samples remained omniphobic after the 7-day period and were easily dried by tilting them. We used the following protocol to fix the bacteria to the cotton fibers of the samples. First, the samples were immerged for 1 h in a 2.5% glutaraldehyde solution in 0.1 M sodium cacodylate buffer. Second, the samples were gently transferred to a 1% osmium tetroxide solution in 0.1 M sodium cacodylate and maintained immerged for 1 h. Third, we dehydrated the bacteria by exchanging the osmium tetroxide solution for anhydrous ethanol. After the samples were immerged in anhydrous ethanol for 10 min, we dried the samples under a gentle stream of nitrogen, placed them in a desiccator, and coated them with several drops of hexamethyldisilazane, to chemically dry the samples. The samples were kept in the desiccator at 36 Torr overnight. We mounted the samples on SEM specimen stubs (Ted Pella Inc.) using double-sided adhesive carbon tape (Ted Pella Inc.)

and sputter-coated them with a ~50-nm-thick layer of platinum before imaging them at an accelerating voltage of 5 kV.

3.2.4 Characterization of Wettability of Different Textiles Using Polar and Non-polar Solvents

We characterized $\theta_{app}^{H_2O}$, $\theta_{app}^{C_{16}H_{34}}$, $\left(\theta_a - \theta_r\right)^{H_2O}$, $\left(\theta_a - \theta_r\right)^{C_{16}H_{34}}$ on cotton, spandex and wool samples silanized using the following fluoroalkylated organosilanes:

i) trichloro(3,3,4,4,5,5,6,6,7,7,8,8,8-tridecafluorooctyl)silane ($CF_3(CF_2)_5CH_2$-CH_2SiCl_3; "C_8^F"),

ii) trichloro(3,3,4,4,5,5,6,6,7,7,8,8,9,9,10,10,10-heptadecafluorodecyl)silane ($CF_3(CF_2)_7CH_2$-CH_2SiCl_3; "C_{10}^F"),

iii) trichloro(3,3,4,4,5,5,6,6,7,7,8,8,9,9,10,10,11,11,12,12,12-henicosafluorododecyl)silane ($CF_3(CF_2)_9CH_2$-CH_2SiCl_3; "C_{12}^F")

We obtained these silanes from Gelest Inc (Morrisville, PA) and used them without further purification. To measure the static contact angle and contact angle hysteresis we used a goniometer system (Krüss Drop Shape Analyzer DSA25) at room temperature (20–25 °C). The volume of the droplets used in the measurement was ~10 μL to avoid gravity effects. Five different droplets were used for each measurement and the average of those measurements was reported as the result (**Figure 3.12**a).

To silanize the textiles, we sprayed over their surface a 4.76% v/v solution in isopropanol of one of the fluorinated organosilanes specified above and waited until the isopropanol dried at room temperature (~10 min).

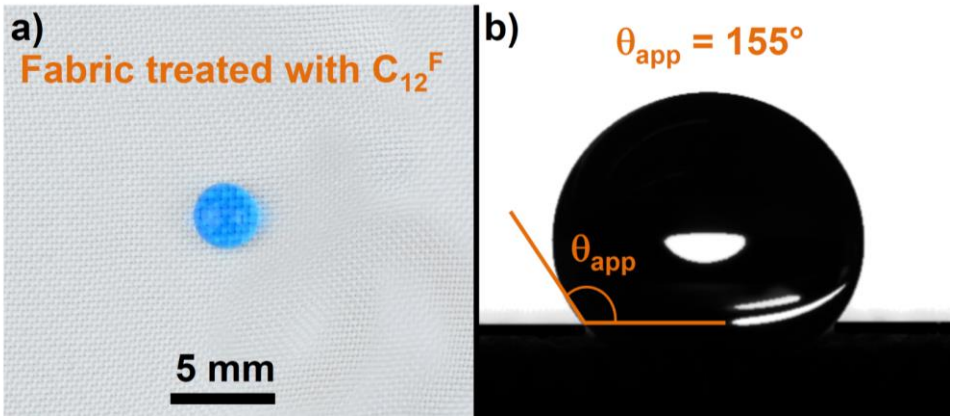

Figure 3.2 Wetting characterization of cotton rendered omniphobic using C_{12}^F organosilane. Droplet of blue-dyed water on top of a piece of cotton fabric rendered omniphobic using C_{12}^F. b) Apparent static contact angle of a 10μL water droplet on the omniphobic cotton.

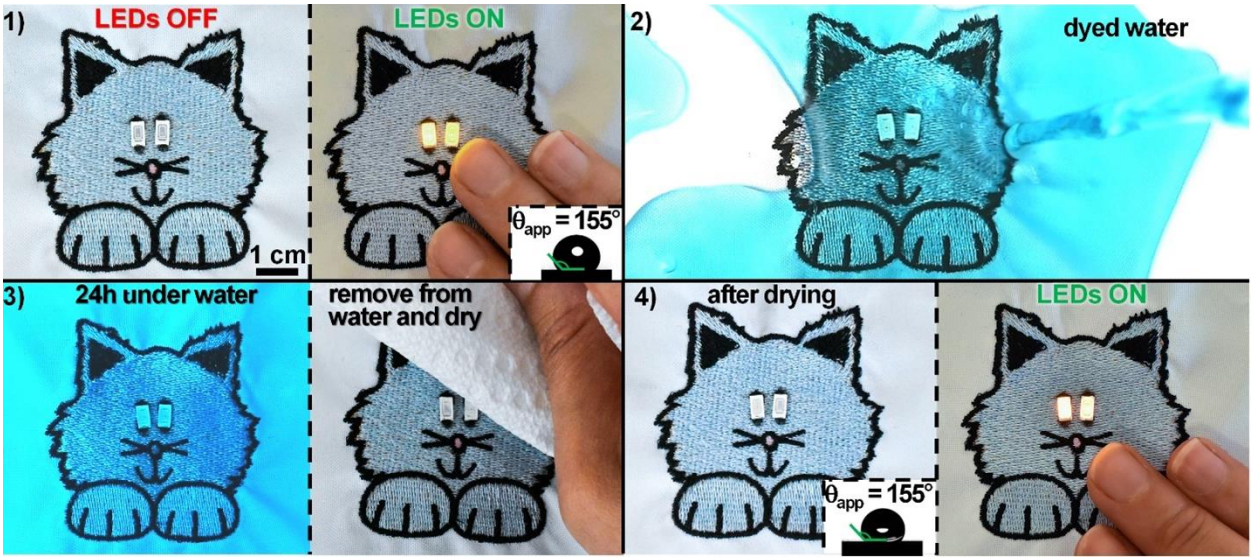

Figure 3.3 Stability of R^F-TENGs to prolonged immersion in water. 1) Energy harvesting by an R^F-TENG before immersion in water. Inset shows an apparent static contact angle $\theta_{app}^{H_2O} \approx 155°$ with water. 2) R^F-TENG being submerged in blue-dyed water. 3) R^F-TENG is kept immersed in water for 24 hours, and then removed from the water and quickly dried with a paper towel. 4) After drying the R^F-TENG, there is no significant change in its $\theta_{app}^{H_2O}$ or its energy-harvesting performance.

3.2.5 Effect of Relative Humidity on the Performance of R^F-TENGs.

Using an experimental setup similar to the one described by Nguyen and Yang,[137] we ramped the relative humidity (RH) from 20% to 80% inside an AtmosBag (Z530204, Sigma Aldrich) at 22 ± 1 ℃ and recorded the open-circuit voltage and short-circuit current characteristics of a 2.25 cm^2 R^F-TENG at RH intervals of 10%. We found no significant changes in the performance of the R^F-TENGs as the relative humidity was gradually ramped up from 20% to 80%, observing variations of the peak voltages and currents oscillating within 10% (**Figure 3.4**).

Previous studies[137,138] reported that TENGs experience up to 20% drop in charge generation when exposed to a relative humidity of 80%; however, due to the omniphobic functionalization in R^F-TENGs, they do not suffer from any significant deterioration in performance even as the humidity increases to 80%.

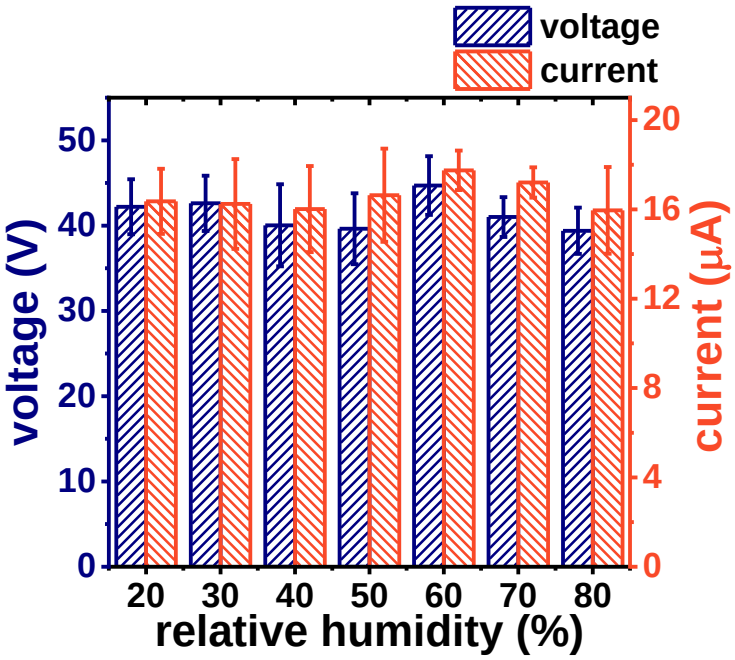

Figure 3.4 Open-circuit voltage and short-circuit current characteristics of 2.25 cm^2 R^F-TENGs at different values of relative humidity and a constant temperature T = 22 ± 1 °C.

3.2.6 Production and Storage of Electric Energy Using R^F-TENGs

The electrical output characteristics of the R^F-TENGs were obtained using an Infinii Vision MSO-X-3104T oscilloscope (Keysight Technologies) at a rate of 3×10^5 samples per second. The electrical measurements consisted of open-circuit voltage, short-circuit current, output current with different loads, output voltage with different loads, and the charging curves of different capacitors over time (**Figure 3.11** and **Figure 3.12**).

Figure 3.5 shows R^F-TENGs used to charge four different capacitors (2 mF, 3 mF, 4 mF, 5 mF) using a universal testing machine (MTS Insight 10; MTS Systems Corp.), with a 1 kN load cell covered with cotton fabric (model 661.18.F01), which tapped the R^F-TENGs at a frequency of 4 Hz and a constant pressure of ~0.47 psi. The cat design has an area of 6.25 cm^2 (**Figure 3.5**e), the fish 4.5 cm^2 (**Figure 3.5**c) and the cherry 2.25 cm^2 (**Figure 3.5**a). The plots in **Figure 3.5**b,d,f verify the trend observed in previous studies:[139] capacitors with smaller values of capacitance are charged and get saturated faster than those with higher values of capacitance.

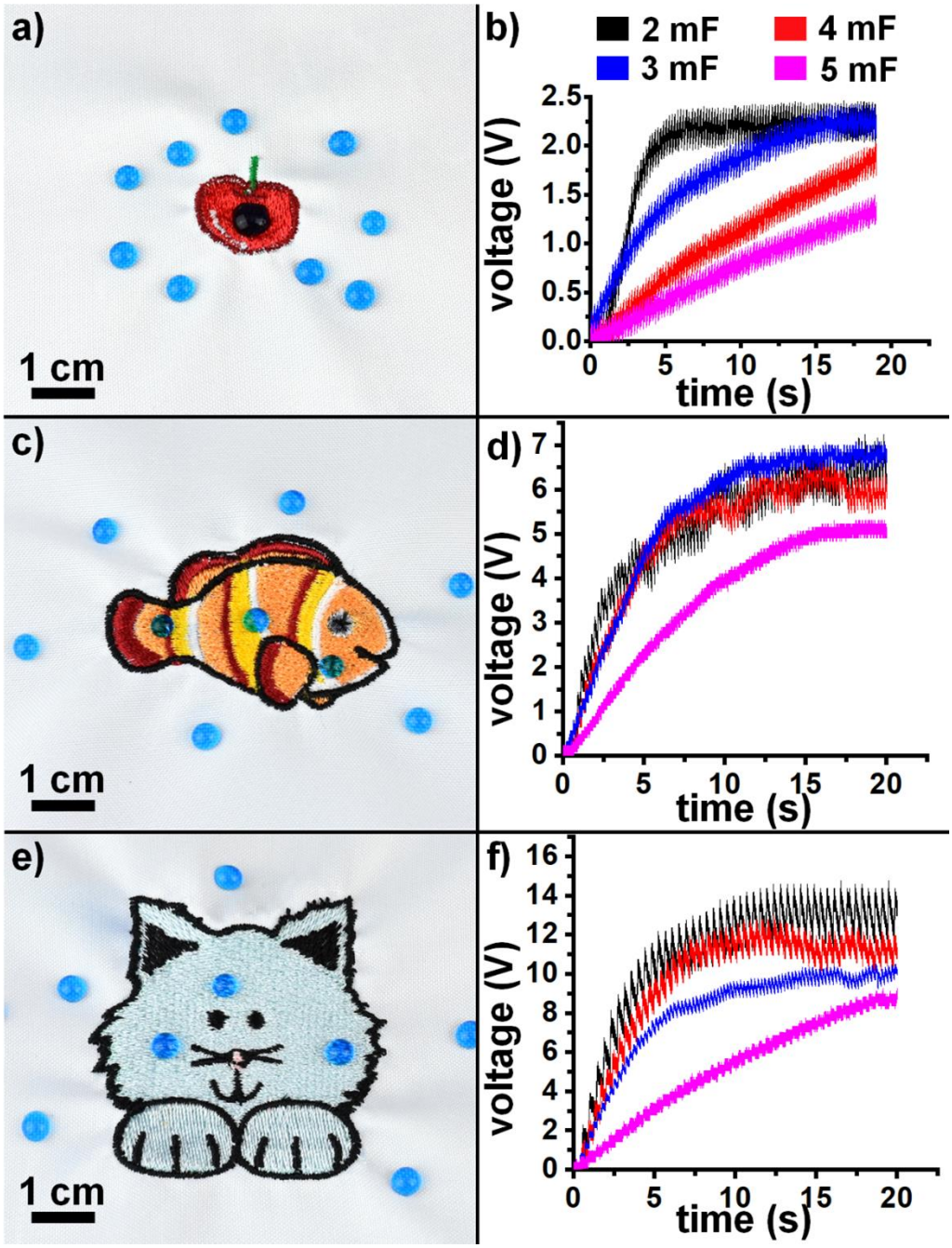

Figure 3.5.Production and storage of electric energy using different R^F-TENG sizes and capacitors with different capacitances. Capacitors of 2 mF, 3 mF, 4 mF, and 5 mF were each charged by the three different sizes of R^F-TENGs. a) R^F-TENG with a cherry design of area 2.25 cm^2. b) Charging curves of different capacitors, produced by tapping the R^F-TENG in (a) at ~4 Hz. c) R^F-TENG with a fish design of area 4.5 cm^2. d) Charging curves of different capacitors, produced by tapping the R^F-TENG in (c) at ~4 Hz. e) R^F-TENG with a cat design of area 6.25 cm^2. f) Charging curves of different capacitors, produced by tapping the R^F-TENG in (e) at ~4 Hz.

Figure 3.6 shows how, after 50 washing cycles, R^F-TENGs can charge a 2 mF capacitor through a diode bridge rectifier (electronic components embedded in the e-textile) without any significant decrease in performance. The maximum voltage transferred to the capacitor is achieved after 18 s of continuous tapping (tapping frequency 4 Hz, pressure ~0.47 psi), and remains proportional to the size of the R^F-TENG even after the vigorous spinning and abrasive action of the ballast during 50 washing cycles. We attribute the stability of the performance of the R^F-TENG to the omniphobic e-textiles aiding the protection of the embedded electronic components from corrosion and the mechanical barrier provided by the embroidered layer on top of the R^F-TENG.

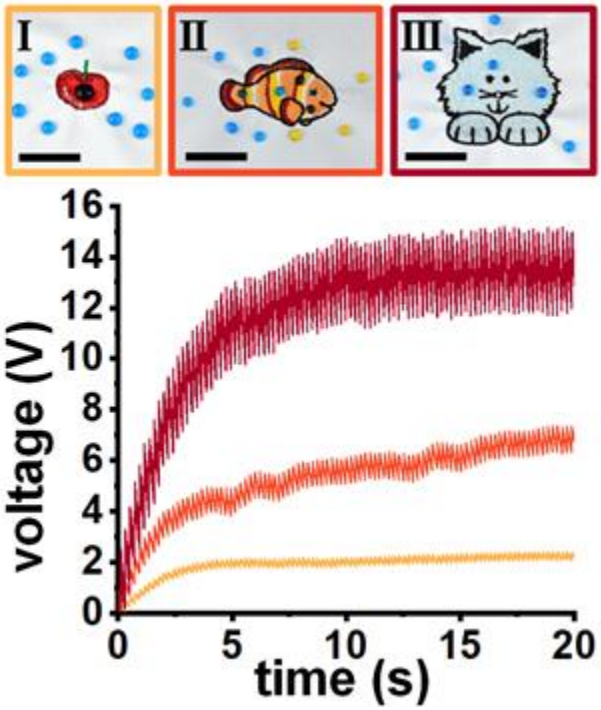

Figure 3.6. Charging curves of a 2 mF capacitor embedded in R^F-TENGs of different sizes (I- cherry design ~2.25 cm^2; II- fish design ~4.5 cm^2; III- cat design ~6.25 cm^2) fabricated in cotton, after 50 cycles of standard machine washing.

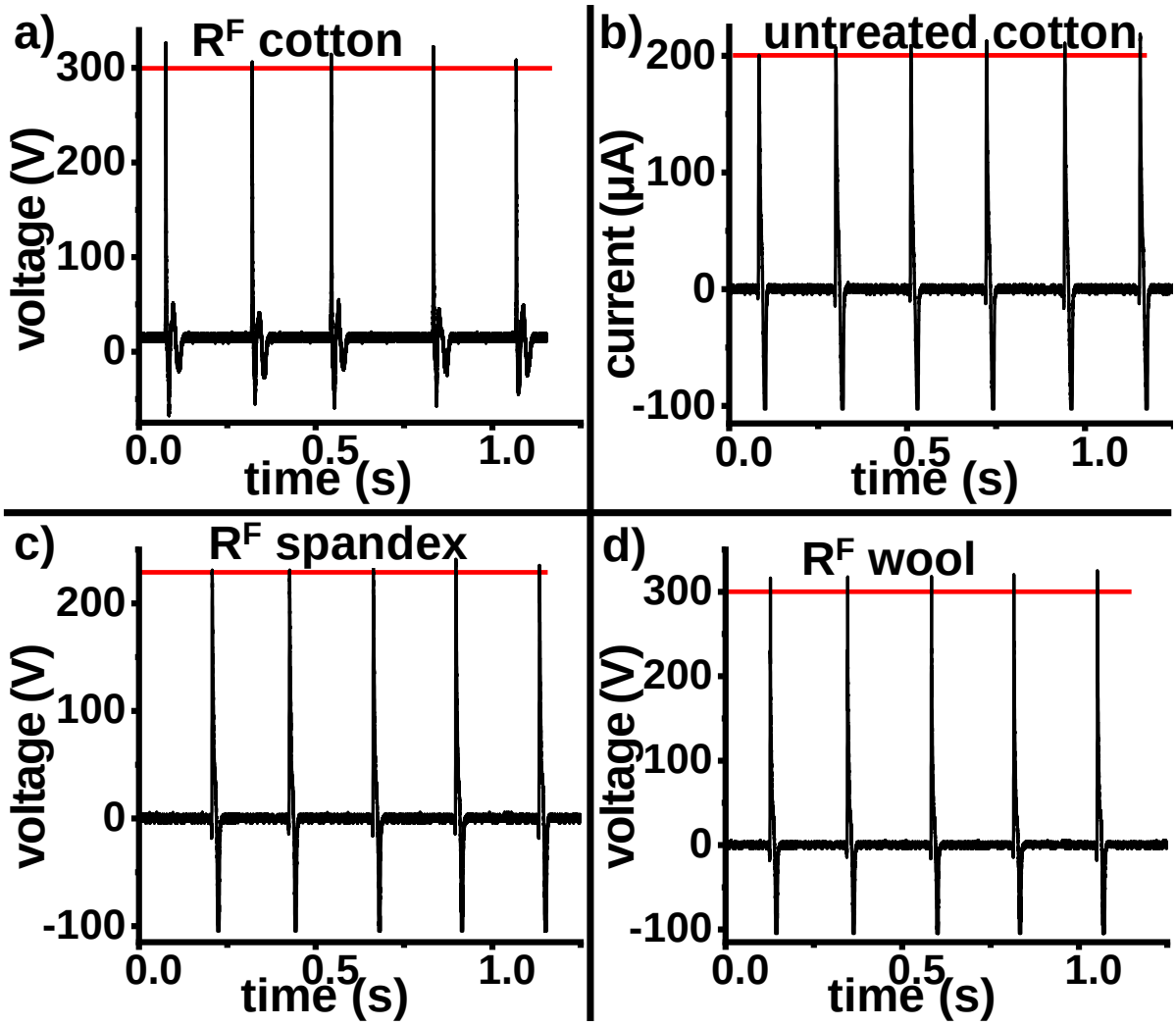

Figure 3.7 Voltage peaks generated by tapping R^F-TENGs (area = 6.25 cm^2) made with different fabrics: silanized cotton; b) untreated cotton; c) silanized spandex; d) silanized wool.

3.2.7 Fabrication of Self-Powered Human-Machine Interfaces based on R^F-TENGs

We incorporated two R^F-TENGs in a polo-shirt to fabricate an audio system controller with a compact fashionable design that fits within the shirt collar. The controls for play/pause are located on the right side of the collar while the control of volume is available on the left side. The different layers of the audio control interface on the collar are detailed in **Figure 3.8**.

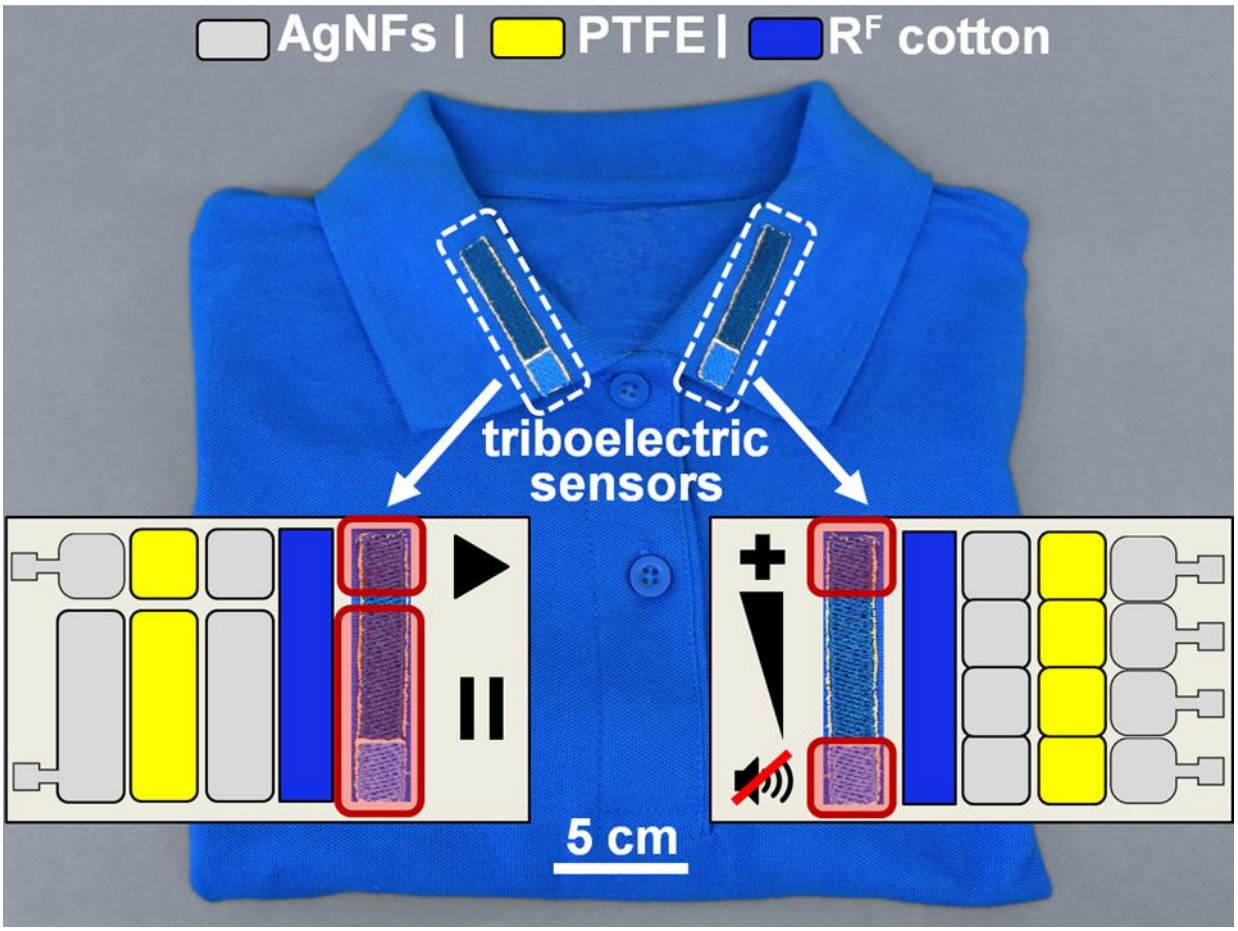

Figure 3.8 Layers of the audio control interface described in Figure 3.14. Right side of the collar: play/pause controls; left side of the collar: volume/mute controls.

3.2.8 Analog Signal Acquisition and Signal Processing

We acquired the voltage peaks generated by each tactile interaction using a multichannel microcontroller (GEMMA V2; Adafruit Inc.), which also served as an analog to digital converter with a quantization capacity of 8 bits. We specified threshold voltages for each tactile zone to ensure that the microcontroller would be able to differentiate touch events from the accidental bending or stretching of the R^F-TENG.

3.2.9 Fabrication Cost

We estimate the cost to make 6.25 cm^2 R^F-TENGs to be less than $ 0.19, without considering labor or capital expenses. The total cost, itemized in **Table 3**, is based on the costs of relatively small quantities of material and reagents (**Table 4**) and could be subject to lower prices based on volume discounts.

Table 3. Bill of materials to fabricate R^F-TENGs

Item	ID	Vendor	Qty.	Cost (US$)
PTFE Spray	MPTFEN300M	Silmid, UK	400 mL	13.65
AgNF	47MR-11F	Inframat Advanced Materials	500 g	694.00
Silane	SIT8174.0	Gelest Inc.	750 g	1665.00
Embroidery Thread	B077Z5VJHN	New Brothread	20000 m	25.99
Cotton Fabric	B00EQJ3C7Y	Fabric Wholesale Direct	14000 cm^2	2.49
Spandex	B01N0ETLLS	Fabric Wholesale Direct	14000 cm^2	4.23
Toluene	600173480656	Dural Company	12 L	89.95
Isopropanol	741296772799	Florida Laboratories	15.14 L	92.70

Table 4. Itemized cost of 6.25 cm^2 R^F-TENGs

AgNF spray coating 30 mg AgNF: $ 0.046 6 mL Toluene: $0.044	**$ 0.090**
PTFE spray coating 1500 μL: $ 0.050	**$ 0.050**
Omniphobic spray coating 30 mg Silane: $ 0.037 500 μL Isopropanol: $0.003	**$ 0.040**
Thread for embroidery 230 cm thread: $ 0.003	**$ 0.003**
Textiles 6.25 cm^2 cotton: $ 0.0011 6.25 cm^2 spandex: $ 0.0018	**$ 0.003**
Total cost	**$ 0.19**

3.3 Results and Discussion

3.3.1 Design and Fabrication of R^F-TENGs

Figure 3.9a shows the fabrication process followed to fabricate the top electrode of the R^F-TENG on any fabric or cloth item. We first rendered the textile omniphobic by spraying a 4.76% v/v solution of a fluoroalkylated organosilane in isopropanol inside a chemical hood. After the isopropanol evaporates, the silanized textile exhibits an apparent static contact angle $\theta_{app}^{H_2O} \approx 155°$ with water (**Figure 3.9**c) and $\theta_{app}^{C_{16}H_{34}} \approx 122°$ with hexadecane. The silanized textile fibers of the R^F-TENGs do not show significant multi-layer texturing artifacts since their silanization was completed in ~10 min, at room temperature. Multi-layer texturing is expected, however, when the reaction is performed at higher temperatures (95 °C) or for longer times (> 30 min), due to the formation of small polymeric particles on the surface of the textile.[128] We then sprayed a 5 wt. %

suspension of Ag nanoflakes (AgNFs) in toluene over the fabric through a laser cut Teflon stencil mask and let it dry in a desiccator at 36 Torr for 20 min. The omniphobic fabric patterned with the AgNFs electrode is then embroidered with a protective shape-matching design, which is also rendered omniphobic using the same spray silanization process. This step completes the fabrication of the top electrode of the fabric-based R^F-TENG. We fabricated the bottom electrode of the R^F-TENG (**Figure 3.9**b) by rendering the surface of a stretchable textile (spandex) omniphobic and spraying AgNFs over its silanized fibers. After the suspension of AgNFs dried, we encapsulated the highly networked nanoflakes by spraying an ~8-µm-thick layer of PTFE and curing it at room temperature for 2 h. The top and bottom electrodes of the R^F-TENG are assembled by sewing them together along the contour of the embroidered design (**Figure 3.9**c, **Figure 3.1**c).

Figure 3.9 Fabric-based R^F-TENG fabrication process.
a) Schematic diagram of the fabrication of the top electrode of the R^F-TENGs: (1) A spray silanization process renders the fabric or cloth omniphobic; (2) The shape of the top electrode is defined by spraying AgNFs over the omniphobic textile through a stencil mask; (3) The AgNFs are protected by embroidering a shape-matching design that is also rendered omniphobic by silanization. b) Schematic diagram of the fabrication of the bottom electrode of the R^F-TENGs: (4) A spray silanization process renders a piece of spandex omniphobic; (5) Spray deposition of AgNFs over the omniphobic spandex; (6) Encapsulation of the AgNFs with PTFE by spray deposition. c) Assembly of the fabric-based R^F-TENG: (7) top and bottom electrodes are assembled by sewing along the contour of the embroidered design. The inset of the top electrode shows a representative SEM image of the conformal AgNF coating of the fibers of the omniphobic fabric. The inset of the waterproof textile shows an SEM image of a silanized cotton fabric, which exhibits $\theta_{app}^{H_2O} \approx 155°$. The inset of the bottom electrode shows an SEM image of the conformal PTFE encapsulation of the AgNFs.The proposed fabrication method to create fabric-based R^F-TENGs is simple, easy to customize, scalable, and compatible with mass-production technologies using a variety of commercially available fibers and textiles. Additionally, the omniphobic character of the R^F-TENGs protects the AgNFs electrodes from moisture, making these fabric-based devices waterproof and facilitating their cleaning. The spray deposition processes used to render the textiles omniphobic and to deposit thin conformal layers of highly networked AgNFs and PTFE preserve the flexibility, natural breathability (air permeability ~90.5 mm/s), and light weight of the used textiles.

Figure 3.9 continued

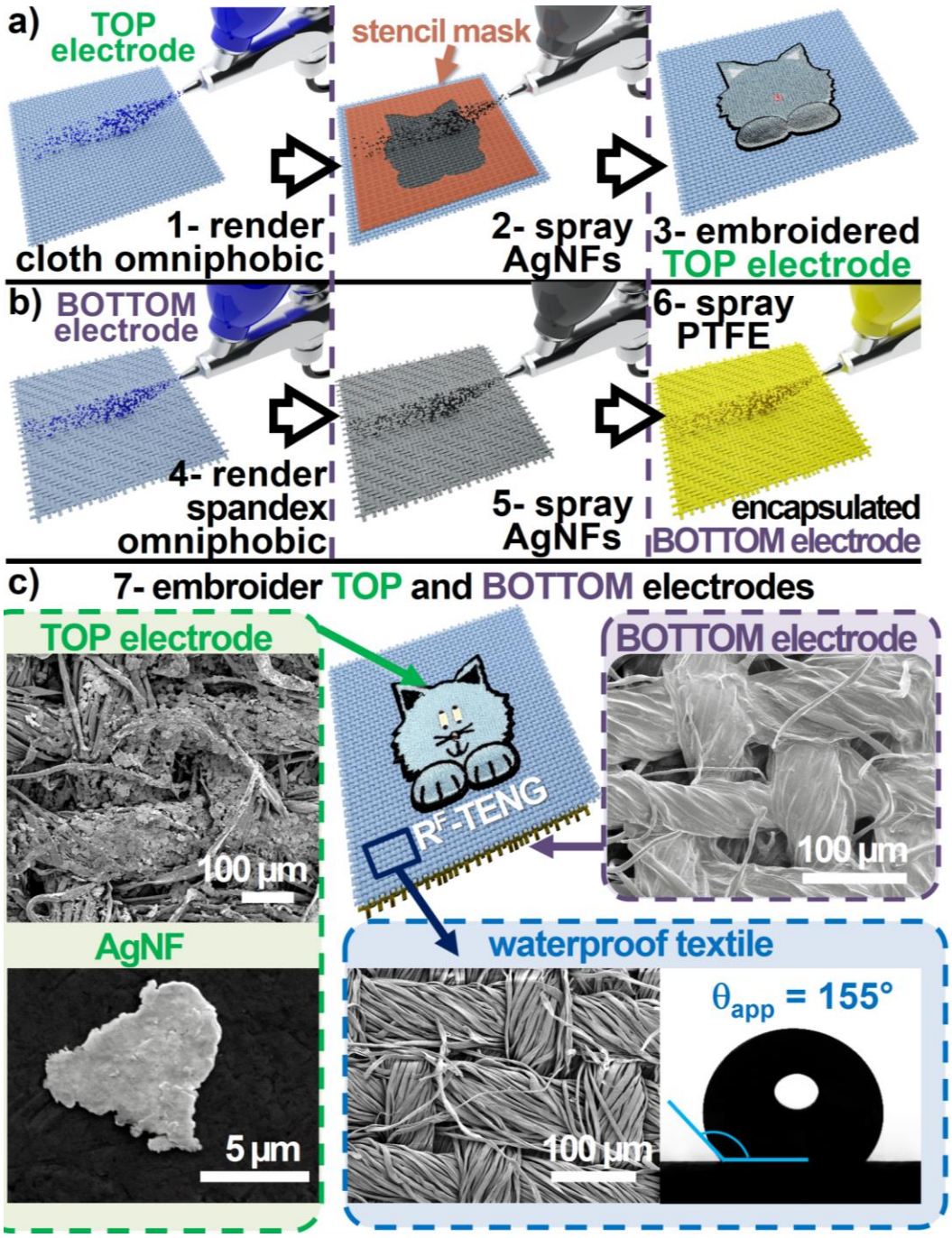

3.3.2 Working Principle of Flexible and Stretchable R^F-TENGs.

Omniphobic textile-based R^F-TENGs operate in vertical contact-separation mode,[140] generating energy when the motion of the wearer induces the compression, bending, or rubbing of the device (**Figure 3.10**a). The repetitive separation and re-contact of the omniphobic textile layer of the top electrode and the PTFE coating of the bottom electrode generates charges on their surfaces due to the triboelectric effect—where two materials with different tendencies to gain or lose electrons become electrically charged after they are separated from each other.[141] The polarity and magnitude of the resulting triboelectric charges on each material is governed by their relative positions in the triboelectric series. In the case of the R^F-TENGs, the R^F-textile becomes positively charged while the PTFE layer becomes negatively charged, since PTFE is lower in the triboelectric series than most textiles.[74] Note that triboelectric materials may be either conductors or insulators.[141] The bending and stretching of the R^F-TENG during wearing promote friction among the omniphobic fibers of the textile, generating additional charges that increase the voltage difference between the top and bottom AgNFs electrodes (**Figure 3.10**e). The voltage peaks generated by the R^F-TENG can be easily rectified and used to power miniaturized electronic components connected using conductive textile threads and embedded into the e-textile during the embroidery process (**Figure 3.10**c). The omniphobic surface of the R^F-TENG renders them insensitive to environmental moisture (**Figure 3.10**d), protecting the embedded electronics from corrosion by washing.

Fluorinated materials have also been demonstrated to repel the adhesion of bacterial pathogens such as *C. albicans*, *P. aeruginosa*, and *E. coli*.[142] As a consequence, several hydrophobic coatings have been developed to inhibit the growth of microbes on textiles during their use or storage, since these microorganisms negatively affect the wearer and the textile.[143,144] To evaluate the antimicrobial repulsion mechanism of R^FTENG-based e-textiles toward *S. aureus*, untreated pieces of cotton (control samples) and omniphobic pieces of cotton (R^F-cotton) were cultured for seven days in the presence of *S. aureus*. Scanning electron microscopy (SEM) of the control and omniphobic samples indicate that *S. aureus* is repelled from the surface of the R^F-cotton and unable to proliferate. To confirm the reduction in *S. aureus* observed by SEM, we quantified the number of viable cells on pieces of R^F-TENG using a Bactiter-Glo assay by measuring the amount of ATP present on the samples after cell lysis. **Figure 3.10**b shows the quantification of *S. aureus* colony

forming units (CFU) present on the surface of the untreated and R^F-cotton samples after culturing for seven days (see Materials and Methods for antibacterial characterization details).

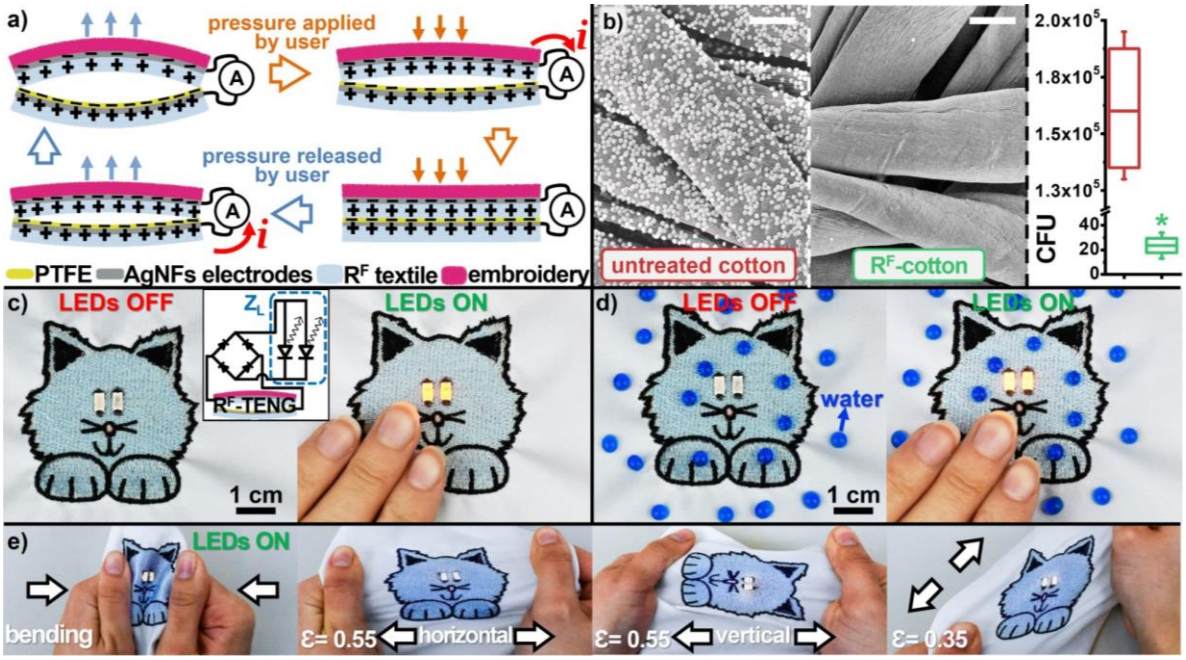

Figure 3.10 Production of electric energy and bacteria repellency of omniphobic e-textiles powered by R^F-TENGs. a) Schematics of the charge generation process in an R^F-TENG. b) Scanning electron micrographs of the control (untreated cotton) and omniphobic R^F-cotton samples after seven days of growth in media with *S. aureus* (scale bars 10 µm). Graph showing the reduction of *S. aureus* growth, colony forming units (CFU), on R^F-cotton samples compared to control samples, quantified using Bactiter-Glo (* indicates $p < 0.05$, error bars ± SD; n = 7), after culturing for seven days. c) R^F-TENG with the shape of a cat powering two LEDs embroidered as eyes. d) R^F-TENG operating while being covered with several droplets of blue-dyed water. e) Biomechanical energy harvesting by bending and stretching R^F-TENGs (LEDs on in all pictures).

3.3.3 Conversion of Mechanical Energy into Electric Energy using R^F-TENGs

Figure 3.11 electrical output characteristics of a textile-based R^F-TENG with a surface area of 6.25 cm^2. The triboelectric voltages generated every time the user taps the R^F-TENG are ~300 V (**Figure 3.11**a and **Figure 3.7**). The short-circuit current produced by each tap is ~80 µA (**Figure 3.11**c). Embedding a full-wave rectifier into the embroidered design (**Figure 3.10**c) reverses the negative voltages and currents generated by the R^F-TENG as shown in **Figure 3.11** b and d, respectively. The rectified open-circuit voltages (~270 V) and short-circuit currents (~72 µA)

generated by textile-based R^F-TENGs with two single-layer electrodes, are comparable to those of tribogenerators with multilayered electrodes and nanotexturized surfaces.[75,145] **Figure 3.11**e shows the effect of the external load on the voltage and current outputs of the textile-based R^F-TENGs. As expected, when the external load increases, the current output through the load decreases, while the output voltage increases.[2] The output power density of R^F-TENGs reaches a maximum of ~600μW/cm^2 when coupled to an impedance matching load of 1 MΩ (**Figure 3.11**f).

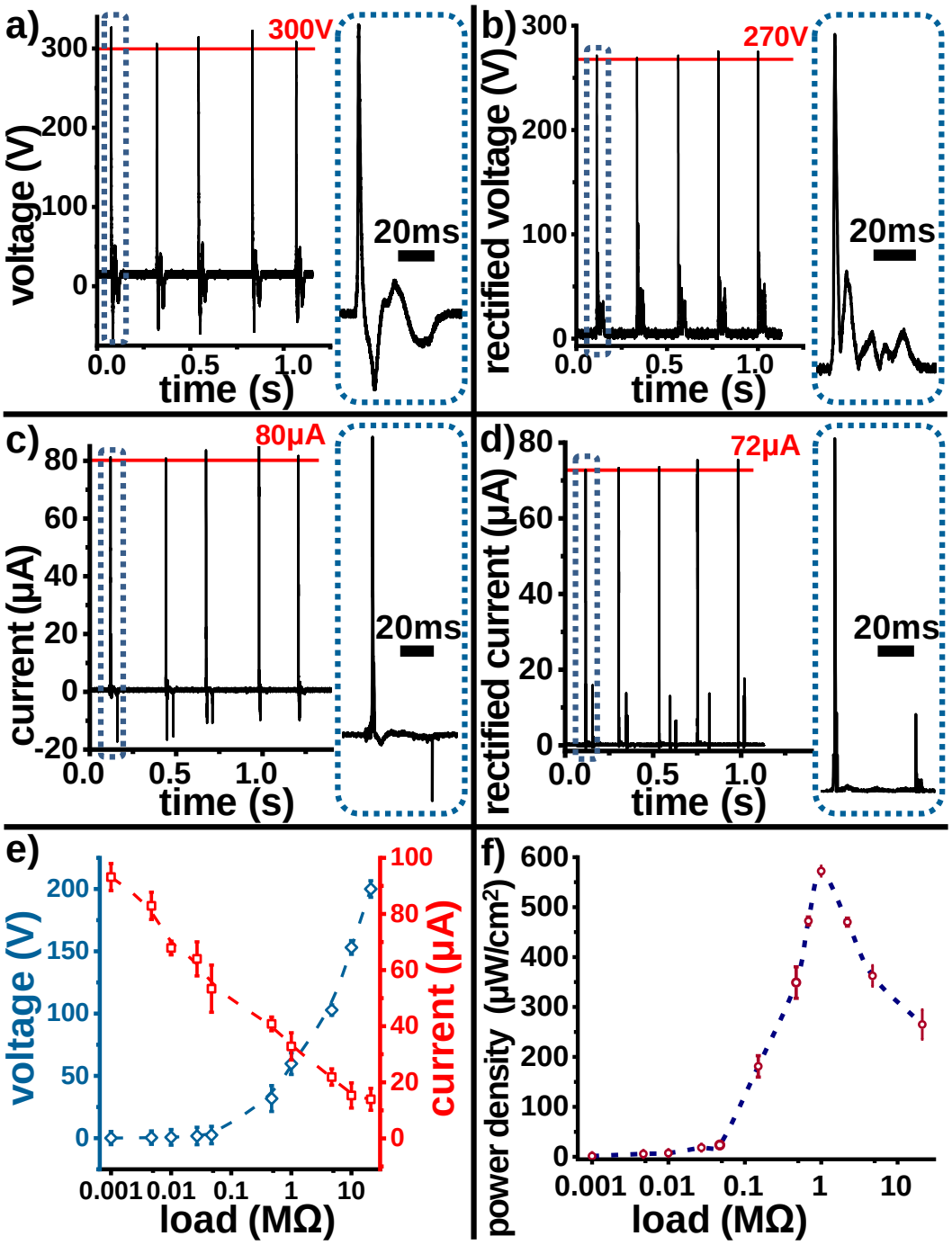

Figure 3.11 Production of electric energy using a 6.25 cm^2 R^F-TENG.
a) Open-circuit voltage peaks (before rectification) generated by tapping the R^F-TENG with two fingers at a frequency of ~4 Hz. b) Open-circuit voltage peaks rectified using the circuit shown in **Figure 3.10**c. c) Short-circuit current peaks (before rectification) generated by tapping the R^F-TENG with two fingers at ~4 Hz. d) Short-circuit current peaks after rectification. e) Dependence of the output voltage and output current on the external load. f) Dependence of the output power density on the external load.

3.3.4 Stain Repellency and Machine-Washing Resistance of R^F-TENGs

We used three commercially available fluoroalkylated organosilanes (C_8^F, C_{10}^F, C_{12}^F, see Experimental Section for details) to evaluate the effect of the chain length of the organosilane on the wetting properties of the e-textile for water (surface tension 72.8 mN/m) and hexadecane (surface tension 27.05 mN/m). The apparent static contact angle of water ($\theta_{app}^{H_2O}$) on cotton, spandex, and wool ranged from 150°–160° increasing proportionally with the roughness of the textile.[129] This correlation between the roughness of the textile and the apparent static contact angle is also observed for hexadecane ($\theta_{app}^{C_{16}H_{34}} = 95° - 125°$, **Figure 3.12**a). The θ_{app} of each functionalized fabric increases with the chain length of the organosilane, while the contact angle hysteresis ($\theta_a - \theta_r$) varies from 5°–20° for both water and hexadecane and decreases with the chain length. While the voltage output of R^F-TENGs did not show any noticeable trend with the chain length of the fluorinated organosilane, we chose C_{12}^F to render both the R^F-TENG and the e-textile omniphobic to maximize their stain repellency, which is inversely proportional to the contact angle hysteresis. **Figure 3.12**a illustrates how aqueous solutions and organic liquids with surface tensions as low as 27.05 mN/m (hexadecane) do not wick into C_{12}^F-treated e-textiles and can be easily cleaned by wiping them with an absorbent paper towel. Additionally, due to the omniphobic nature of R^F-TENGs, their energy-harvesting performance is not significantly affected by changes in environmental relative humidity (**Figure 3.4**).

We tested the washing durability of e-textiles powered with R^F-TENGs by laundering in repeated (50) standard washing cycles using 2 kg of clothes as ballast (see Experimental Section).[86] **Figure 3.12**b shows how, after 50 washing cycles, R^F-TENGs can charge a 2 mF capacitor through a diode bridge rectifier (electronic components embedded in the e-textile) without any significant decrease in performance. The maximum voltage across the capacitor after 18 s of continuous tapping (tapping frequency 4 Hz, pressure ~0.47 psi) is proportional to the size of the R^F-TENG and therefore to its maximum output voltage (**Figure 3.5** and **Figure 3.6**). After the vigorous spinning and abrasive action of the ballast during 50 washing cycles, the minimal change in $\theta_{app}^{H_2O}$ of omniphobic e-textiles indicates that the silanization remains stable, which helped to protect the embedded electronic components from corrosion during the washing cycles (**Figure 3.12**c). We also verified that $\theta_{app}^{H_2O}$ is not significantly affected after the immersion of the R^F-TENGs in water

for 24 h (**Figure 3.3**). We attribute the small decrease in open-circuit voltage and short-circuit current of the R^F-TENG after washing to the effects of the mechanical fatigue on the electrical interconnects inside the R^F-TENG, which resulted in higher contact resistance values. Note that the performance of R^F-TENG-embroidered e-textiles is affected by the drying cycles of commercial dryers, since the continuous heat and friction among the clothes cause the shrinking of the textiles and the fraying of the embroidery layer, exposing the AgNF electrodes to degradation after a few washing/drying cycles. Therefore, to extend the washing durability of R^F-TENG-embroidered e-textiles, we opted to hang them dry in room conditions (and not in a dryer) before subsequent characterization.

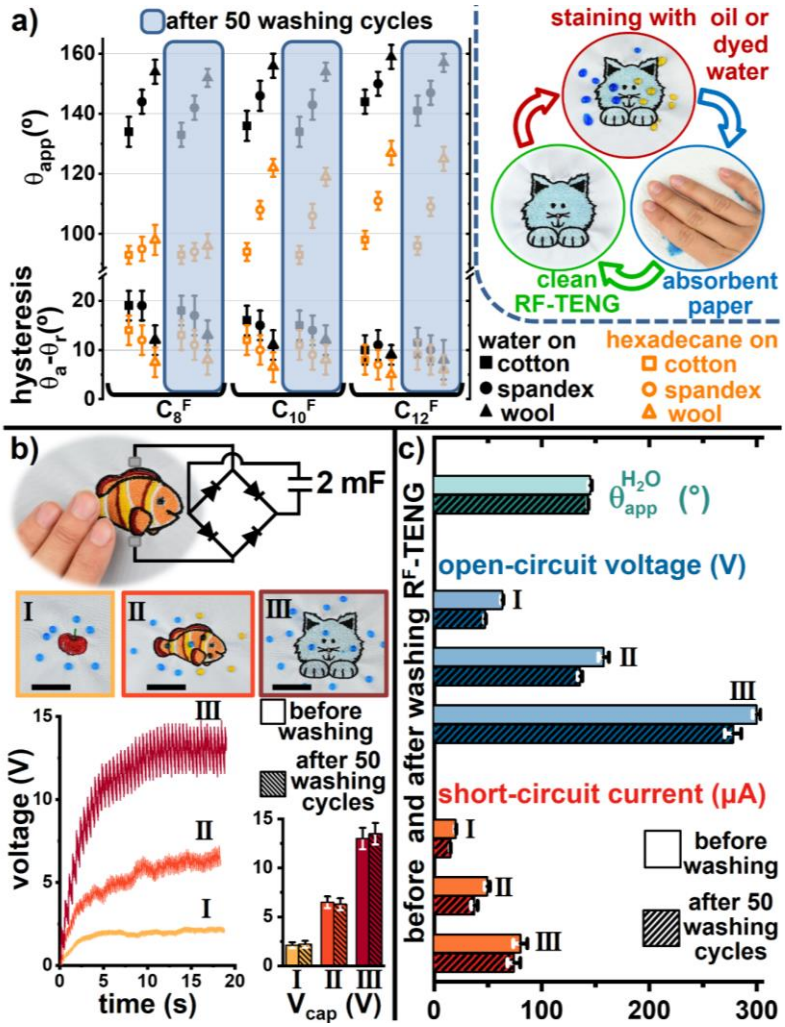

Figure 3.12 Washing durability of e-textiles powered by R^F-TENGs. a) Comparison of the apparent static contact angle θ_{app} and the contact angle hysteresis ($\theta_a - \theta_r$) of water and hexadecane on three textiles (cotton, spandex, and wool) with different functionalizations (C_8^F, C_{10}^F, and C_{12}^F), before and after 50 cycles of standard machine washing. The inset shows the stain repellency of these omniphobic textiles to hexadecane and dyed water, which can be cleaned by bringing them into contact with an absorbent paper towel. b) Charging curves of a 2 mF capacitor embedded in cotton-based R^F-TENGs of different sizes (I- cherry design ~2.25 cm^2; II- fish design ~4.5 cm^2; III- cat design ~6.25 cm^2; scale bars 2 cm), before and after 50 cycles of washing. V_{cap} indicates the voltage at the capacitor after 18 s of tapping. c) Measurements of the $\theta_{app}^{H_2O}$, the open-circuit voltage, and the short-circuit current of the R^F-TENGs shown in (b), before and after 50 cycles of washing.Harvesting Biomechanical Energy using R^F-TENGs

The embroidery of textile-based R^F-TENGs on conventional cloth items makes it possible to harvest energy from the natural motions of the wearer (**Figure 3.13**) without compromising comfort. As an example, **Figure 3.13**a shows human body energy harvesting from walking with a textile R^F-TENG embroidered on the bottom of a woolen sock (where they provide additional padding to maximize the comfort of the user). Similarly, R^F-TENGs can serve as decorations for shirts, where they can harvest energy when the arms get into rubbing contact with their surface (**Figure 3.13**b). Additionally, thanks to the flexibility and stretchability of the R^F-TENGs, they can be used to fabricate elbow patches capable of harvesting energy from the bending of the arm, due to the relative sliding of the top and bottom electrodes of the R^F-TENG (**Figure 3.13**c).

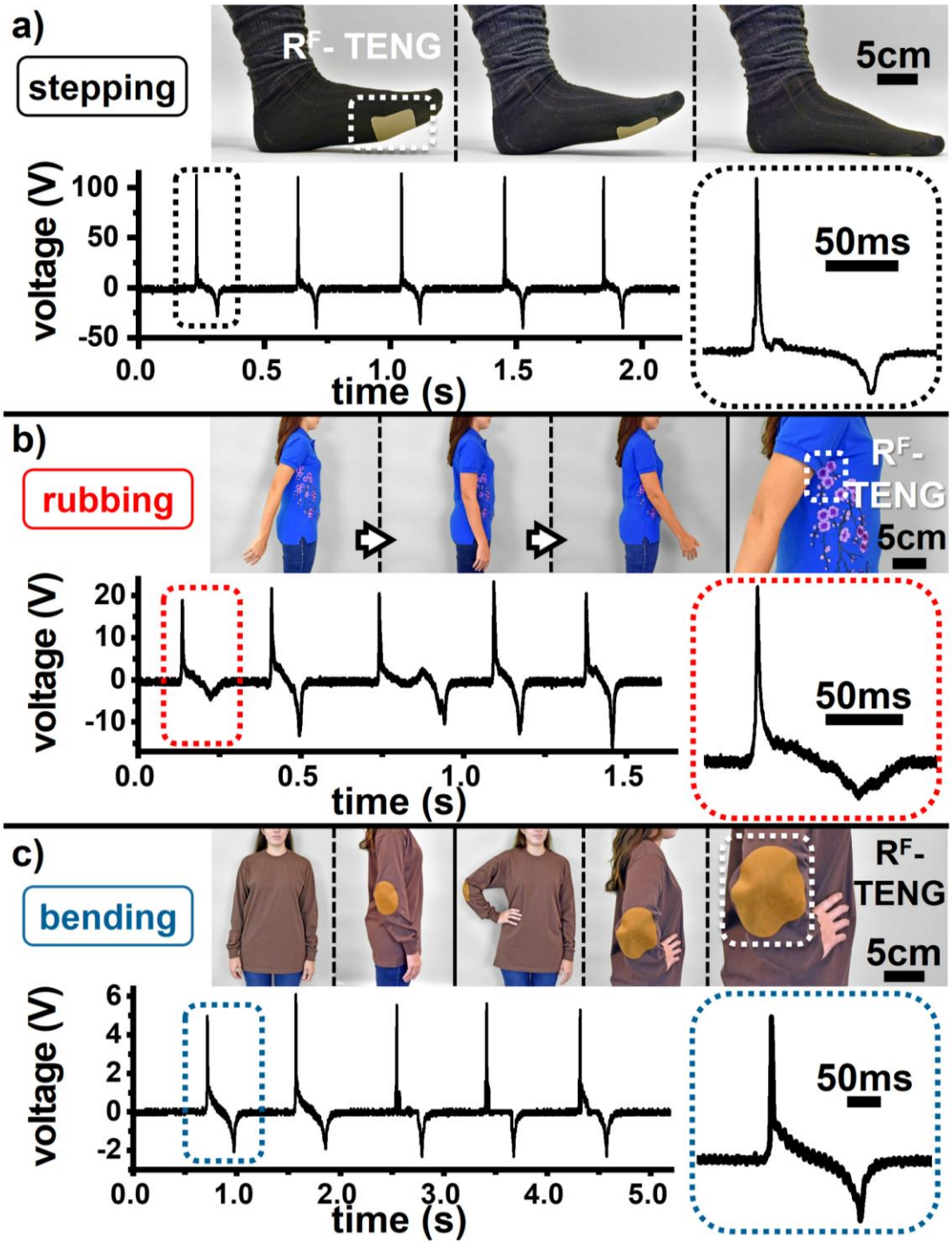

Figure 3.13 Biomechanical energy harvesting using R^F-TENGs. a) Output voltage generated by one R^F-TENG embroidered on the bottom of a sock during walking. b) Output voltage generated by rubbing the arm against the surface of an R^F-TENG embroidered on the side of a polo shirt. c) Output voltage generated by an R^F-TENG elbow patch upon repetitive bending of the elbow.

3.3.5 R^F-TENGs as Human-Machine Interfaces

The embroidered structure of the textile R^F-TENGs can produce fashionable, comfortable, washable, and self-powered e-textiles with triboelectric interfaces for user interaction. **Figure 3.14** shows a self-powered polo shirt comprising two R^F-TENGs placed under the arms on both sides of the shirt (see **Figure 3.13**b) and two self-powered triboelectric interfaces (on the collar of the shirt; **Figure 3.8**) that can change the volume, pause, and resume a song played by a music player integrated in the textile. Each triboelectric interface has different sensing areas embroidered using threads of different colors (light and dark blue) and raised patterns of different heights to facilitate tactile perception. The user can play and pause songs by gently pressing the two triboelectric sensing areas on the right side of the collar of this e-textile (**Figure 3.14**b). Similarly, on the left side of the collar, the user can slide their fingers up or down over the long triboelectric area to increase or decrease the volume of the playing song and mute the song by pressing the short triboelectric area (**Figure 3.14**c). We used this e-textile after 50 washing cycles without apparent damage or degradation in performance.

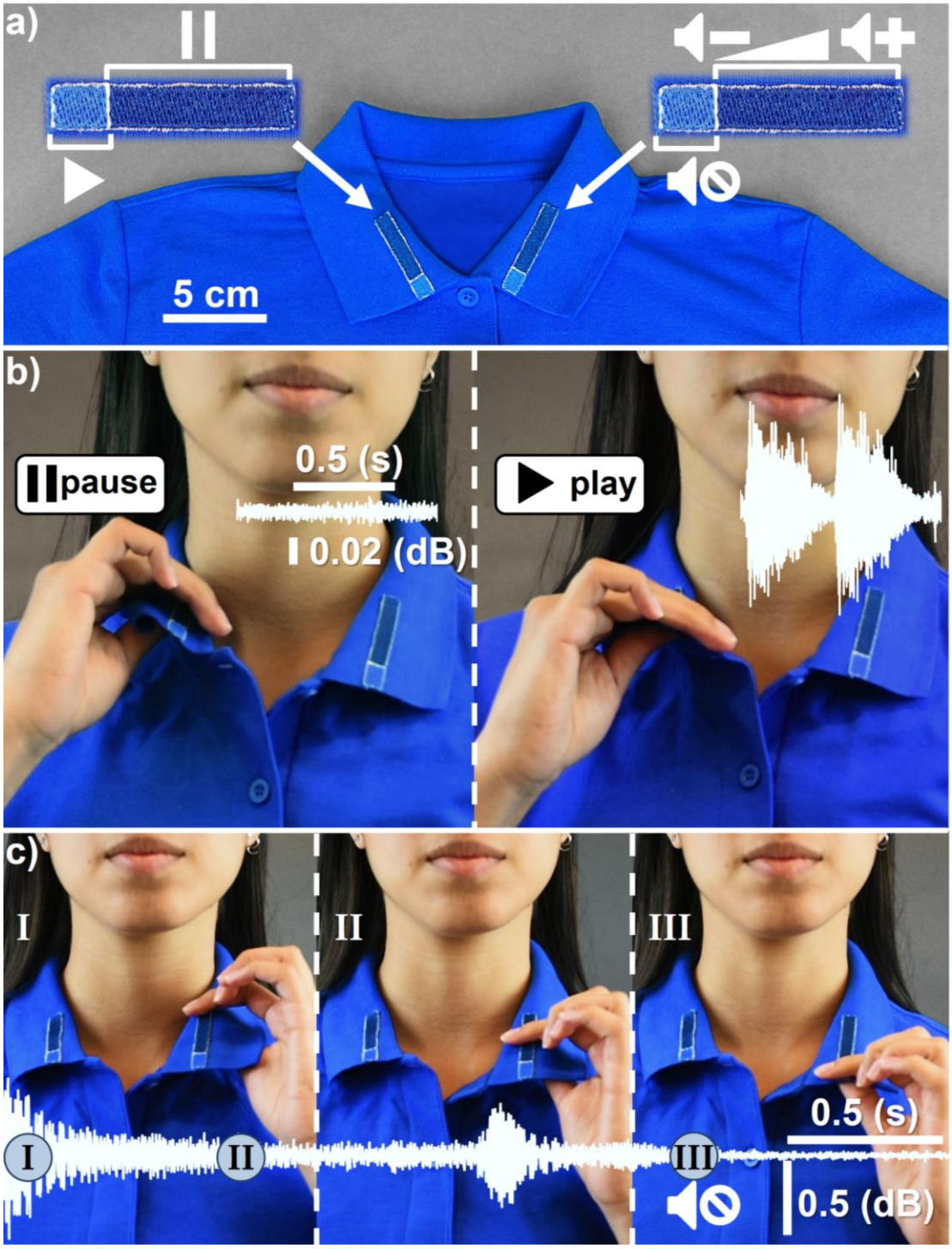

Figure 3.14 Self-powered audio control interface based on R^F-TENGs.

a) R^F-TENG-based controllers embroidered on the polo shirt shown in Figure 5b. b) Double-tapping the top part of the right controller pauses the music; double-tapping its bottom part resumes the music playback. c) Dragging the finger down from the top part of the left controller gradually lowers the music volume, all the way to mute.

3.4 Conclusions

In summary, this work demonstrates a simple and scalable method to transform conventional garments or textiles into omniphobic and self-powered e-textiles capable of powering embedded electronic systems using the electrostatic energy generated by the natural motions of the wearer. These e-textiles harvest biomechanical energy using omniphobic, fabric-based, triboelectric nanogenerators (R^F-TENGs) fabricated, at a low cost (<0.04$/cm^2; see **Table 3** and **Table 4**), by combining textile-mounted electronics with embroidery and the spray-based deposition of silanizing agents, highly networked AgNFs, and a conformable PTFE encapsulating solution. The resulting R^F-TENGs are lightweight, flexible, breathable (air permeability 90.5 mm/s), and can generate high output power densities (~600 μW/cm^2). The omniphobic silanization of these textiles prevents bacterial proliferation and repels staining by aqueous solutions and organic liquids with surface tensions as low as 27.05 mN/m, rendering R^F-TENGs insensitive to changes in the environmental moisture. The omniphobic embroidery design used to assemble R^F-TENGs protects both the textile-mounted electronic components and the electrodes of the R^F-TENGs from moisture and over-stretching (ε_{max} = 55%), conferring these R^F-e-textiles with excellent stability under mechanical deformations and remarkable washing durability after 50 standard machine-washing cycles. Moreover, thanks to the embroidery design, the user can easily pinpoint the location of the R^F-TENGs, enabling their use as self-powered tactile interfaces to control embedded electronics. Finally, the combination in the same textile of several R^F-TENGs, some serving as biomechanical energy transducers and some as tactile sensors, enables the creation of battery-free e-textiles controlled by the wearer. We envision that the versatility of the proposed fabrication method to create omniphobic e-textiles and its compatibility with large-scale production processes, such as spray deposition, will pave the way toward the cost-effective manufacturing of robust e-textiles and wearable human-machine interfaces for emerging applications.

4. WASHABLE, BREATHABLE, AND STRETCHABLE E-TEXTILES WIRELESSLY POWERED BY OMNIPHOBIC SILK-BASED COILS

Motivation and rationale: The commercial development of smart garments is currently hindered by significant challenges, such as dependence on batteries, reduced washability, and difficult incorporation into existing large-scale textile manufacturing technologies. This work describes an industrially scalable approach to transform conventional fabrics into smart textiles—wirelessly powered by omniphobic silk-based coils (OSCs). OSCs are stretchable and lightweight power-receiving coils that can be easily sewn onto any textile, enabling the safe wireless powering of wearable electronics *via* magnetic resonance coupling without compromising the comfort of the user. OSCs are composed of microfibers made of a novel silk-nanocarbon composite that benefits from the stretchability of silk fibroin and the high conductivity of multiwall carbon nanotubes and chitin carbon nanoflakes. These conductive silk fibers were previously developed by Dr. Ramses V. Martinez, and they were used in this study to fabricate the OSCs, which enable advancements on the wirelessly powering of e-textiles. The surface of the OSC-powered electronic textiles (e-textiles) is rendered omniphobic—both hydrophobic and oleophobic—using a spray-based silanization method, which imbues the e-textile with waterproof and stain repellent properties without compromising its flexibility, stretchability, or breathability. OSCs exhibit excellent stability in high moisture environments and under mechanical deformations, allowing them to undergo 50 standard machine-washing cycles without degradation in performance. Moreover, OSC-powered e-textiles can be fabricated at a low cost using scalable manufacturing processes, paving the way toward the rapid development and commercialization of machine-washable and battery-free smart clothing and reusable wearable electrophysiological sensors.

4.1 Introduction

We present a scalable method to fabricate omniphobic silk-based coils (OSCs), which can be integrated into conventional textiles by sewing and can be used for the continuous wireless powering of electronic components *via* magnetic resonance coupling. We used a thread composed by multiwall carbon nanotubes (MWCNTs) and chitin carbon (ChC) with silk fibroin (SF) that is stretchable and conductive and can be sewn onto a variety of textiles in the shape of a flat spiral

coil and rendered omniphobic by the spray-based deposition of fluoroalkylated organosilanes, creating OSCs. We demonstrate that OSCs are flexible, stretchable, washable, and capable of continuously providing power to e-textiles *via* wireless power transfer. We also demonstrate that the power output of OSCs does not diminish significantly after repeated mechanical deformation and washing cycles, enabling the continuous wireless powering of wearable sensors embedded into e-textiles. The combination of stretchability, high conductivity, independence from environmental moisture, and relative low cost, outperforms the WPT capabilities of several silver and carbon-based yarns proposed for the manufacturing of washable e-textiles [146]. We expect the WPT efficiency of OSCs to expedite the sustainable development and commercialization of emerging, battery-free, wearable electronics and e-textiles.

4.2 Materials and Methods

4.2.1 Fabrication of OSCs using SF/MWCNTs/ChC Microfibers

We used a ~350μm-thick SF/MWCNT/ChC thread to fabricate the OSCs; and since MWCNTs, ChC, and SF are biodegradable materials [147–149], we expect the fabricated OSCs to contribute to the development of future biodegradable e-textiles. We designed and sewed the OSCs in a serpentine pattern (**Figure 4.1**) to enhance their performance upon stretching [150–153]. We chose the curvature angles of the serpentine pattern ($\alpha_1 = 90^o$ and $\alpha_2 = 135^o$), to ensure that the WPT efficiency of the OSC increases (rather than decrease) when stretched up to strains of ~10% (**Figure 4.19**d; for reference, the maximum shear strain that the human skin can sustain is ~11%; [154]). Moreover, the choice of this serpentine pattern allows the WPT efficiency to remain within 70% of its maximum possible value up to strains of 50% (for reference, the maximum longitudinal strain that the human skin can sustain is ~30%; [155]); see **Figure 4.19**c, d.

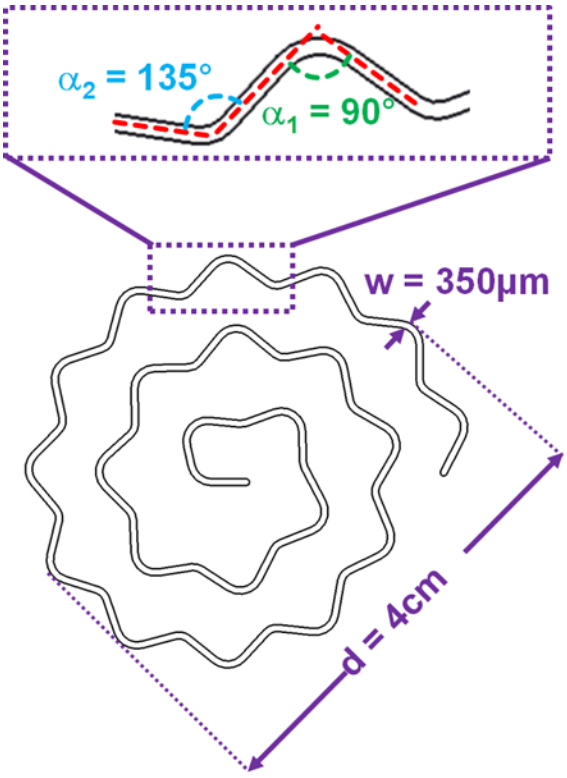

Figure 4.1. Serpentine design used in the fabrication of OSCs.

OSCs reported in this manuscript have a resistance in the range 80–90 Ω/m (at the optimized composition of 90 wt% SF with 7 wt% MWCNT and 3 wt% ChC; see **Figure 4.17**c), can withstand strains up to 500% (see **Figure 4.17**a), and maintain an apparent static contact angle of ~158° even after 50 cycles of machine washing (**Figure 4.21** and **Figure 4.12**). As a comparison, commercial silver-coated yarns have resistances ranging 50–150 Ω/m (dry) and limited stretchability (strain at failure ε_f <20%). Additionally, the resistance of these yarns increases ~100−300% over 50 wash cycles, as silver oxidizes in the presence of moisture [156]. Commercially available carbon fibers exhibit resistances of ~1K Ω/m and, while they can be very tough, their stretchability is limited (~8%) [157]. Recently reported yarns based on carbon (reduced graphene oxide) exhibit resistances as low as 12 Ω/m, but cannot endure stretching >30%, as the graphene oxide flakes cannot provide a tensile mechanical reinforcement as efficient as MWCNTs due to their aspect ratio [158,159]. The static contact angle of these graphene-based nanocomposites depends on their polymeric matrix resistances and oscillates between 60-110° [160].

We used a commercial sewing machine (EverSewn Hero; EverSewn Inc.) equipped with a USB port to import custom sewing designs with sizes up to 110 × 170 mm. Note that if the sewing machine patterns the OSC using a high sewing tension (tight stitches), this will cause the SF/MWCNT/ChC thread to experience near 90° bending on each stitch, which could compromise conductivity, particularly upon stretching. Since we aimed to fabricate highly flexible and stretchable e-textiles (stretchable up to ε=100%), we maintained the sewing machine tension low (4N), which resulted in bending angles of ~36° (**Figure 4.2**).After sewing the OSCs on the textile, we interface the ends of the coil with a miniaturize wearable impedance matching circuit using conductive epoxy (8331D, MG Chemicals Inc.). We further secured the electrical connection by coating them with a flexible epoxy adhesive (FlexEpox; TotalBoat Inc.).

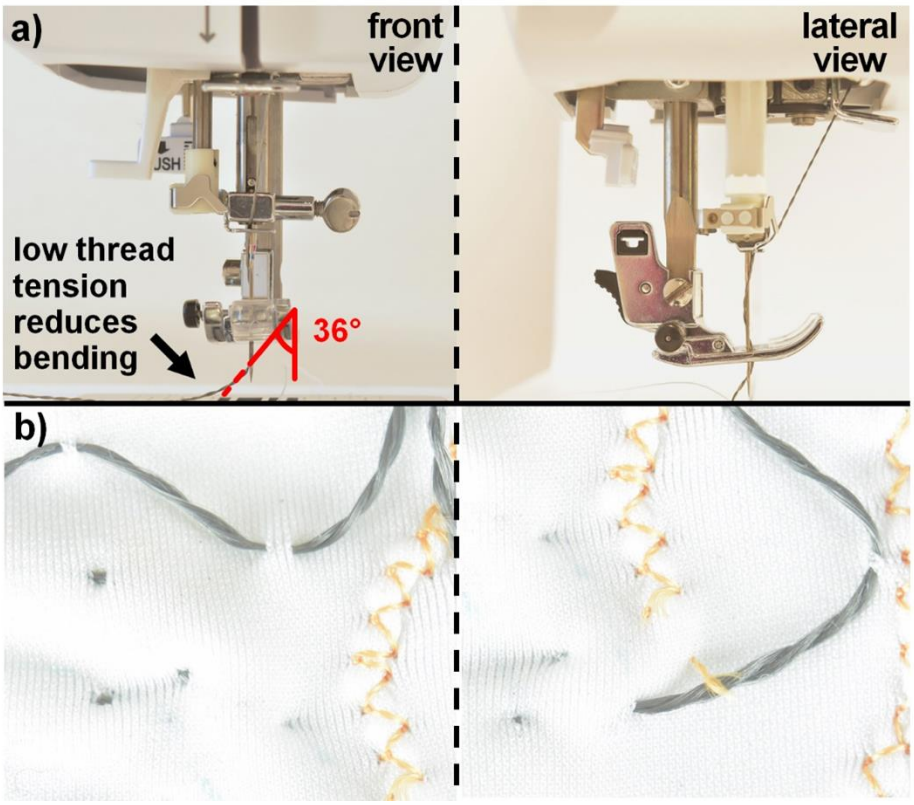

Figure 4.2 a) Image of the thread tension mechanism used to keep the SF/MWCNT/ChC thread at ~4 N tension during sewing. b) Image of the thread as it travels through a stitch, showing how the low sewing tension reduces the bending experienced by the conductive thread as it is sewn on the textile.

After silanizing the surface of the e-textile by spraying it with a 4.76% v/v solution of trichloro (3,3,4,4,5,5,6,6,7,7,8,8,9,9,10,10,11,11,12,12,12-henicosafluorododecyl)silane ($CF_3(CF_2)_9CH_2$-CH_2SiCl_3; "C_{12^F}") in isopropanol, the silane and the sub-10μm size of the fluorinated clusters attached to the e-textile (**Figure 4.3**) prevent water (and virtually any fluid with a surface tension ≥27.05 mN/m) [129] from contacting the surface of the SF/MWCNT/ChC fibers or the underlying textile. This robust silanization does not interfere with the gas transport through the textile (air permeability ~90.5 mm/s, **Figure 4.16**e) or limit its flexibility [134]. Additionally, the neglectable increase of radius and coefficient of friction of silanized threads makes OSCs compatible with current textile mass production technologies. Additionally, the neglectable increase of radius and coefficient of friction of silanized threads makes OSCs compatible with current textile mass production technologies.

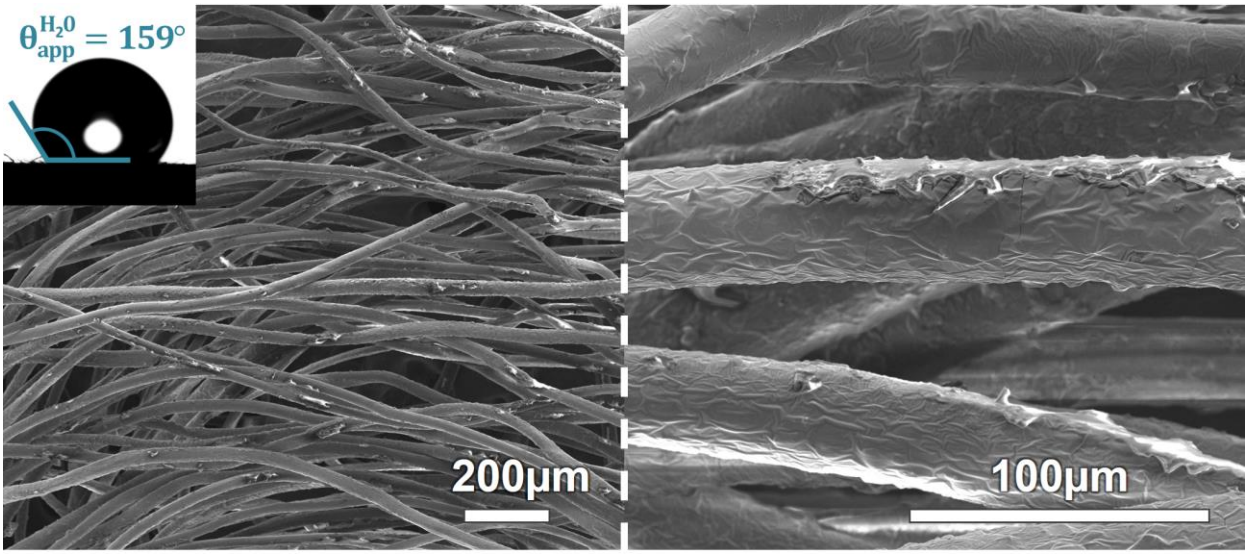

Figure 4.3 High-resolution SEM images of the fibers of a cotton textile rendered omniphobic by silanization with C_{12^F} Fluorinated polymeric clusters—generated by the reaction between the sprayed fluoroalkylated silane and the surface-bound water—can be found distributed over the cotton fibers, without significantly reducing the porosity or the gas permeability of the textile. The apparent static contact angle of a 10μL water droplet on omniphobic cotton is $\theta_{app}^{H_2O} = 159°$.

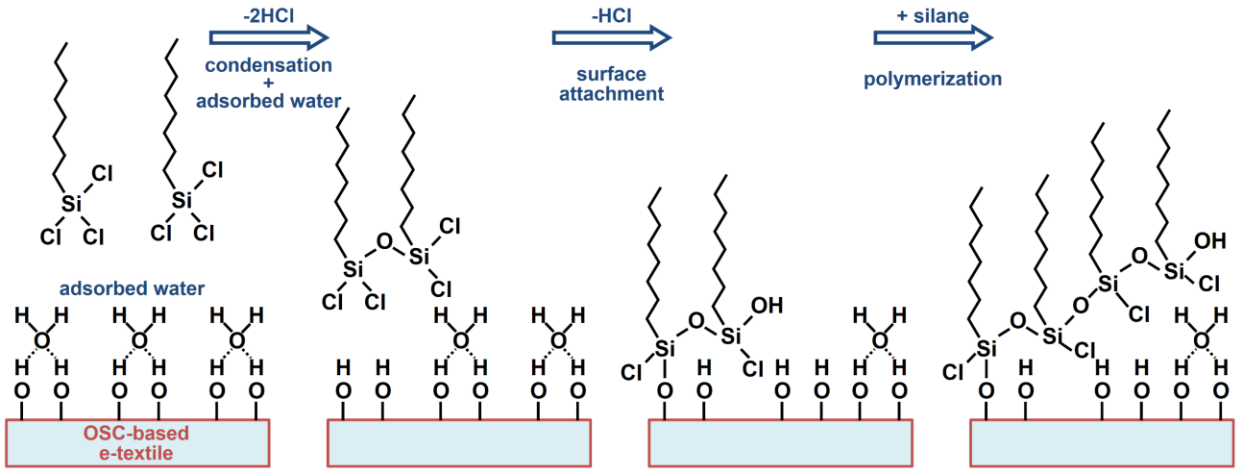

Figure 4.4 Covalent modifications of OSC and e-textile fibers [128].

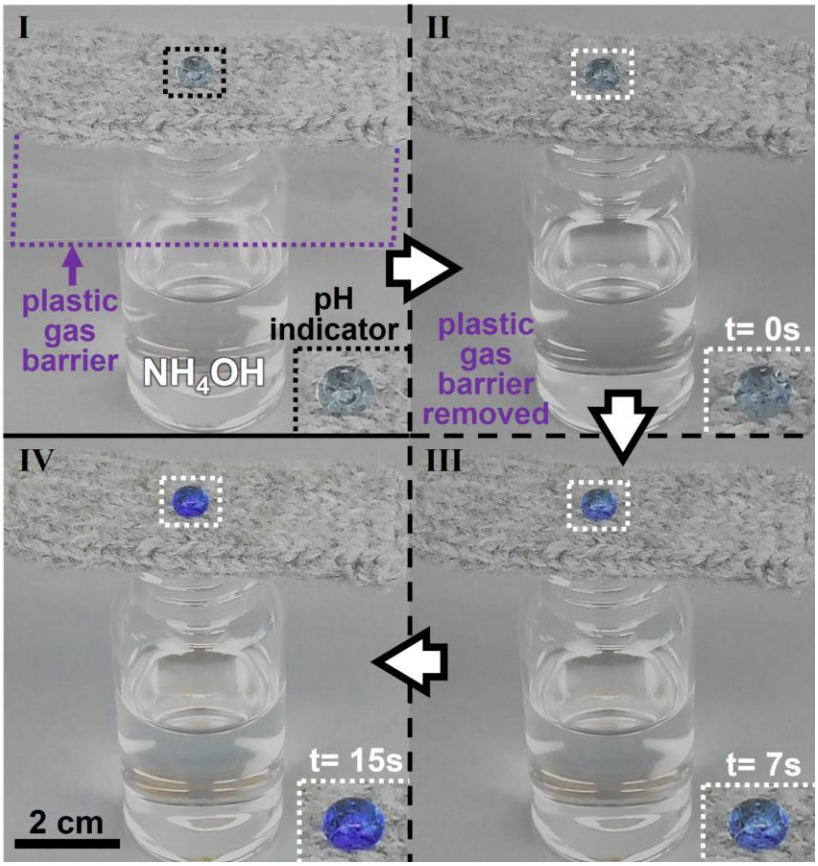

Figure 4.5 Gas permeability of an omniphobic OSC-powered e-textile (smart glove shown in Figure 4.16d and e, Figure 4.20c and d). We deposited a 10-µL drop of liquid pH indicator over the top surface of the omniphobic wool glove ($\theta_{app}^{H_2O} = 158°$), which rests on a plastic film (gas barrier) that separates the glove from an open scintillation vial containing NH_4OH (panel I). At t=0, the plastic film is removed, allowing the NH_3 gas in the solution to contact the glove, travel through its highly porous structure, and reach the pH indicator at the other side (panel II). The color of the pH indicator immediately begins to change from light blue (pH = 5) to dark blue (pH =10), a process that takes ~15s, as the NH_3 gas permeates through the omniphobic glove (panels II – IV). Structural Characterization of OSCs and Omniphobic E-textilesScanning Electron Microscopy

We used a scanning electron microscope (SEM; FEI Nova NanoSEM 200), operating at a working distance of 3–6 mm, to characterize the structure of the textile substrates and the conductive silk thread (**Figure 4.16**c) used in the fabrication of OSC-powered e-textiles. To facilitate charge dissipation during imaging, the textile substrates were mounted on an orbital rotation stage and coated with a ~20-nm-thick layer of platinum using a sputter coater (208HR, Cressington Scientific Instruments, UK) operating at a 40 mA filament current during 60s.

4.2.1.1 Fourier-Transform Infrared Spectroscopy

Fourier-Transform Infrared Spectroscopy (FTIR) spectra were collected using a 550 Nicolet Magna-IR Spectrometer. Fiber samples were placed over a 2-mm-thick ZnSe optical window and kept under a nitrogen atmosphere prior to the collection of the spectra. Each collected spectrum corresponded to the average of 180 scans in transmittance mode.

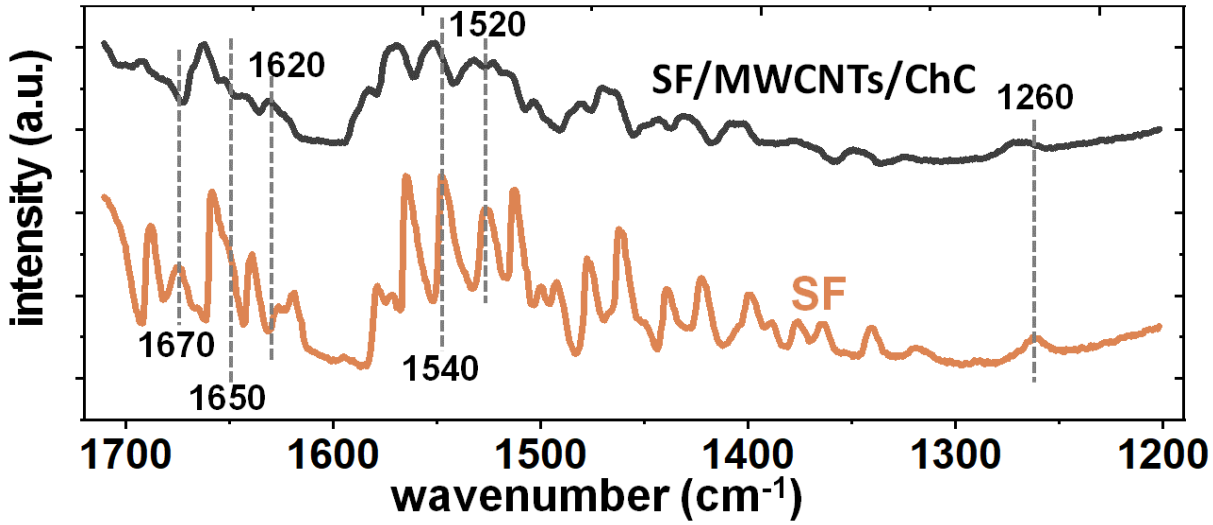

Figure 4.6 Comparison between the FTIR spectra of SF/MWCNTs/ChC microfibers and pure silk microfibers. The peaks identified in the graph indicate the presence of secondary structures (α-helix, β-sheet, and random-coil) in the SF.

4.2.2 Mechanical Characterization of OSCs

We characterized the mechanical performance of the SF/MWCNTs/ChC threads used to sew OSCs according to ASTM D2256 specifications using a universal testing machine (MTS Insight 10; MTS Systems Corp.), with a 1 kN load cell (model 661.18.F01), while applying tensile loads at a crosshead speed of 5 mm min^{-1}. We used at least eight samples with a length of 10cm to characterize the dependence of the properties of the conductive threads on stretching.

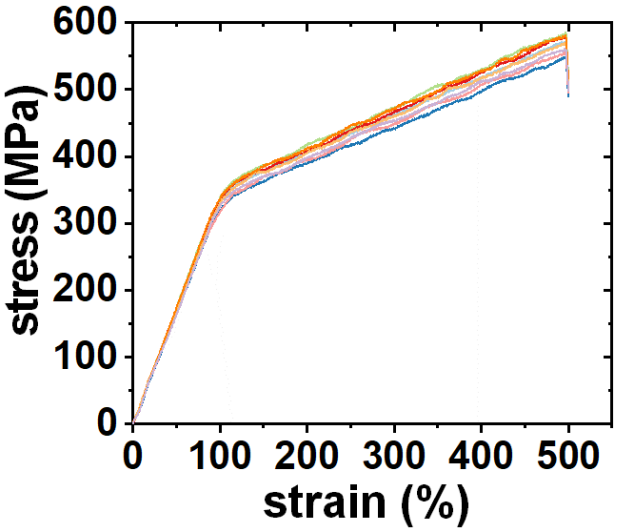

Figure 4.7 Stress-strain curves generated during the tensile testing of eight different 100-mm-long OSC threads.

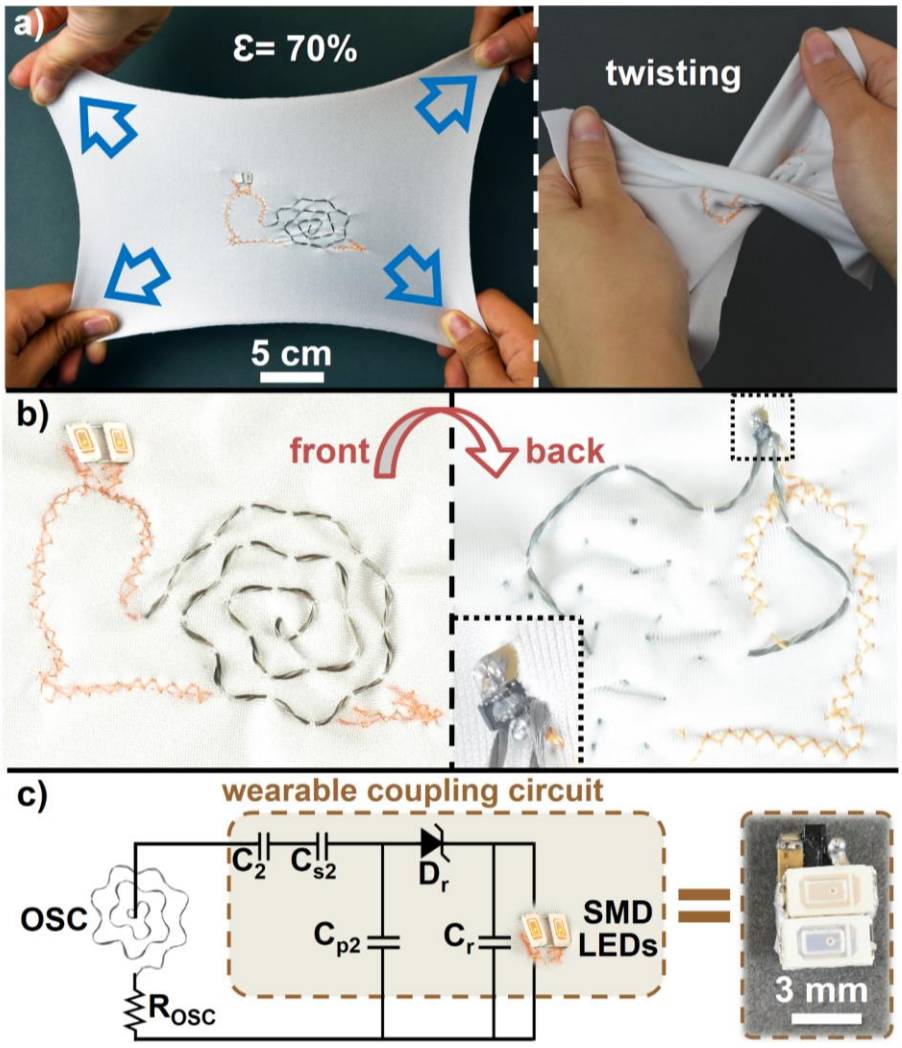

Figure 4.8 Stretchability and bendability of omniphobic OSC-based e-textiles.

a) OSC-powered e-textile shown in **Figure 4.18**b withstanding a strain e=70% in multiple directions, followed by 180° twisting without inducing damage to the sewn circuitry or suffering any noticeable degradation in performance. b) Pictures of the front and the back of the textile showing the electronic components, which weigh ~0.3g, and occupy an area of ~18 mm^2. c) Schematic diagram and actual picture of the wearable MRC circuit and the SMD LEDs (Z_L) comprising the e-textile, where C_2= 940 nF, C_{s2}= 80 nF, C_{p2}= 75 nF, C_r= 4700 nF, and D_r being a high frequency Schottky diode. Note that we use the sub index 2 to identify that this MRC circuit is applied in the wearable device (secondary coupling stage feed by the primary coil). We use the sub index "s" or "p" to identify elements connected in series or parallel with the OSC, respectively. The sub index "r" is used to identify the elements (a diode D_r, and a capacitor C_r) responsible for the rectification of the altern current induced by the primary coil on the OSC

4.2.3 Electrical Characterization of OSCs

We connected the primary coil powering the e-textiles to a vector network analyzer (E5071B ENA, Agilent Technologies) and characterized the OSCs passively by bringing them in the vicinity of the primary coil. We first measured the real and imaginary components of the impedance, $Z(f) = R(f) + jX(f)$; $|Z| = (R^2 + X^2)^{1/2}$, where the real part is the resistance (R) and the imaginary part is the reactance (X), as a function of the operating frequency (f) $\left(L = \frac{X}{2\pi f}\right)$, $\left(\theta = \tan^{-1}\left(\frac{X}{R}\right)\right)$ and $Q = \left(\frac{X}{R}\right)$ quality factor, see **Figure 4.10**.

The vector network analyzer records the fraction of power reflected by the OSC back to the primary coil ($|S_{11}|^2$) via a one-port measurement, from which the efficiency of the WPT is calculated as $\eta = (1 - |S_{11}|^2) \times 100\%$. We then performed impedance-matching to optimize the magnetic resonant coupling between the external coil and the OSC by introducing matching capacitances in series (C_{s1}= 280pF, C_{s2}= 80nF) and parallel (C_{p1}= 6nF, C_{p2}= 75nF) on their respective MRC circuits (**Figure 4.17**a). The value of these capacitances was determined using the bandpass filter theory described by Chappell et al.[161] As a result of this impedance matching, the WPT efficiency increases from ~1.5% to ~37% at 5.2 MHz (**Figure 4.19**b)

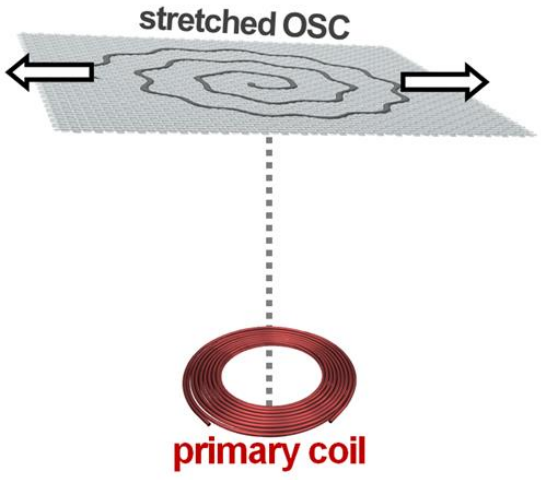

Figure 4.9 Schematics of the experimental set-up used to maintain the OSC axis collinear with the primary coil during the stretching characterization experiments.

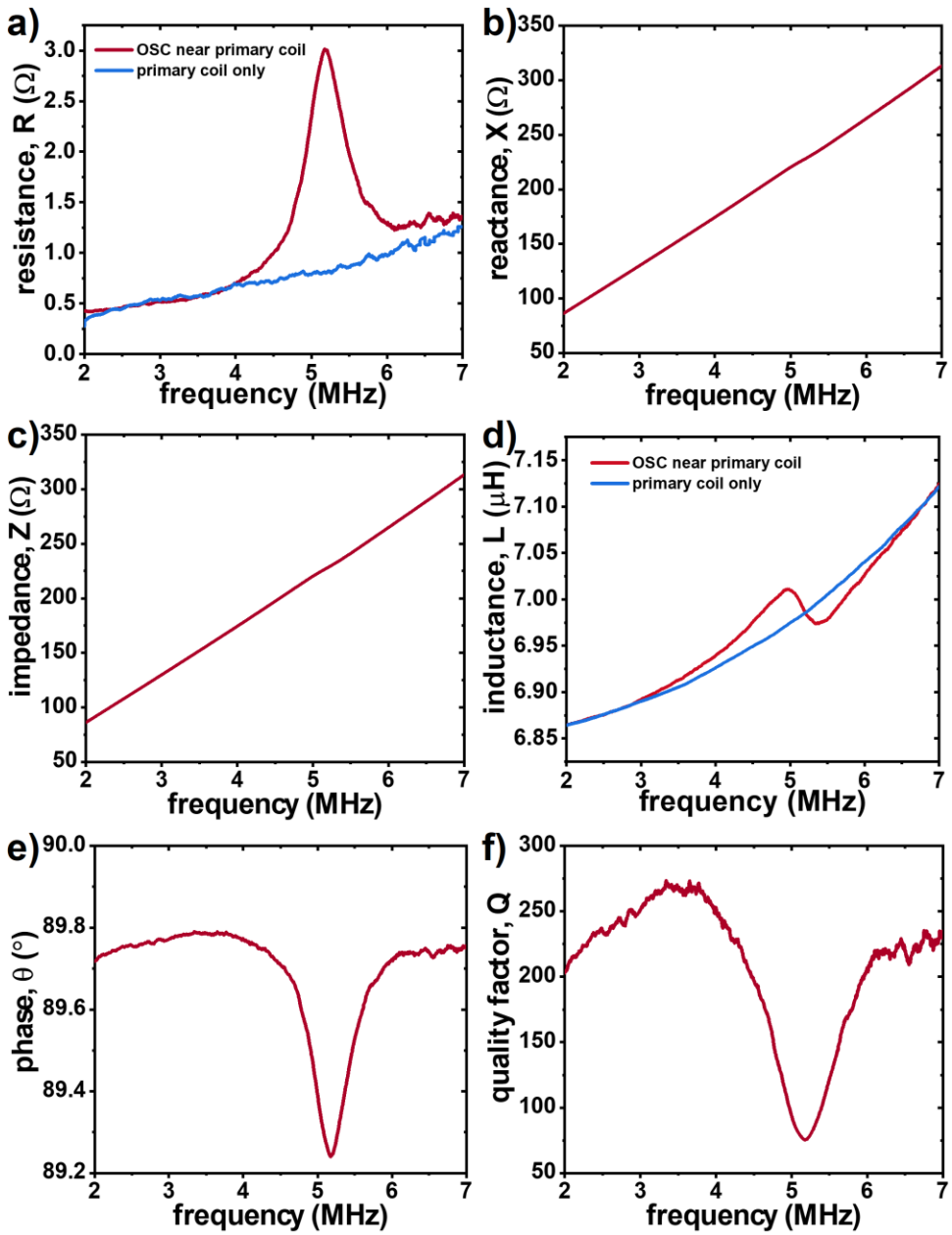

Figure 4.10 Frequency-dependent electrical characteristics of the wirelessly powered OSC-based e-textile (acquired passively from the primary coil side) shown in Figure 4.17b: a) Resistance (*R*), b) Reactance (*X*), c) Impedance (*Z*), d) Inductance (*L*), e) Phase (θ), and f) Quality Factor (*Q*).

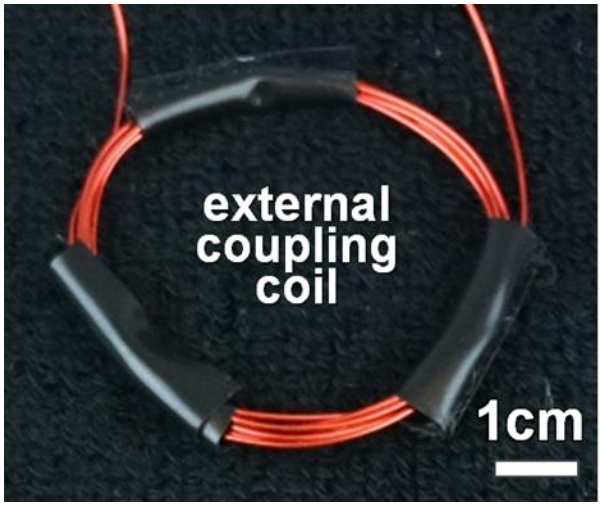

Figure 4.11 Image of the primary coil used for MRC WPT with OSCs presented in this work. The coil is 5cm in diameter and made of polymer enamel coated 27 AWG copper wire forming 6 turns.

4.2.4 Safety of Use of OSC-based e-textiles with respect to Human Exposure to Electromagnetic Fields

We followed the IEEE Standard for safety levels with respect to human exposure to electromagnetic fields to guarantee that the wireless power transfer to the OSC-powered wearable devices respects the safety limits established in the USA [162]. The maximum power per unit area allowed for wireless devices operating on a frequency range from 1.0 MHz to 30 MHz is given by $Max.\ Power\ Density\ (W/m^2) = 9000/f_M^2$, where f_M is the frequency of operation in MHz. Since all the OSC-powered e-textiles presented in this study operate at a frequency of 5.2MHz, the maximum power density that allows them to operate safely under the maximum exposure reference level (ERL) is 33.2 mW/cm^2. The table below demonstrates that all the wearable, OSC-powered, devices discussed in the main manuscript respect this ERL safety limit.

Table 5. Power and power density levels of OSC-based e-textiles, and maximum allowed safe power density level according to IEEE standard for safety with respect to human exposure to electromagnetic fields (1–30MHz).

Device	Seen in Figure	Total Power required (mW)	Power density received by the OSC (mW/cm^2)
OSC-based display with a "snail" design.	**Figure 4.18**b	120	9.55
OSC-based display with a "bike" design.	**Figure 4.18**c	120	9.55
OSC-based PPG sensor	**Figure 4.20**	155	12.33
OSC-powered Non-contact voltage detector	**Figure 4.21**	60	4.77
Maximum allowed safe power density level according to IEEE standard for safety with respect to human exposure to electromagnetic fields (1–30 MHz)[162].			**33.2**

4.2.5 OSC-powered wearable non-contact voltage detector

The non-contact voltage detection circuit mounted on the glove is composed by two bipolar junction transistors (BC547) that acts as a current amplifier system that can amplify the small current captured by the conductive embroidered glove fingerprint, and by another transistor which acts as a switch for the OSC that is powering the LED.

The current received by the NPN transistor connected to the glove fingerprint is amplified with a gain of β_1= 200, and it is further amplified by the next transistor with a gain of β_2= 200. This configuration is known as Darlington configuration and gives a much higher current gain

than using a single transistor. The gain of the Darlington ($\beta_{darlington}$) configuration of the non-contact voltage detector is given by the product of the individual gain of each transistor ($\beta_{darlington} = \beta_1 * \beta_2$).

We placed different OSC-powered e-textiles inside a commercial laundering machine (TR3000WN, Whirlpool) using 2kg of conventional textiles as ballast and followed the laundering test specifications dictated by the AATCC Test Method 135–2014. Each washing cycle consisted of 120L of water at 22°C (wash and rinse cycles) under an 8-min delicate laundering program. The spinning process reached ~120 rpm during washing and rinsing, followed by an additional 3 min of spinning under ~450 rpm. After cleaning, the textiles were hung and allowed to dry at room conditions.

To illustrate the laundry resistance of OSC-based wearable devices we characterized the non-contact voltage detection glove shown in **Figure 4.21** after 50 washing cycles. The omniphobic character of OSC-powered e-textiles allow them to operate even when fully immerged in water. **Figure 4.12** shows the fibrous structure of the wool as purchased, after silanization, and after 50 washing cycles. While the amount of fluorinated polymeric clusters coating the wool fibers reduces as a consequence of the shear action of the washing cycles (see **Figure 4.12** b and c), this degradation is not enough to modify the apparent static contact angle of water on the surface of the silanized wool ($\theta_{app}^{H_2O} = 158°$; see **Figure 4.12** b and d). Similarly, **Figure 4.13** shows how the electrical detection performance of the circuitry in this OSC-based e-textile remains unchanged after 50 washing cycles. The non-contact voltage detection capabilities of this glove—wirelessly powered through its OSC (**Figure 4.21**a)—depend both on the magnitude of the voltage connected applied to the cable and the distance separating the electrical cable from the fingertip of the glove (covered with an embroidered SF/MWCNTs/ChC conductive pad), see **Figure 4.13**a.

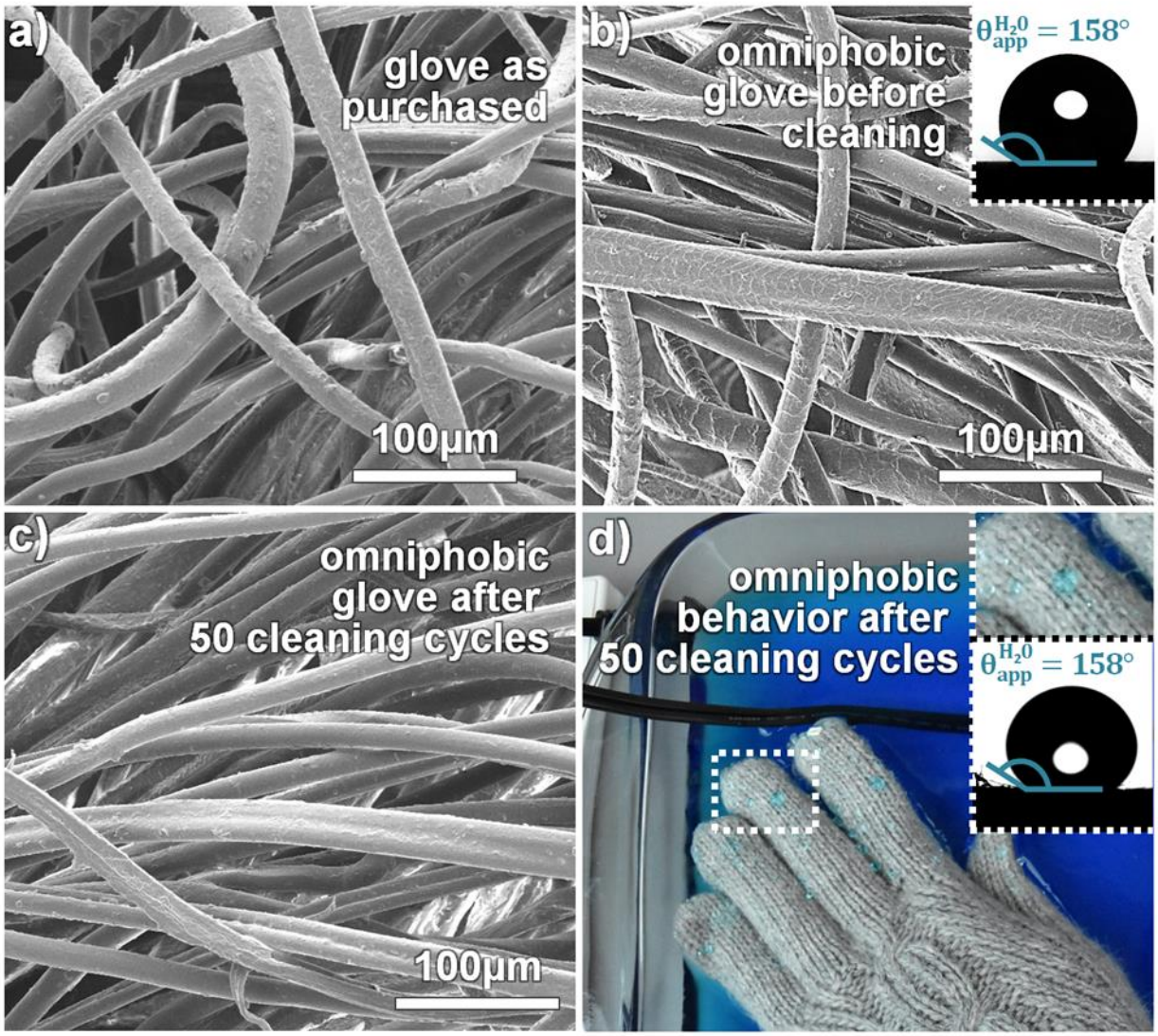

Figure 4.12 Laundry resistance of the wearable non-contact voltage detection glove. High resolution SEM image of the fibrous structure of the wool glove as purchased (a), after being rendered omniphobic by silanization with $C_{12}F$ (b), and after 50 washing cycles (c). d) The apparent static contact angle of a 10µL water droplet on this OSC-powered wearable device remains unchanged after 50 washing cycles.

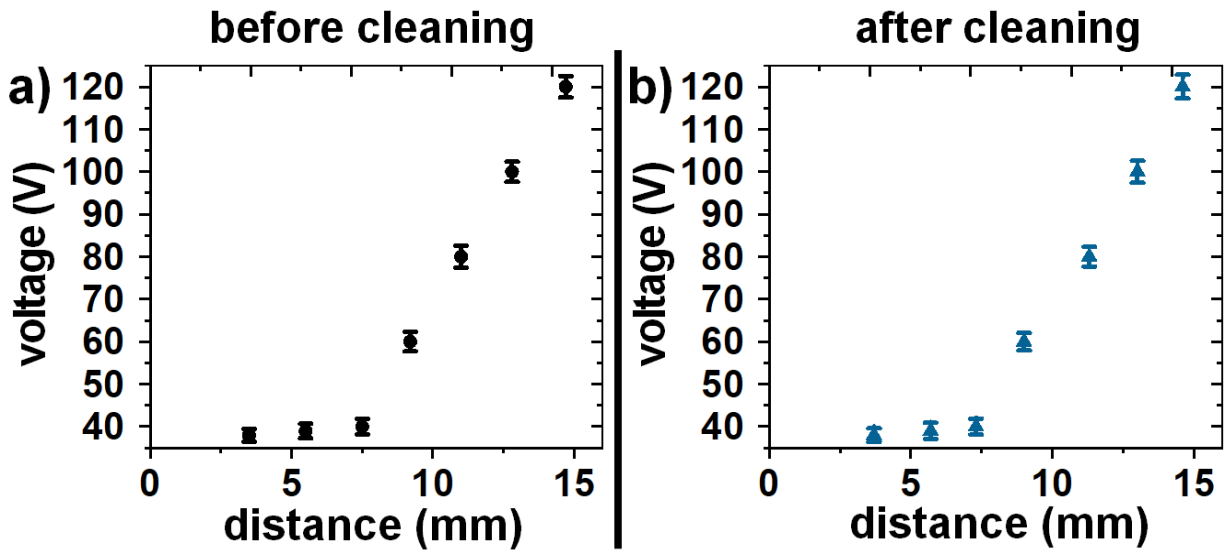

Figure 4.13. Dependence of voltage detected with the non-contact voltage detection glove shown in Figure 4.21 and Figure 4.12 on its separation from the cable before (a) and after (b) 50 cleaning cycles.

4.2.6 Wireless, Battery-free, PPG Wristband

Photoplethysmography (PPG) is a low-cost optical technique that can detect changes in the volume of blood flowing through blood vessels due to the rhythmic activity of the heart [163,164]. This blood volume change is measured by illuminating the skin of the user with a green SMD LED and collecting the reflected light using a SMD photosensor (see **Figure 4.20**). The amount of reflected light is proportional to the volume of blood circulating under the skin of the user. Therefore, by continuously collecting the reflected light from the skin of the user it is possible to identify different cardiac phases and associated parameters [165]. **Figure 4.14** shows a representative PPG waveform collected from a single cardiac cycle. This waveform is composed of the following sequence of peaks and valleys: the systolic peak, dicrotic notch, and diastolic peak. By identifying these peaks, other cardiac parameters can be calculated: pulse interval (PI), inflection point area ratio (IPAR), ΔT, crest time (CT), see **Figure 4.14**. These cardiac parameters have been commonly used to monitor cardiac output during exercise [166] and arterial stiffness due to aging [167].

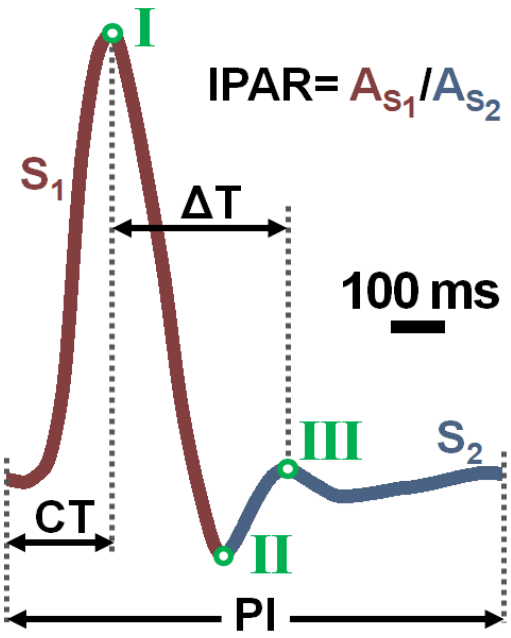

Figure 4.14 Information extractable from the PPG waveforms collected with the wearable OSC-based PPG sensor (single cardiac cycle). The waveform is composed of a systolic peak (I), a dicrotic notch (II), and a diastolic peak (III). The period of this PPG signal corresponds to the pulse interval (PI). Additionally, other relevant cardiac parameters can be extracted from this waveform, such as ΔT, the crest time (CT), and the inflection point area ratio (IPAR; ratio between the area under the S_1 and the S_2 regions) [165].

Figure 4.15 shows a high-resolution SEM image of the C_{12}^F-silanized wristband, where a PPG sensor, a low-power microcontroller and Bluetooth chip is integrated into a textile wristband. We used conductive epoxy (8331D, MG Chemicals Inc.) to connect the terminals of the OSC to the flexible miniaturized electronics embedded in the textile (**Figure 4.8**). The electronic components weigh ~12 g, and occupy an area of ~540 mm^2, minimally affecting their somatosensory perception.

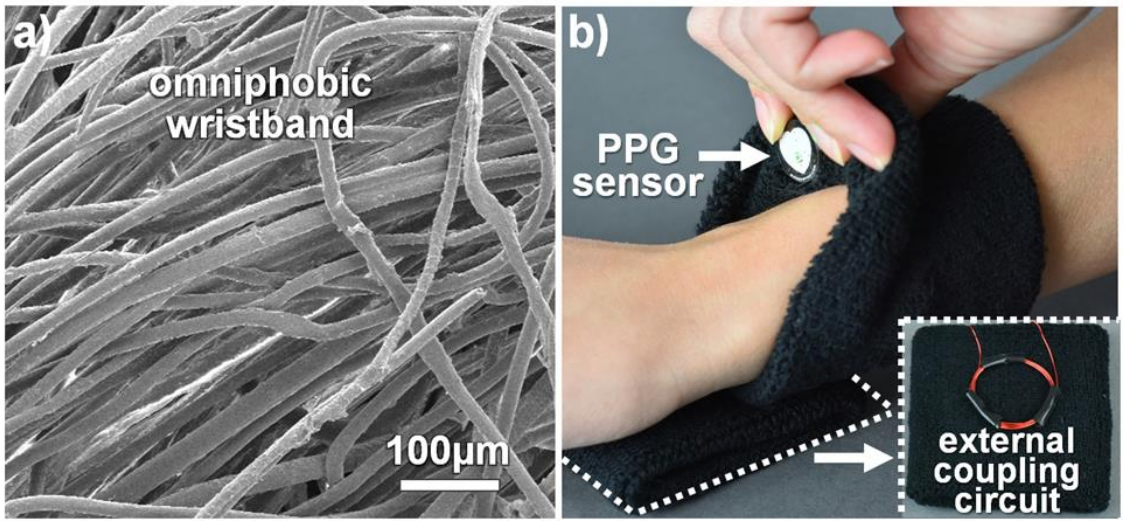

Figure 4.15. OSC-powered PPG wristband. a) High-resolution SEM images of $C_{12}F$-silanized wristband. b) Image of the PPG sensor embedded in the omniphobic wristband. Inset shows the copper coil used for the external coupling circuit.

4.2.7 Fabrication Costs

Using the non-contact voltage detection glove (**Figure 4.21**, **Figure 4.12**) and the PPG wristband (**Figure 4.20**, **Figure 4.15**), we found that the averaged fabrication cost of OSC-based e-textiles could be less than $0.28 per coil (**Table 6**). This calculation does not consider either the cost of the textile or the associated labor or capital expenses. Moreover, the ultimate functionality of OSC-based e-textiles relies on the textile-mounted electronics (SMD electronics, microcontroller with Bluetooth connectivity...).

Table 6. Itemized cost of the materials needed to fabricate OSCs. These prices correspond to small quantities and could be further reduced by volume discounts.

Silk from B. mori cocoons	$ 0.090
MWCNTs	$ 0.055
ChC	$ 0.042
Silane	$ 0.040
Solvents and Reagents	$ 0.049
Total cost	$ 0.276

4.3 Results and Discussion

4.3.1 Design and Fabrication of OSCs

Figure 4.16a shows the fabrication process followed to fabricate the conductive thread used to fabricate the OSCs. First, a 1:10 solution of silk fibroin (SF) comprising three secondary structures—α-helix, β-sheet, and random-coil—was prepared by dissolving SF in a $CaCl_2$-formic acid solution. Chitin carbon (ChC) and multiwall carbon nanotubes (MWCNTs) were mixed (**Figure 4.16**a) and incorporated to this solution in a 1:10 ratio with respect to the SF. The electrospinning of this solution on a rotating mandrel resulted in the alignment of ~14 μm-thick conductive silk microfibers, which were subsequently twisted into a thread (**Figure 4.16**; **Figure 4.6**). The conductive silk thread is then fed into the needle of a sewing machine (see **Figure 4.2**) and used to sew planar coils with a serpentine pattern on the textile (**Figure 4.16**c, **Figure 4.1**). We designed and sewed the OSCs in a serpentine pattern to enhance their stretchability, since the use of serpentine designs in stretchable electronics has been widely reported in the literature [150–153]. After the sewing is completed, the terminals of the OCS are connected to the wearable coupling circuit using conductive adhesive. This magnetic resonant coupling (MRC) circuitry can be used to power other wearable electronics, depending on the desired functionality (see **Figure 4.18**). We mounted the MRC circuitry using surface-mount device (SMD) electronic components that weigh ~0.3g and occupy an area of 18mm^2. Finally, the e-textile is sprayed with a fluoroalkylated organosilane solution, which renders both the textile and the OSC omniphobic (**Figure 4.16**c). Planar OSCs can be fabricated in a variety of shapes and sizes using a conventional sewing machine feed with SF/MWCNT/ChC thread. In this work, we used planar OSCs with 3 turns, diameter of ~4 cm, resistance $R_2 = 1.85\ \Omega$, and inductance $L_2 = 3.9 \times 10^{-7}$ H (at a frequency of 6.78 MHz). In general, for WPT applications, it is desired to have high L and low R to maximize the quality factor $Q = 2\pi fL/R$. Increasing the size and turns of the coil typically increases both L and R and therefore a judicious balance needs to be struck between the two.

The omniphobic behavior of OSC-powered e-textiles allows them to repel liquids with surface tensions as low as 27.05 mN/m, including water, sweat, blood, and most oils at room temperature (**Figure 4.16**d, **Figure 4.3**) [1]. This omniphobic behavior arises from the interaction between liquids and the fluorinated polymeric particles firmly attached to the textile due to the reaction of the fluoroalkylated silane and the surface-bound water [127,128]. The sub-10μm size of

these fluorinated particles covalently attached to the e-textile (**Figure 4.4**) does not interfere with the gas transport through the textile (air permeability ~90.5 mm/s, **Figure 4.16**e; **Figure 4.5**) or limit its flexibility.

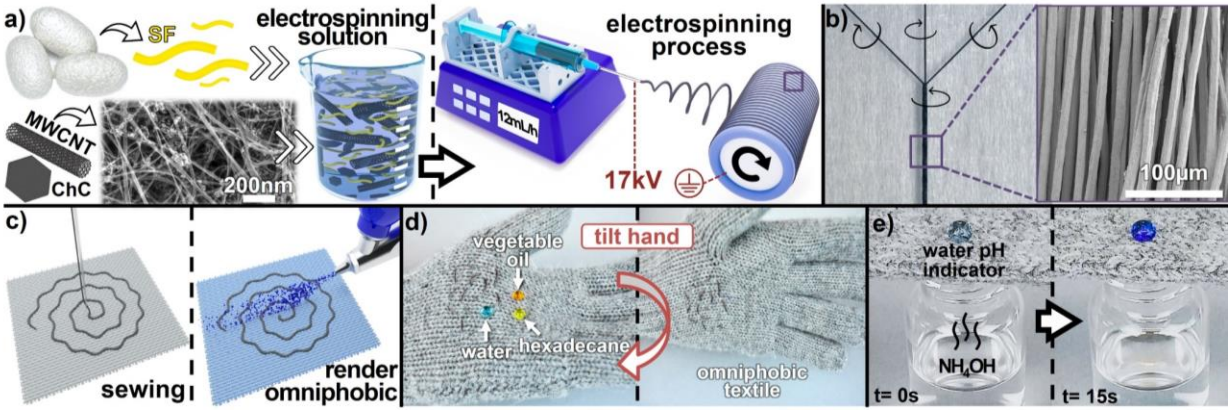

Figure 4.16 Process to fabricate OSC-powered e-textiles. Silk fibroin (SF), chitin carbon (ChC) nanoflakes, and multiwall carbon nanotubes (MWCNTs) are suspended in a 1:10 ratio with respect to the SF and electrospun over a rotating mandrel. b) The resulting SF/MWCNTs/ChC microfibers are separated into yarns and twisted into a conductive thread. The inset shows a high-resolution SEM image of the conductive thread, comprised of aligned SF/MWCNTs/ChC microfibers. c) OSCs can be machine-sewn on most textiles. After, both the textile and the OSC are rendered omniphobic using a rapid spray-based silanization process. d) Omniphobic glove with an OSC sewn on its palmar side holding 100µL droplets of dyed water, hexadecane, and vegetable oil. Once the hand is tilted, the droplets roll over the surface of the glove without leaving traces or staining it, until they fall. e) Omniphobic glove holding a 100µL droplet of pH indicator solution placed on top of an open vial filled with NH_4OH. The high breathability of the functionalized fabric (90.5 mm/s) is evidenced by the reaction between the NH_3 gas and the pH indicator, which changes from light blue (pH=5) to dark blue (pH=10) in 15s.

4.3.2 Materials Characterization of OSCs

The conductive threads used in the fabrication of OSCs can endure strains up to 500% (**Figure 4.17**a). We collected Raman spectra from the electrospun fibers using a Horiba T64000 Raman spectrometer to verify the incorporation of the MWCNTs and ChC in SF. We recorded at least 10 spectra per sample, which were averaged to generate the representative Raman spectra shown in **Figure 4.17**b. We used the automated peak fitting algorithm of OriginPro 2020b (OriginLab Inc.) to deconvolute the Raman measurements. The occurrence of the D-band at 1350 cm^{-1}, G-band at

1580 cm^{-1}, and the G'-band at 2700 cm^{-1} validate the presence of electrically active nanocarbon species (MWCNTs and ChC) embedded in the SF matrix.

We used an optimized composition of the conductive SF/MWCNTs/ChC thread to fabricate the OSCs to minimize resistance without significantly compromising its stretchability and toughness (**Figure 4.17**c, **Figure 4.6**). The resistances of 80-90 Ω/m were achieved by using a thread containing SF (90 wt%) with MWCNT (7 wt%) and ChC (3 wt%). The relative change in resistance of the OSC upon stretching is proportional to the length of the conductive thread, which changes linearly with the applied tensile force (**Figure 4.17**d). The conductivity of the electrospun SF/MWCNTs/ChC nanocomposite is primarily due to the highly networked nanocarbon materials (MWCNT and ChC). As the OSC thread stretches due to the application of a tensile force, the electrically conductive network becomes more "open", increasing the median distance between nanocarbon particles, thus increasing the resistance of the network and consequently the nanocomposite thread [168,169]. The low viscoelastic loss modulus (imaginary component of the complex dynamic modulus used to describe viscoelastic materials [170] of the SF/MWCNTs/ChC fibers ensures minimal phase lag between their strain and stress, facilitating their rapid (~30ms) response and recovery from sudden stretching—a quality highly desired in the textile industry to maximize the compliance of the garment and the comfort of the user (**Figure 4.17**e). To minimize the changes in the WPT efficiency of the OSC caused by the changes in the resistance of the SF/MWCNTs/ChC fibers due to stretching, we created all our OSCs using a serpentine design (**Figure 4.16**c, **Figure 4.17**). Due to the serpentine nature of the design, it first "unfurls" when stretched, without intrinsically stretching the thread fibers. Since the conductivity of the electrospun SF/MWCNTs/ChC nanocomposite is primarily due to the highly networked nanocarbon materials (MWCNT and ChC), the absence of intrinsic stretching prevents the conductive network from stretching, thus preserving the resistance of the OSC thread. We tested the resistance to fatigue of the proposed SF/MWCNTs/ChC threads by exposing them to strains up to 100% during 2500 cycles, without perceiving any significant drop in performance (**Figure 4.17**f).

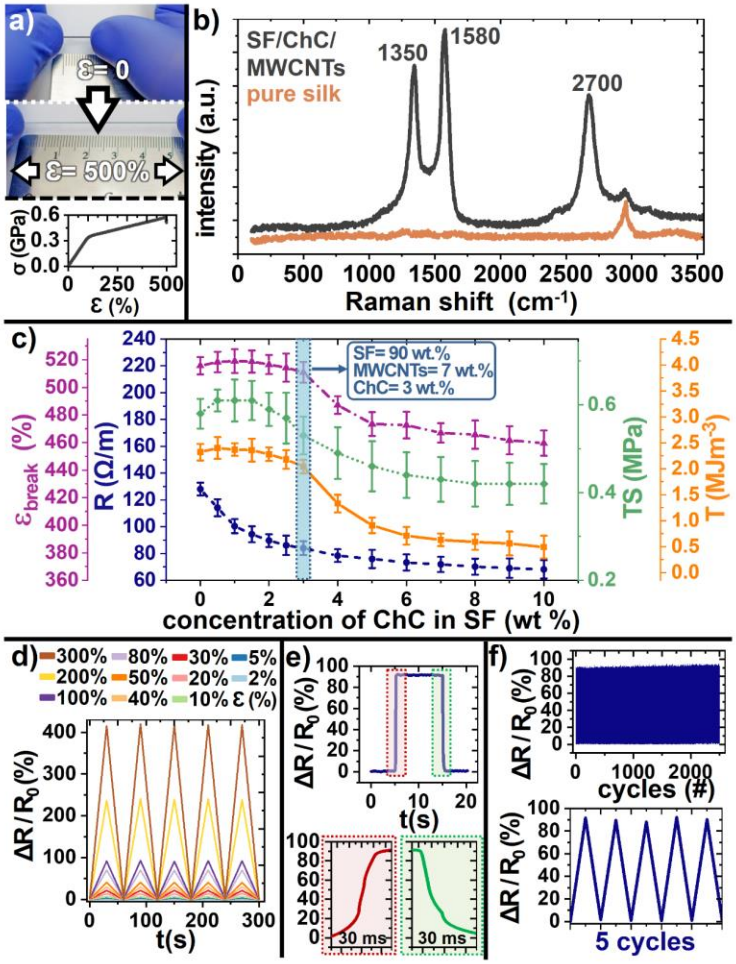

Figure 4.17 Materials characterization of the SF/MWCNTs/ChC thread. Stretchability of the SF/MWCNTs/ChC thread used to sew OSCs. b) Comparison between the Raman spectra of SF/MWCNTs/ChC microfibers and pure silk microfibers. c) Dependence of the maximum strain at break (ε_{break}), resistance (R), tensile strength (*TS*), and toughness (*T*) of the SF/MWCNTs/ChC thread on the concentration of ChC, for a total concentration of carbonaceous nanostructures (MWCNTs and ChC) of 10 wt% in SF. d) Dependence of the relative change in resistance of the SF/MWCNTs/ChC thread on its stretching and relaxation. e) Rapid elastic response (~30ms) of the SF/MWCNTs/ChC thread upon the sudden application of a strain ε= 100%. f) Resistance of the SF/MWCNTs/ChC thread to the application of 2,500 loading and unloading cycles (ε= 100%).

4.3.3 Working Principle of Flexible and Stretchable OSCs

OSCs sewn on the surface of conventional textiles can be used to wirelessly power wearable electronics and e-textiles through a magnetic resonant coupling (MRC) circuit, as shown in **Figure 4.18**a. The inductive coupling between the OSC and an external primary coil enables efficient wireless power transfer (WPT) when the two coils are in resonance [161]. We selected the values of

the capacitors in the MRC circuits of both the primary coil and the OSC so that, for a known load (Z_L) applied to the OSC, the primary coil and the OSC are in resonance at the desired frequency of operation (5.2 MHz). The resonance between the coils greatly increases coupling and power transfer efficiency since MRC resonators exchange energy at a much higher rate than they dissipate due to internal damping [171]. The stretchability of the conductive SF/MWCNTs/ChC thread and the serpentine pattern of OSCs make OSC-powered e-textiles easily bendable (bending radius of curvature = ~2 mm, comparable to the thickness of the substrate textile), twistable (**Figure 4.8**) and omnidirectionally stretchable (for strains up to ε = 100%, see **Figure 4.18**b), and hence do not constraint the motions of the wearer or compromise user's comfort.

The omniphobic character of OSC-powered e-textiles allow them to operate even when fully immerged in water (**Figure 4.18**c), protecting the embedded electronics from short circuits and the eventual corrosion caused by sweating, washing cycles, or accidental spills. Moreover, after more than 100 cleaning cycles consisting of immersion in water followed by drying (wiping the textile with an absorbent paper sheet; **Figure 4.18**d), the apparent static contact angle of water on omniphobic OSC-powered e-textiles remains unaffected, $\theta_{app}^{H_2O}$ = 155°.

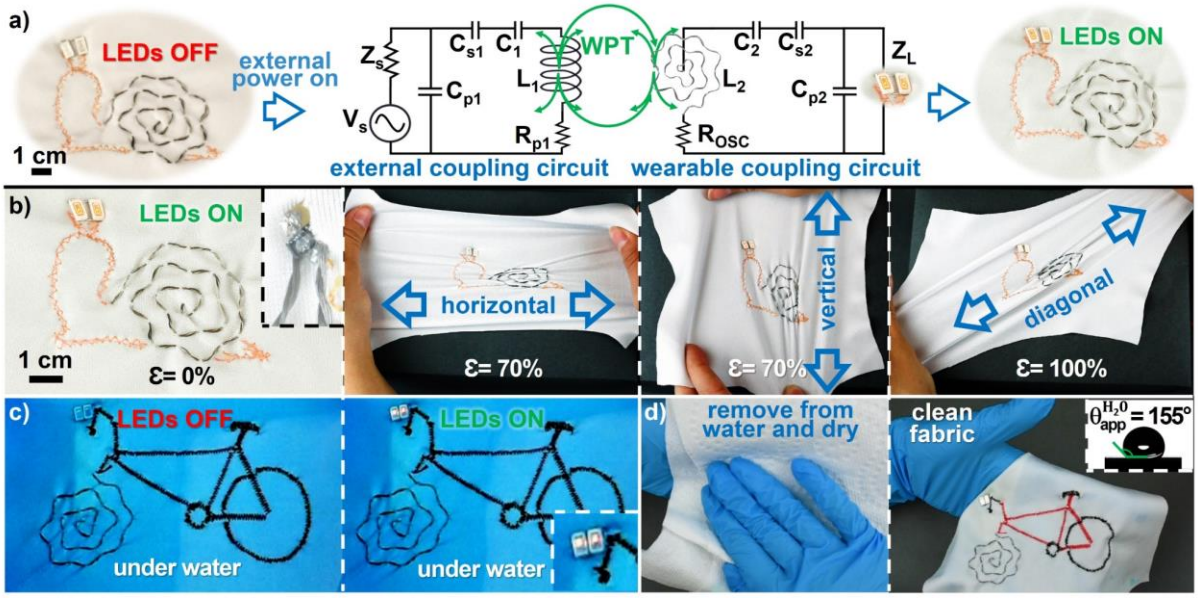

Figure 4.18 Stretchability and water repellency of OSC-powered omniphobic e-textiles. a) Schematic diagram showing the MRC circuitry used to power e-textiles using OSCs. b) Operation of a 4-cm diameter OSC subjected to strains up to 100% in multiple directions (LEDs are on in all pictures) Inset shows a picture of the back of the textile showing the SMD electronic components, which weigh ~0.3g, and occupy an area of ~18 mm^2. c) Wireless operation of OSC-based e-textiles while submerged in water. d) Easy cleaning of OSC-based e-textiles by bringing them into contact with a sheet of absorbent paper.

4.3.4 Electrical Characterization of OSCs

We studied the frequency-dependent WPT characteristics of OSCs in air, under water, and subjected to varying mechanical strains. We measured the scattering parameter S_{11} (reflection coefficient) at the primary coil side, from which, for low interconnect losses, the WPT efficiency ($|S_{21}|^2$) may be approximated as $\eta \approx \left(1-|S_{11}|^2\right)\times 100\%$ (**Figure 4.10**, **Figure 4.11**). Thanks to the omniphobic functionalization, OSCs can operate during prolonged immersion in water (~24 h), without shifting their resonance frequency (**Figure 4.19**a). Furthermore, since we use magnetic resonance (inductive) coupling to wirelessly power the OSCs, their performance is not degraded during underwater operation due to the weak diamagnetism of water (relative permeability μ/μ_0 = 0.999992; where $\mu_0 = 4\pi\times10^{-7}$ H/m). **Figure 4.19**b shows the enhancement of WPT efficiency enabled by the addition of an impedance matching circuit of capacitors (**Figure 4.8**) as determined from bandpass filter theory [43]. When subjected to mechanical strains, the resonant frequency of OSCs undergoes a blue-shift (towards higher frequencies) due to the distortion of the coil shape (**Figure 4.19**c). Nevertheless, the reduction in WPT efficiency is less than 30% even at significant

uniaxial strains (ε =50%), whereas the maximum longitudinal strain that human skin can sustain is ~30% [155]. The highest WPT efficiency (~40%) is observed at small positive uniaxial strains (ε ~10%), rather than in unstrained OSCs (**Figure 4.19**d), since the serpentine sewn pattern of the OSC thread is completely unfurled at such strains. For reference, the maximum shear strain that the human skin can sustain is ~11% [154]. At successively higher uniaxial strains, however, the WPT efficiency drops due to the asymmetric distortion of the OSCs. Nevertheless, the OSC is electromechanically robust enough to operate with at least 65% of the maximum achievable WPT efficiency in a broad region of the strain-frequency landscape (region enclosed by the red dotted line in **Figure 4.18**d) up to ε = ~70% and within a 4.5–8 MHz frequency range, which includes the 6.78 MHz center frequency of the Industrial Scientific and Medical (ISM) band.

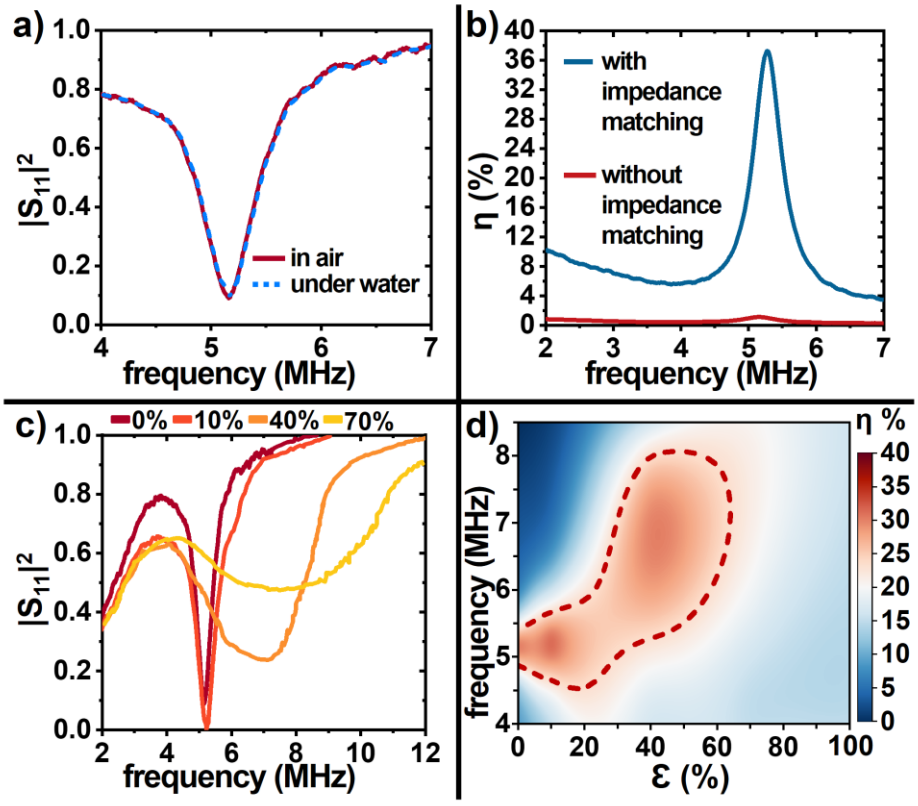

Figure 4.19 Electrical Characterization of the WPT performance of OSC-based e-textiles.
a) Frequency-dependence of the reflectance, $|S_{11}|^2$, of an OSC with a resonant frequency f_0= 5.2 MHz, in air and under water. b) WPT efficiency of OSC before and after their connection to an impedance matching circuit. These measurements are taken at 0% strain, with an input power of 1W at the primary coil. c) Reflectance characteristics, $|S_{11}|^2$, of the OSC under different strains. d) Contour plot showing the dependence of the WPT efficiency (η) of the OSC on the applied strain and operating frequency. The region enclosed by the red dotted line indicates a regime where the WPT efficiency is within 65% of its maximum possible.

4.3.5 Battery-free, Wirelessly-powered, Photoplethysmography Wristband

We developed a stretchable (one size fits all) OSC-powered photoplethysmography (PPG) wristband that can be wirelessly paired with cellphones, tablets, laptops, or desktop computers *via* Bluetooth (**Figure 4.20**). This PPG wristband comprises a miniaturized reverse-mounted green SMD LED, which illuminates the skin of the user, and a photodetector collecting the reflected light. The amount of reflected light is proportional to the volume of blood circulating under the skin of the user. Therefore, by continuously collecting the reflected light, it is possible to identify different cardiac phases and associated parameters noninvasively (**Figure 4.20**a and b; **Figure 4.14**, **Figure 4.15**) [172]. The OSC sewn on the wristband (**Figure 4.20**c) powers, *via* WPT, the low-power microcontroller and Bluetooth chip integrated on this wearable device, which wirelessly transmits the collected PPG signals to the paired device in real time. By mounting the LED on the back of the flexible PCB of this wearable, we avoided its direct contact with the skin of the user, minimizing the experimental noise generated during the motion of the wearer. This setup decreases noise generated by the friction of the LED and the user's skin, allowing the wristband-PPG to work while the wearer is on movement (**Figure 4.20**d). The signals recorded with this wearable device allow us to distinguish the three critical points of each PPG peak: systolic wave (I), dicrotic notch (II), and diastolic peak (III), see inset of **Figure 4.20**d [172]. We also tested the performance of the OSC-powered PPG wristband after the device was subjected to 50 washing cycles and 20 usage cycles (user wearing it for 5 minutes while running at an average speed of ~9km/h), see **Figure 4.20**e. We attribute the stability of the sensing performance of the device to the omniphobic behavior of the e-textile, which protects the electronic components from their potential degradation during the washing cycles and the prolonged exposure to the sweat of the wearer.

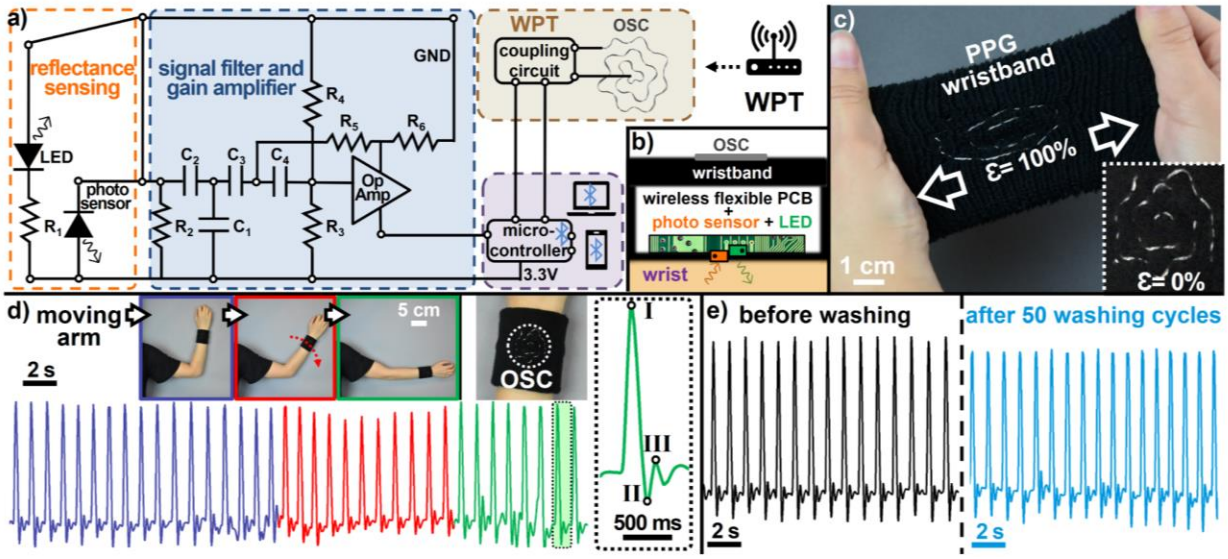

Figure 4.20 OSC-powered PPG wristband. Schematic circuit diagram of the OSC-powered PPG wristband. The PPG flexible sensor is interfaced with a miniaturized microcontroller with Bluetooth for signal processing and wireless data transmission. b) Schematics of the cross-section of the PPG wristband. c) Stretchability of the PPG wristband (ε =100%, OSC facing up). d) PPG signals recorded from a volunteer wearing the PPG wristband while moving their arm. The inset shows the characteristic PPG features of one cardiac cycle: systolic peak (I), dicrotic notch (II), and diastolic peak (III). e) Signals obtained by the PPG wristband before and after enduring 50 washing cycles and 20 usage cycles (while exercising).

4.3.6 Wearable Non-contact Voltage Detection Glove

The omniphobicity of OSC-powered smart clothing lends itself to potential applications where traditional hygroscopic e-textiles, which absorb water when immersed in it, would be rendered inoperative (**Figure 4.12**). As an example, we developed a wirelessly powered glove capable of alerting the wearer about the proximity of live voltage even under water (**Figure 4.21**; **Figure 4.13**). This e-textile comprises a miniaturized non-contact voltage detection circuit [173] mounted on a glove that is wirelessly powered through an OSC *via* WPT (**Figure 4.21**a). A conductive ~1cm^2 pad was embroidered at the index fingertip of the glove using SF/MWCNTs/ChC thread. This conductive pad polarizes when it gets in the proximity to any cables connected to a voltage source, injecting a small current in the non-contact voltage detection circuit. This current is amplified using the power wirelessly received from the OSC sewed at the palm side of the hand (bottom of the glove) and used to power an SMD LED mounted at the index fingertip (**Figure 4.21**b and c). The frequency of operation of this OSC-based smart glove at wireless resonance is 5.2MHz, which

is within the high transmission band of water, enabling the use of this e-textile under water without significant degradation in its non-contact voltage detection performance (**Figure 4.21**d).

Due to the miniaturized low-voltage components used on their fabrication, OSC-powered e-textiles safely operate under electromagnetic wireless power densities ranging 4.77 to 12.33 mW/cm^2 (see 4.2.4). According to IEEE safety standards for the protection of humans against the potential adverse health effects from exposure to non-ionizing electromagnetic fields ranging 1–30MHz [54], the maximum power density allowed for WPT applications is 33.2 mW/cm^2. This maximum allowed power density is at least 94% larger than the power densities needed for OSC-powered wearables to operate, demonstrating the safety and reliability of these silk-based wirelessly powered e-textiles (**Table 5**).

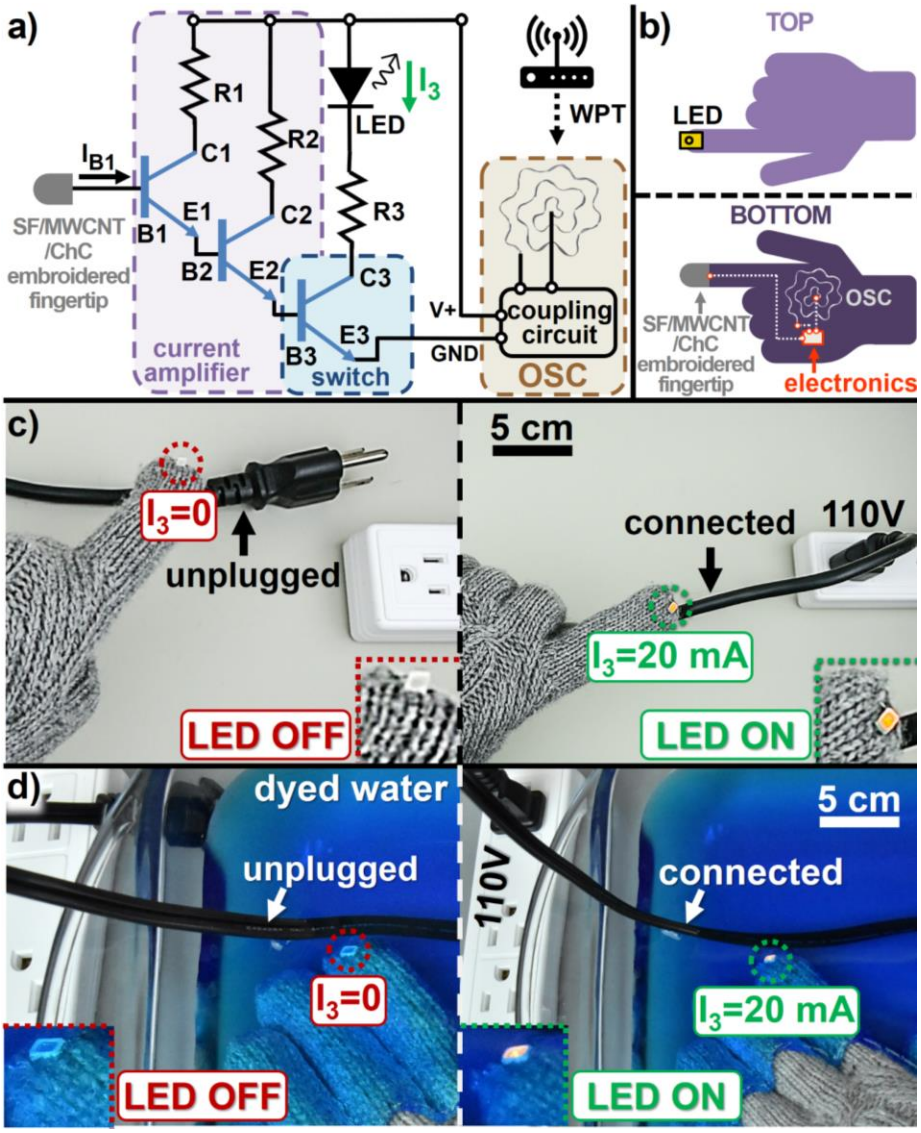

Figure 4.21 OSC-powered wearable non-contact voltage detector. a) Schematic diagram of a non-contact voltage detection circuit mounted at the fingertip of a glove and wirelessly powered *via* OSC. b) Bottom and top views of the omniphobic glove showing the OSC sewed on the palm side (bottom) and the miniaturized non-contact voltage detection circuit attached to the index fingertip (top). c) Non-contact identification of cables connected to voltage using an OSC-powered omniphobic glove. d) Under water non-contact identification of cables connected to voltage using an omniphobic glove wirelessly powered through an OSC.

4.4 Conclusions

In summary, this work demonstrates a simple and industrially-scalable [174,175] method to fabricate omniphobic silk-based coils (OSCs) which are easily integrated into conventional textiles by sewing and can be used for the continuous wireless powering of wearable electronic devices *via* magnetic resonance coupling. OSCs are highly conductive, lightweight, flexible, and stretchable (ε_{break} ~500%), and can be produced at large scale in a cost-effective manner. The omniphobic silanization of e-textiles powered by OSCs protects both the conductive nanomaterials in the coils and the flexible circuitry embedded in the textile from humidity-induced short-circuits and degradation upon prolonged contact with the wearer's sweat. Moreover, the omniphobicity of OSC-powered e-textiles renders them stain repellent to aqueous solutions and organic liquids with surface tensions as low as 27.05 mN/m, without significantly reducing their breathability (air permeability >90 mm/s). This omniphobicity makes OSC-powered e-textiles exhibit excellent stability in high moisture environments and under mechanical deformations, which confer them with a remarkable washing durability (no degradation in performance even after 50 washing cycles, AATCC-135 standard machine-washing test). We demonstrated that OSCs can be used as low-cost and easy to implement power sources for wearable devices and smart clothing through the fabrication of a textile wristband-like photoplethysmography battery-free device and a wireless non-contact voltage detection glove. We expect that the design and fabrication strategies proposed here will accelerate the development and commercialization of fully washable and battery-free smart clothing and reusable wearable devices, allowing current technologies to benefit from recent advances in wireless power transfer.

5. CONCLUSIONS

In summary, this PhD dissertation demonstrates versatile, cost-effective, and scalable methods to for the design and fabrication of moisture-insensitive, self-powered paper-based devices and e-textiles. The cellulose paper, e-textiles, and threads introduced in Chapters 2, 3, and 4 benefit from the covalent modifications of their fibrous structure, by spray-deposition of fluoroalkylated organosilanes, which confers these devices a remarkable water, oil, and dust repellency. This omniphobicity preserves the mechanical properties of the fibers upon contact with aqueous solutions and organic liquids with surface tensions as low as 27.05 mN/m and prevents the corrosion of the printed electrodes and electronic components mounted on their surface. Additionally, the embroidery approach used to assemble R^F-TENGs protects both the electronics embedded in the textile and the textile from bacterial proliferation, moisture, and over-stretching ($\varepsilon_{max} = 55\%$), conferring these R^F-e-textiles with excellent stability under mechanical deformations and remarkable washing durability after 50 standard machine-washing cycles.

In Chapter 2, I demonstrate the use of moisture-insensitive and self-powered paper-based electronics devices (R^F-SPEs) as flexible and wireless human-machine interfaces. R^F-SPEs are simple to design and rapid to print, at a low cost (<$0.25 per device), by simply exposing cellulose-based paper to the sequential spray-deposition of fluoroalkylated organosilanes, PTFE, EC, and conductive NiNPs. The resulting R^F-SPEs are lightweight, flexible, and even foldable. R^F-SPEs harvest electrostatic energy from the user during user interaction, generating power densities up to 300 $\mu W/cm^2$, which enables their use as wireless and battery-free human-machine interfaces. I envision that the simplicity, low material cost, and compatibility with large-scale manufacturing processes of the proposed fabrication method to create R^F-SPEs will pave the way towards the cost-effective fabrication of self-powered paper-based electronics and the ubiquitous integration of human-machine interfaces.

Across Chapter 3, I developed a simple and scalable method to transform conventional garments or textiles into omniphobic and self-powered e-textiles capable of powering embedded electronic systems using the electrostatic energy generated by the natural motions of the wearer. These e-textiles harvest biomechanical energy using omniphobic, fabric-based, triboelectric nanogenerators (R^F-TENGs) fabricated, at a low cost (<0.04$/$cm^2$), by combining textile-mounted

electronics with embroidery and the spray-based deposition of silanizing agents, highly networked AgNFs, and a conformable PTFE encapsulating solution. The resulting R^F-TENGs are lightweight, flexible, breathable (air permeability 90.5 mm/s), and can generate high output power densities (~600 $\mu W/cm^2$). Finally, the combination in the same textile of several R^F-TENGs, some serving as biomechanical energy transducers and some as tactile sensors, enables the creation of battery-free e-textiles controlled by the wearer. I envision that the versatility of the proposed fabrication method to create omniphobic e-textiles and its compatibility with large-scale production processes, such as spray deposition, will pave the way toward the cost-effective manufacturing of robust e-textiles and wearable human-machine interfaces for emerging applications.

Finally, in Chapter 4, I used a conductive silk-based thread to demonstrate a simple and industrially-scalable method to fabricate omniphobic silk-based coils (OSCs) which are easily integrated into conventional textiles by sewing and can be used for the continuous wireless powering of wearable electronic devices *via* magnetic resonance coupling. OSCs are highly conductive, lightweight, flexible, and stretchable (ε_{break} ~500%), and can be produced at large scale in a cost-effective manner. I demonstrated that OSCs can be used as low-cost and easy to implement power sources for wearable devices and smart clothing through the fabrication of a textile wristband-like photoplethysmography battery-free device and a wireless non-contact voltage detection glove.

The technologies developed during this PhD will contribute to the development of new wearable devices and human-machine interfaces. As an example, the self-powered paper-based touch-pads presented in Chapter 2 could give readers the opportunity to send information from printed books, pamphlet, and catalogues to their phones *via* Bluetooth. Similarly, the self-powered e-textiles described in Chapter 3, when complemented with efficient machine learning methods, would be able to predict the fatigue of the user, alert about incorrect ergonomics at work, and provide the wearers with a full-body interface to communicate with machines via gesture and posture recognition. Additionally, the wireless OSC-based interfaces developed in Chapter 4 could help to significantly reduce the wiring connecting patients at the hospital with their monitoring equipment. Future studies on the usability of these wearable devices and human-machine interfaces would lead to design improvements that would enhance the practicality, safety, and

comfort of these devices, expanding the adoption of this technology. Finally, I expect that the design and fabrication strategies proposed here will accelerate the development and commercialization of low-cost paper-based electronics and fully washable and battery-free smart clothing and reusable wearable devices, allowing current technologies to benefit from recent advances in self-power and wireless power transfer technologies.

REFERENCES

(1) Sala de Medeiros, M.; Chanci, D.; Moreno, C.; Goswami, D.; Martinez, R. V. Waterproof, Breathable, and Antibacterial Self-Powered E-Textiles Based on Omniphobic Triboelectric Nanogenerators. *Adv. Funct. Mater.* **2019**, *1904350*, 1904350. https://doi.org/10.1002/adfm.201904350.

(2) Guo, Y.; Zhang, X.-S.; Wang, Y.; Gong, W.; Zhang, Q.; Wang, H.; Brugger, J. All-Fiber Hybrid Piezoelectric-Enhanced Triboelectric Nanogenerator for Wearable Gesture Monitoring. *Nano Energy* **2018**, *48* (January), 152–160. https://doi.org/10.1016/j.nanoen.2018.03.033.

(3) Lai, Y.-C.; Hsiao, Y.-C.; Wu, H.-M.; Wang, Z. L. Waterproof Fabric-Based Multifunctional Triboelectric Nanogenerator for Universally Harvesting Energy from Raindrops, Wind, and Human Motions and as Self-Powered Sensors. *Adv. Sci.* **2019**, *6* (5), 1801883. https://doi.org/10.1002/advs.201801883.

(4) Zhou, Z.; Padgett, S.; Cai, Z.; Conta, G.; Wu, Y.; He, Q.; Zhang, S.; Sun, C.; Liu, J.; Fan, E.; et al. Single-Layered Ultra-Soft Washable Smart Textiles for All-around Ballistocardiograph, Respiration, and Posture Monitoring during Sleep. *Biosens. Bioelectron.* **2020**, *155*, 112064. https://doi.org/10.1016/j.bios.2020.112064.

(5) Wen, Z.; Yeh, M.-H.; Guo, H.; Wang, J.; Zi, Y.; Xu, W.; Deng, J.; Zhu, L.; Wang, X.; Hu, C.; et al. Self-Powered Textile for Wearable Electronics by Hybridizing Fiber-Shaped Nanogenerators, Solar Cells, and Supercapacitors. *Sci. Adv.* **2016**, *2* (10), e1600097. https://doi.org/10.1126/sciadv.1600097.

(6) Wang, Z.; Pan, R.; Sun, R.; Edström, K.; Strømme, M.; Nyholm, L. Nanocellulose Structured Paper-Based Lithium Metal Batteries. *ACS Appl. Energy Mater.* **2018**, *1* (8), 4341–4350. https://doi.org/10.1021/acsaem.8b00961.

(7) Fraiwan, A.; Choi, S. A Stackable, Two-Chambered, Paper-Based Microbial Fuel Cell. *Biosens. Bioelectron.* **2016**, *83*, 27–32. https://doi.org/10.1016/j.bios.2016.04.025.

(8) Mo, F.; Liang, G.; Huang, Z.; Li, H.; Wang, D.; Zhi, C. An Overview of Fiber-Shaped Batteries with a Focus on Multifunctionality, Scalability, and Technical Difficulties. *Adv. Mater.* **2020**, *32* (5), 1902151. https://doi.org/10.1002/adma.201902151.

(9) Gwon, H.; Hong, J.; Kim, H.; Seo, D.-H.; Jeon, S.; Kang, K. Recent Progress on Flexible Lithium Rechargeable Batteries. *Energy Environ. Sci.* **2014**, *7* (2), 538–551. https://doi.org/10.1039/C3EE42927J.

(10) Christodouleas, D. C.; Simeone, F. C.; Tayi, A.; Targ, S.; Weaver, J. C.; Jayaram, K.; Fernández-Abedul, M. T.; Whitesides, G. M. Fabrication of Paper-Templated Structures of Noble Metals. *Adv. Mater. Technol.* **2017**, *2* (2), 1600229. https://doi.org/10.1002/admt.201600229.

(11) Sani, N.; Robertsson, M.; Cooper, P.; Wang, X.; Svensson, M.; Andersson Ersman, P.; Norberg, P.; Nilsson, M.; Nilsson, D.; Liu, X.; et al. All-Printed Diode Operating at 1.6 GHz. *Proc. Natl. Acad. Sci.* **2014**, *111* (33), 11943–11948. https://doi.org/10.1073/pnas.1401676111.

(12) Chen, J.; Zhu, G.; Yang, J.; Jing, Q.; Bai, P.; Yang, W.; Qi, X.; Su, Y.; Wang, Z. L. Personalized Keystroke Dynamics for Self-Powered Human–Machine Interfacing. *ACS Nano* **2015**, *9* (1), 105–116. https://doi.org/10.1021/nn506832w.

(13) Hamedi, M. M.; Campbell, V. E.; Rothemund, P.; Güder, F.; Christodouleas, D. C.; Bloch, J.-F.; Whitesides, G. M. Electrically Activated Paper Actuators. *Adv. Funct. Mater.* **2016**, *26* (15), 2446–2453. https://doi.org/10.1002/adfm.201505123.

(14) Thuo, M. M.; Martinez, R. V.; Lan, W.-J.; Liu, X.; Barber, J.; Atkinson, M. B. J.; Bandarage, D.; Bloch, J.-F.; Whitesides, G. M. Fabrication of Low-Cost Paper-Based Microfluidic Devices by Embossing or Cut-and-Stack Methods. *Chem. Mater.* **2014**, *26* (14), 4230–4237. https://doi.org/10.1021/cm501596s.

(15) Hamedi, M. M.; Ainla, A.; Güder, F.; Christodouleas, D. C.; Fernández-Abedul, M. T.; Whitesides, G. M. Integrating Electronics and Microfluidics on Paper. *Adv. Mater.* **2016**, *28* (25), 5054–5063. https://doi.org/10.1002/adma.201505823.

(16) Phillips, E. A.; Moehling, T. J.; Ejendal, K. F. K.; Hoilett, O. S.; Byers, K. M.; Basing, L. A.; Jankowski, L. A.; Bennett, J. B.; Lin, L.-K.; Stanciu, L. A.; et al. Microfluidic Rapid and Autonomous Analytical Device (MicroRAAD) to Detect HIV from Whole Blood Samples. *bioRxiv* **2019**, 582999. https://doi.org/10.1101/582999.

(17) Zhong, Q.; Zhong, J.; Hu, B.; Hu, Q.; Zhou, J.; Wang, Z. L. A Paper-Based Nanogenerator as a Power Source and Active Sensor. *Energy Environ. Sci.* **2013**, *6* (6), 1779. https://doi.org/10.1039/c3ee40592c.

(18) Pal, A.; Cuellar, H. E.; Kuang, R.; Caurin, H. F. N.; Goswami, D.; Martinez, R. V. Self-Powered, Paper-Based Electrochemical Devices for Sensitive Point-of-Care Testing. *Adv. Mater. Technol.* **2017**, *2* (10), 1700130. https://doi.org/10.1002/admt.201700130.

(19) Sadri, B.; Goswami, D.; Sala de Medeiros, M.; Pal, A.; Castro, B.; Kuang, S.; Martinez, R. V. Wearable and Implantable Epidermal Paper-Based Electronics. *ACS Appl. Mater. Interfaces* **2018**, *10* (37), 31061–31068. https://doi.org/10.1021/acsami.8b11020.

(20) Liao, X.; Zhang, Z.; Liao, Q.; Liang, Q.; Ou, Y.; Xu, M.; Li, M.; Zhang, G.; Zhang, Y. Flexible and Printable Paper-Based Strain Sensors for Wearable and Large-Area Green Electronics. *Nanoscale* **2016**, *8* (26), 13025–13032. https://doi.org/10.1039/C6NR02172G.

(21) Lou, Z.; Chen, S.; Wang, L.; Shi, R.; Li, L.; Jiang, K.; Chen, D.; Shen, G. Ultrasensitive and Ultraflexible E-Skins with Dual Functionalities for Wearable Electronics. *Nano Energy* **2017**, *38*, 28–35. https://doi.org/10.1016/j.nanoen.2017.05.024.

(22) Brunetti, F.; Operamolla, A.; Castro-Hermosa, S.; Lucarelli, G.; Manca, V.; Farinola, G. M.; Brown, T. M. Printed Solar Cells and Energy Storage Devices on Paper Substrates. *Adv. Funct. Mater.* **2019**, *29* (21), 1806798. https://doi.org/10.1002/adfm.201806798.

(23) Li, H.; Li, X.; Wang, W.; Huang, J.; Li, J.; Lu, Y.; Chang, J.; Fang, J.; Song, W. Highly Foldable and Efficient Paper-Based Perovskite Solar Cells. *Sol. RRL* **2019**, *3* (3), 1800317. https://doi.org/10.1002/solr.201800317.

(24) Zhang, Y.; Zhang, L.; Cui, K.; Ge, S.; Cheng, X.; Yan, M.; Yu, J.; Liu, H. Flexible Electronics Based on Micro/Nanostructured Paper. *Adv. Mater.* **2018**, *30* (51), 1801588. https://doi.org/10.1002/adma.201801588.

(25) Briedis, U.; Valisevskis, A.; Grecka, M. Development of a Smart Garment Prototype with Enuresis Alarm Using an Embroidery-Machine-Based Technique for the Integration of Electronic Components. *Procedia Comput. Sci.* **2017**, *104* (December 2016), 369–374. https://doi.org/10.1016/j.procs.2017.01.147.

(26) Chen, G.; Li, Y.; Bick, M.; Chen, J. Smart Textiles for Electricity Generation. *Chem. Rev.* **2020**, *120* (8), 3668–3720. https://doi.org/10.1021/acs.chemrev.9b00821.

(27) Weng, W.; Chen, P.; He, S.; Sun, X.; Peng, H. Smart Electronic Textiles. *Angew. Chemie Int. Ed.* **2016**, *55* (21), 6140–6169. https://doi.org/10.1002/anie.201507333.

(28) Xiong, J.; Cui, P.; Chen, X.; Wang, J.; Parida, K.; Lin, M. F.; Lee, P. S. Skin-Touch-Actuated Textile-Based Triboelectric Nanogenerator with Black Phosphorus for Durable Biomechanical Energy Harvesting. *Nat. Commun.* **2018**, *9* (1), 1–9. https://doi.org/10.1038/s41467-018-06759-0.

(29) Rao, J.; Liu, N.; Li, L.; Su, J.; Long, F.; Zou, Z.; Gao, Y. A High Performance Wire-Shaped Flexible Lithium-Ion Battery Based on Silicon Nanoparticles within Polypyrrole/Twisted Carbon Fibers. *RSC Adv.* **2017**, *7* (43), 26601–26607. https://doi.org/10.1039/c7ra02051a.

(30) Wan, F.; Zhang, L.; Wang, X.; Bi, S.; Niu, Z.; Chen, J. An Aqueous Rechargeable Zinc-Organic Battery with Hybrid Mechanism. *Adv. Funct. Mater.* **2018**, *28* (45), 1804975. https://doi.org/10.1002/adfm.201804975.

(31) Kwak, S. S.; Yoon, H.-J.; Kim, S.-W. Textile-Based Triboelectric Nanogenerators for Self-Powered Wearable Electronics. *Adv. Funct. Mater.* **2019**, *29* (2), 1804533. https://doi.org/10.1002/adfm.201804533.

(32) Liu, Z.; Li, H.; Shi, B.; Fan, Y.; Wang, Z. L.; Li, Z. Wearable and Implantable Triboelectric Nanogenerators. *Adv. Funct. Mater.* **2019**, *29* (20), 1808820. https://doi.org/10.1002/adfm.201808820.

(33) Kim, B. J.; Kim, D. H.; Lee, Y.-Y.; Shin, H.-W.; Han, G. S.; Hong, J. S.; Mahmood, K.; Ahn, T. K.; Joo, Y.-C.; Hong, K. S.; et al. Highly Efficient and Bending Durable Perovskite Solar Cells: Toward a Wearable Power Source. *Energy Environ. Sci.* **2015**, *8* (3), 916–921. https://doi.org/10.1039/C4EE02441A.

(34) Chen, J.; Huang, Y.; Zhang, N.; Zou, H.; Liu, R.; Tao, C.; Fan, X.; Wang, Z. L. Micro-Cable Structured Textile for Simultaneously Harvesting Solar and Mechanical Energy. *Nat. Energy* **2016**, *1* (10), 16138. https://doi.org/10.1038/nenergy.2016.138.

(35) Yu, X.; Pan, J.; Zhang, J.; Sun, H.; He, S.; Qiu, L.; Lou, H.; Sun, X.; Peng, H. A Coaxial Triboelectric Nanogenerator Fiber for Energy Harvesting and Sensing under Deformation. *J. Mater. Chem. A* **2017**, *5* (13), 6032–6037. https://doi.org/10.1039/C7TA00248C.

(36) Bai, P.; Zhu, G.; Lin, Z.-H.; Jing, Q.; Chen, J.; Zhang, G.; Ma, J.; Wang, Z. L. Integrated Multilayered Triboelectric Nanogenerator for Harvesting Biomechanical Energy from Human Motions. *ACS Nano* **2013**, *7* (4), 3713–3719. https://doi.org/10.1021/nn4007708.

(37) Pu, X.; Liu, M.; Chen, X.; Sun, J.; Du, C.; Zhang, Y.; Zhai, J.; Hu, W.; Wang, Z. L. Ultrastretchable, Transparent Triboelectric Nanogenerator as Electronic Skin for Biomechanical Energy Harvesting and Tactile Sensing. *Sci. Adv.* **2017**, *3* (5), e1700015. https://doi.org/10.1126/sciadv.1700015.

(38) Ha, M.; Park, J.; Lee, Y.; Ko, H. Triboelectric Generators and Sensors for Self-Powered Wearable Electronics. *ACS Nano* **2015**, *9* (4), 3421–3427. https://doi.org/10.1021/acsnano.5b01478.

(39) Zhang, N.; Chen, J.; Huang, Y.; Guo, W.; Yang, J.; Du, J.; Fan, X.; Tao, C. A Wearable All-Solid Photovoltaic Textile. *Adv. Mater.* **2016**, *28* (2), 263–269. https://doi.org/10.1002/adma.201504137.

(40) Gong, S.; Cheng, W. Toward Soft Skin-Like Wearable and Implantable Energy Devices. *Adv. Energy Mater.* **2017**, *7* (23), 1700648. https://doi.org/10.1002/aenm.201700648.

(41) Sun, G.; Wang, X.; Chen, P. Microfiber Devices Based on Carbon Materials. *Mater. Today* **2015**, *18* (4), 215–226. https://doi.org/10.1016/j.mattod.2014.12.001.

(42) Li, Y.; Meng, L.; Yang, Y.; Xu, G.; Hong, Z.; Chen, Q.; You, J.; Li, G.; Yang, Y.; Li, Y. High-Efficiency Robust Perovskite Solar Cells on Ultrathin Flexible Substrates. *Nat. Commun.* **2016**, *7* (1), 10214. https://doi.org/10.1038/ncomms10214.

(43) Lu, Z.; Zhang, H.; Mao, C.; Li, C. M. Silk Fabric-Based Wearable Thermoelectric Generator for Energy Harvesting from the Human Body. *Appl. Energy* **2016**, *164*, 57–63. https://doi.org/10.1016/j.apenergy.2015.11.038.

(44) Suarez, F.; Nozariasbmarz, A.; Vashaee, D.; Öztürk, M. C. Designing Thermoelectric Generators for Self-Powered Wearable Electronics. *Energy Environ. Sci.* **2016**, *9* (6), 2099–2113. https://doi.org/10.1039/C6EE00456C.

(45) Siddique, A. R. M.; Mahmud, S.; Heyst, B. Van. A Review of the State of the Science on Wearable Thermoelectric Power Generators (TEGs) and Their Existing Challenges. *Renew. Sustain. Energy Rev.* **2017**, *73* (December 2016), 730–744. https://doi.org/10.1016/j.rser.2017.01.177.

(46) Bowen, C. R.; Xie, M.; Zhang, Y.; Topolov, V. Y. Pyroelectric Energy Harvesting : Materials and Applications. In *Ferroelectric Materials for Energy Applications*; Huang, H., Scott, J. F., Eds.; Wiley-VCH, 2018; pp 203–229.

(47) Costa, P.; Nunes-Pereira, J.; Pereira, N.; Castro, N.; Gonçalves, S.; Lanceros-Mendez, S. Recent Progress on Piezoelectric, Pyroelectric, and Magnetoelectric Polymer-Based Energy-Harvesting Devices. *Energy Technol.* **2019**, 1800852. https://doi.org/10.1002/ente.201800852.

(48) He, H.; Wu, Y.; Liu, W.; Rong, M.; Fang, Z.; Tang, X. Comprehensive Modeling for Geometric Optimization of a Thermoelectric Generator Module. *Energy Convers. Manag.* **2019**, *183* (December 2018), 645–659. https://doi.org/10.1016/j.enconman.2018.12.087.

(49) Choi, A. Y.; Lee, C. J.; Park, J.; Kim, D.; Kim, Y. T. Corrugated Textile Based Triboelectric Generator for Wearable Energy Harvesting. *Sci. Rep.* **2017**, *7* (1), 45583. https://doi.org/10.1038/srep45583.

(50) Coyle, S.; Wu, Y.; Lau, K.; De Rossi, D.; Wallace, G.; Diamond, D. Smart Nanotextiles: A Review of Materials and Applications. *MRS Bull.* **2007**, *32* (5), 434–442. https://doi.org/10.1557/mrs2007.67.

(51) Xia, K.; Zhu, Z.; Zhang, H.; Du, C.; Xu, Z.; Wang, R. Painting a High-Output Triboelectric Nanogenerator on Paper for Harvesting Energy from Human Body Motion. *Nano Energy* **2018**, *50* (April), 571–580. https://doi.org/10.1016/j.nanoen.2018.06.019.

(52) Lee, M.; Chen, C.; Wang, S.; Cha, S. N.; Park, Y. J.; Kim, J. M.; Chou, L.; Wang, Z. L. A Hybrid Piezoelectric Structure for Wearable Nanogenerators. *Adv. Mater.* **2012**, *24* (13), 1759–1764. https://doi.org/10.1002/adma.201200150.

(53) Choi, Y.-M.; Lee, M. G.; Jeon, Y. Wearable Biomechanical Energy Harvesting Technologies. *Energies* **2017**, *10* (10), 1483. https://doi.org/10.3390/en10101483.

(54) Alluri, N. R.; Selvarajan, S.; Chandrasekhar, A.; Saravanakumar, B.; Jeong, J. H.; Kim, S. Piezoelectric BaTiO 3 /Alginate Spherical Composite Beads for Energy Harvesting and Self-Powered Wearable Flexion Sensor. *Compos. Sci. Technol.* **2017**, *142*, 65–78. https://doi.org/10.1016/j.compscitech.2017.02.001.

(55) Zhang, H.; Zhang, X.-S.; Cheng, X.; Liu, Y.; Han, M.; Xue, X.; Wang, S.; Yang, F.; A S, S.; Zhang, H.; et al. A Flexible and Implantable Piezoelectric Generator Harvesting Energy from the Pulsation of Ascending Aorta: In Vitro and in Vivo Studies. *Nano Energy* **2015**, *12*, 296–304. https://doi.org/10.1016/j.nanoen.2014.12.038.

(56) Shi, Q.; Wang, T.; Lee, C. MEMS Based Broadband Piezoelectric Ultrasonic Energy Harvester (PUEH) for Enabling Self-Powered Implantable Biomedical Devices. *Sci. Rep.* **2016**, *6* (1), 24946. https://doi.org/10.1038/srep24946.

(57) Khan, Y.; Ostfeld, A. E.; Lochner, C. M.; Pierre, A.; Arias, A. C. Monitoring of Vital Signs with Flexible and Wearable Medical Devices. *Adv. Mater.* **2016**, *28* (22), 4373–4395. https://doi.org/10.1002/adma.201504366.

(58) Yi, F.; Zhang, Z.; Kang, Z.; Liao, Q.; Zhang, Y. Recent Advances in Triboelectric Nanogenerator-Based Health Monitoring. *Adv. Funct. Mater.* **2019**, *1808849*, 1808849. https://doi.org/10.1002/adfm.201808849.

(59) Park, D. Y.; Joe, D. J.; Kim, D. H.; Park, H.; Han, J. H.; Jeong, C. K.; Park, H.; Park, J. G.; Joung, B.; Lee, K. J. Self-Powered Real-Time Arterial Pulse Monitoring Using Ultrathin Epidermal Piezoelectric Sensors. *Adv. Mater.* **2017**, *29* (37), 1702308. https://doi.org/10.1002/adma.201702308.

(60) Rajaram, K.; Kim, J. Flexible Wireless Power Transfer Module Implemented with Aerojet-Printing and Laser-Sintering of Rigid NiZn–Ferrite Ceramic Films. *Nano Energy* **2019**, *57*, 317–326. https://doi.org/10.1016/j.nanoen.2018.12.021.

(61) Lee, H. E.; Lee, D.; Lee, T. I.; Shin, J. H.; Choi, G. M.; Kim, C.; Lee, S. H.; Lee, J. H.; Kim, Y. H.; Kang, S. M.; et al. Wireless Powered Wearable Micro Light-Emitting Diodes. *Nano Energy* **2019**, *55*, 454–462. https://doi.org/10.1016/j.nanoen.2018.11.017.

(62) Bibi, F.; Guillaume, C.; Gontard, N.; Sorli, B. A Review: RFID Technology Having Sensing Aptitudes for Food Industry and Their Contribution to Tracking and Monitoring of Food Products. *Trends Food Sci. Technol.* **2017**, *62*, 91–103. https://doi.org/10.1016/j.tifs.2017.01.013.

(63) Shuaib, D.; Ukkonen, L.; Virkki, J.; Merilampi, S. The Possibilities of Embroidered Passive UHF RFID Textile Tags as Wearable Moisture Sensors. In *2017 IEEE 5th International Conference on Serious Games and Applications for Health (SeGAH)*; IEEE, 2017; pp 1–5. https://doi.org/10.1109/SeGAH.2017.7939286.

(64) Moraru, A.; Helerea, E.; Ursachi, C.; Calin, M. D. RFID System with Passive RFID Tags for Textiles. In *2017 10th International Symposium on Advanced Topics in Electrical Engineering (ATEE)*; IEEE, 2017; pp 410–415. https://doi.org/10.1109/ATEE.2017.7905132.

(65) Han, S.; Kim, J.; Won, S. M.; Ma, Y.; Kang, D.; Xie, Z.; Lee, K.-T.; Chung, H. U.; Banks, A.; Min, S.; et al. Battery-Free, Wireless Sensors for Full-Body Pressure and Temperature Mapping. *Sci. Transl. Med.* **2018**, *10* (435), eaan4950. https://doi.org/10.1126/scitranslmed.aan4950.

(66) Zhu, G.; Peng, B.; Chen, J.; Jing, Q.; Lin Wang, Z. Triboelectric Nanogenerators as a New Energy Technology: From Fundamentals, Devices, to Applications. *Nano Energy* **2015**, *14*, 126–138. https://doi.org/10.1016/j.nanoen.2014.11.050.

(67) Wang, Y.; Yang, Y.; Wang, Z. L. Triboelectric Nanogenerators as Flexible Power Sources. *npj Flex. Electron.* **2017**, *1* (1), 10. https://doi.org/10.1038/s41528-017-0007-8.

(68) Huang, T.; Wang, C.; Yu, H.; Wang, H.; Zhang, Q.; Zhu, M. Human Walking-Driven Wearable All-Fiber Triboelectric Nanogenerator Containing Electrospun Polyvinylidene Fluoride Piezoelectric Nanofibers. *Nano Energy* **2015**, *14*, 226–235. https://doi.org/10.1016/j.nanoen.2015.01.038.

(69) Meng, B.; Cheng, X.; Zhang, X.; Han, M.; Liu, W.; Zhang, H. Single-Friction-Surface Triboelectric Generator with Human Body Conduit. *Appl. Phys. Lett.* **2014**, *104* (10), 103904. https://doi.org/10.1063/1.4868130.

(70) Ma, M.; Kang, Z.; Liao, Q.; Zhang, Q.; Gao, F.; Zhao, X.; Zhang, Z.; Zhang, Y. Development, Applications, and Future Directions of Triboelectric Nanogenerators. *Nano Res.* **2018**, *11* (6), 2951–2969. https://doi.org/10.1007/s12274-018-1997-9.

(71) Pu, X.; Li, L.; Liu, M.; Jiang, C.; Du, C.; Zhao, Z.; Hu, W.; Wang, Z. L. Wearable Self-Charging Power Textile Based on Flexible Yarn Supercapacitors and Fabric Nanogenerators. *Adv. Mater.* **2016**, *28* (1), 98–105. https://doi.org/10.1002/adma.201504403.

(72) Jie, Y.; Jia, X.; Zou, J.; Chen, Y.; Wang, N.; Wang, Z. L.; Cao, X. Natural Leaf Made Triboelectric Nanogenerator for Harvesting Environmental Mechanical Energy. *Adv. Energy Mater.* **2018**, *8* (12), 1703133. https://doi.org/10.1002/aenm.201703133.

(73) Wang, Z. L.; Chen, J.; Lin, L. Progress in Triboelectric Nanogenerators as a New Energy Technology and Self-Powered Sensors. *Energy Environ. Sci.* **2015**, *8* (8), 2250–2282. https://doi.org/10.1039/C5EE01532D.

(74) Wang, Z. L. Triboelectric Nanogenerators as New Energy Technology for Self-Powered Systems and as Active Mechanical and Chemical Sensors. *ACS Nano* **2013**, *7* (11), 9533–9557. https://doi.org/10.1021/nn404614z.

(75) Seung, W.; Gupta, M. K.; Lee, K. Y.; Shin, K.-S.; Lee, J.-H.; Kim, T. Y.; Kim, S.; Lin, J.; Kim, J. H.; Kim, S.-W. Nanopatterned Textile-Based Wearable Triboelectric Nanogenerator. *ACS Nano* **2015**, *9* (4), 3501–3509. https://doi.org/10.1021/nn507221f.

(76) Zhu, G.; Chen, J.; Zhang, T.; Jing, Q.; Wang, Z. L. Radial-Arrayed Rotary Electrification for High Performance Triboelectric Generator. *Nat. Commun.* **2014**, *5* (1), 3426. https://doi.org/10.1038/ncomms4426.

(77) Dong, K.; Wang, Y.-C.; Deng, J.; Dai, Y.; Zhang, S. L.; Zou, H.; Gu, B.; Sun, B.; Wang, Z. L. A Highly Stretchable and Washable All-Yarn-Based Self-Charging Knitting Power Textile Composed of Fiber Triboelectric Nanogenerators and Supercapacitors. *ACS Nano* **2017**, *11* (9), 9490–9499. https://doi.org/10.1021/acsnano.7b05317.

(78) Chen, J.; Guo, H.; He, X.; Liu, G.; Xi, Y.; Shi, H.; Hu, C. Enhancing Performance of Triboelectric Nanogenerator by Filling High Dielectric Nanoparticles into Sponge PDMS Film. *ACS Appl. Mater. Interfaces* **2016**, *8* (1), 736–744. https://doi.org/10.1021/acsami.5b09907.

(79) Kim, I.; Jeon, H.; Kim, D.; You, J.; Kim, D. All-in-One Cellulose Based Triboelectric Nanogenerator for Electronic Paper Using Simple Filtration Process. *Nano Energy* **2018**, *53* (June), 975–981. https://doi.org/10.1016/j.nanoen.2018.09.060.

(80) Wu, C.; Kima, T. W.; Sung, S.; Park, J. H.; Li, F. Ultrasoft and Cuttable Paper-Based Triboelectric Nanogenerators for Mechanical Energy Harvesting. *Nano Energy* **2018**, *44* (November 2017), 279–287. https://doi.org/10.1016/j.nanoen.2017.11.080.

(81) Xia, K.; Zhang, H.; Zhu, Z.; Xu, Z. Folding Triboelectric Nanogenerator on Paper Based on Conductive Ink and Teflon Tape. *Sens. Actuators, A* **2018**, *272*, 28–32. https://doi.org/10.1016/j.sna.2018.01.054.

(82) Zhong, J.; Zhang, Y.; Zhong, Q.; Hu, Q.; Hu, B.; Wang, Z. L.; Zhou, J. Fiber-Based Generator for Wearable Electronics and Mobile Medication. *ACS Nano* **2014**, *8* (6), 6273–6280. https://doi.org/10.1021/nn501732z.

(83) Agcayazi, T.; Chatterjee, K.; Bozkurt, A.; Ghosh, T. K. Flexible Interconnects for Electronic Textiles. *Adv. Mater. Technol.* **2018**, *3* (10), 1700277. https://doi.org/10.1002/admt.201700277.

(84) Holt, B. A.; Gregory, S. A.; Sulchek, T.; Yee, S.; Losego, M. D. Aqueous Zinc Compounds as Residual Antimicrobial Agents for Textiles. *ACS Appl. Mater. Interfaces* **2018**, *10* (9), 7709–7716. https://doi.org/10.1021/acsami.7b15871.

(85) Cui, N.; Liu, J.; Gu, L.; Bai, S.; Chen, X.; Qin, Y. Wearable Triboelectric Generator for Powering the Portable Electronic Devices. *ACS Appl. Mater. Interfaces* **2015**, *7* (33), 18225–18230. https://doi.org/10.1021/am5071688.

(86) Zhao, Z.; Yan, C.; Liu, Z.; Fu, X.; Peng, L.-M.; Hu, Y.; Zheng, Z. Wearable Technology: Machine-Washable Textile Triboelectric Nanogenerators for Effective Human Respiratory Monitoring through Loom Weaving of Metallic Yarns (Adv. Mater. 46/2016). *Adv. Mater.* **2016**, *28* (46), 10266–10266. https://doi.org/10.1002/adma.201670325.

(87) Wagih, M.; Komolafe, A.; Zaghari, B. Dual-Receiver Wearable 6.78 MHz Resonant Inductive Wireless Power Transfer Glove Using Embroidered Textile Coils. *IEEE Access* **2020**, *8*, 24630–24642. https://doi.org/10.1109/ACCESS.2020.2971086.

(88) Heo, E.; Choi, K.-Y.; Kim, J.; Park, J.-H.; Lee, H. A Wearable Textile Antenna for Wireless Power Transfer by Magnetic Resonance. *Text. Res. J.* **2018**, *88* (8), 913–921. https://doi.org/10.1177/0040517517690626.

(89) Chen, Y.; Jie, Y.; Wang, N.; Wang, Z. L.; Cao, X. Novel Wireless Power Transmission Based on Maxwell Displacement Current. *Nano Energy* **2020**, *76*, 105051. https://doi.org/10.1016/j.nanoen.2020.105051.

(90) Thackston, K. A.; Mei, H.; Irazoqui, P. P. Coupling Matrix Synthesis and Impedance-Matching Optimization Method for Magnetic Resonance Coupling Systems. *IEEE Trans. Microw. Theory Tech.* **2018**, *66* (3), 1536–1542. https://doi.org/10.1109/TMTT.2017.2741963.

(91) Bissannagari, M.; Kim, T.-H.; Yook, J.-G.; Kim, J. All Inkjet-Printed Flexible Wireless Power Transfer Module: PI/Ag Hybrid Spiral Coil Built into 3D NiZn-Ferrite Trench Structure with a Resonance Capacitor. *Nano Energy* **2019**, *62*, 645–652. https://doi.org/10.1016/j.nanoen.2019.05.075.

(92) Ortego-Isasa, I.; Benli, K. P.; Casado, F.; Sancho, J. I.; Valderas, D. Topology Analysis of Wireless Power Transfer Systems Manufactured Via Inkjet Printing Technology. *IEEE Trans. Ind. Electron.* **2017**, *64* (10), 7749–7757. https://doi.org/10.1109/TIE.2017.2694355.

(93) Sondhi, K.; Garraud, N.; Alabi, D.; Arnold, D. P.; Garraud, A.; Avuthu, S. G. R.; Fan, Z. H.; Nishida, T. Flexible Screen-Printed Coils for Wireless Power Transfer Using Low-Frequency Magnetic Fields. *J. Micromechanics Microengineering* **2019**, *29* (8), 084006. https://doi.org/10.1088/1361-6439/ab26ff.

(94) Haerinia, M.; Noghanian, S. A Printed Wearable Dual-Band Antenna for Wireless Power Transfer. *Sensors* **2019**, *19* (7), 1732. https://doi.org/10.3390/s19071732.

(95) Kazmi, A.; Rizwan, M.; Sydanheimo, L.; Ukkonen, L.; Virkki, J. A Reliability Study of Coating Materials for Brush-Painted Washable Textile RFID Tags. In *2016 6th Electronic System-Integration Technology Conference (ESTC)*; IEEE, 2016; pp 1–4. https://doi.org/10.1109/ESTC.2016.7764735.

(96) Wen, D.-L.; Liu, X.; Deng, H.-T.; Sun, D.-H.; Qian, H.-Y.; Brugger, J.; Zhang, X.-S. Printed Silk-Fibroin-Based Triboelectric Nanogenerators for Multi-Functional Wearable Sensing. *Nano Energy* **2019**, *66*, 104123. https://doi.org/10.1016/j.nanoen.2019.104123.

(97) He, F.; You, X.; Gong, H.; Yang, Y.; Bai, T.; Wang, W.; Guo, W.; Liu, X.; Ye, M. Stretchable, Biocompatible, and Multifunctional Silk Fibroin-Based Hydrogels toward Wearable Strain/Pressure Sensors and Triboelectric Nanogenerators. *ACS Appl. Mater. Interfaces* **2020**, *12* (5), 6442–6450. https://doi.org/10.1021/acsami.9b19721.

(98) Yin, Z.; Jian, M.; Wang, C.; Xia, K.; Liu, Z.; Wang, Q.; Zhang, M.; Wang, H.; Liang, X.; Liang, X.; et al. Splash-Resistant and Light-Weight Silk-Sheathed Wires for Textile Electronics. *Nano Lett.* **2018**, *18* (11), 7085–7091. https://doi.org/10.1021/acs.nanolett.8b03085.

(99) Yong, J.; Hassan, B.; Liang, Y.; Ganesan, K.; Rajasekharan, R.; Evans, R.; Egan, G.; Kavehei, O.; Li, J.; Chana, G.; et al. A Silk Fibroin Bio-Transient Solution Processable Memristor. *Sci. Rep.* **2017**, *7* (1), 14731. https://doi.org/10.1038/s41598-017-15395-5.

(100) Hawker, M. J.; Guo, C.; Omenetto, F. G.; Kaplan, D. L. Solvent-Free Strategy To Encapsulate Degradable, Implantable Metals in Silk Fibroin. *ACS Appl. Bio Mater.* **2018**, *1* (5), 1677–1686. https://doi.org/10.1021/acsabm.8b00498.

(101) Lu, Q.; Zhang, B.; Li, M.; Zuo, B.; Kaplan, D. L.; Huang, Y.; Zhu, H. Degradation Mechanism and Control of Silk Fibroin. *Biomacromolecules* **2011**, *12* (4), 1080–1086. https://doi.org/10.1021/bm101422j.

(102) Patron, D.; Mongan, W.; Kurzweg, T. P.; Fontecchio, A.; Dion, G.; Anday, E. K.; Dandekar, K. R. On the Use of Knitted Antennas and Inductively Coupled RFID Tags for Wearable Applications. *IEEE Trans. Biomed. Circuits Syst.* **2016**, *10* (6), 1047–1057. https://doi.org/10.1109/TBCAS.2016.2518871.

(103) Wagih, M.; Komolafe, A.; Zaghari, B. Separation-Independent Wearable 6.78 MHz Near-Field Radiative Wireless Power Transfer Using Electrically Small Embroidered Textile Coils. *Energies* **2020**, *13* (3), 528. https://doi.org/10.3390/en13030528.

(104) SUWAHARA, R.; KATO, R.; MURATA, K.; WATANABE, T.; SHIMATANI, Y.; KIRYU, S. A Coil for Wireless Power Transmission by Using Sewing Technique with Litz Wire. *J. Japan Soc. Appl. Electromagn. Mech.* **2019**, *27* (1), 49–54. https://doi.org/10.14243/jsaem.27.49.

(105) Vincent, J.; Rispoli, J. V. Conductive Thread-Based Stretchable and Flexible Radiofrequency Coils for Magnetic Resonance Imaging. *IEEE Trans. Biomed. Eng.* **2019**, *9294* (c), 1–1. https://doi.org/10.1109/TBME.2019.2956682.

(106) Sala de Medeiros, M.; Chanci, D.; Martinez, R. V. Moisture-Insensitive, Self-Powered Paper-Based Flexible Electronics. *Nano Energy* **2020**, *78*, 105301. https://doi.org/10.1016/j.nanoen.2020.105301.

(107) Gao, L.; Chao, L.; Hou, M.; Liang, J.; Chen, Y.; Yu, H.-D.; Huang, W. Flexible, Transparent Nanocellulose Paper-Based Perovskite Solar Cells. *npj Flex. Electron.* **2019**, *3* (1), 4. https://doi.org/10.1038/s41528-019-0048-2.

(108) Li, J.; Yang, H.; Huang, K.; Cao, S.; Ni, Y.; Huang, L.; Chen, L.; Ouyang, X. Conductive Regenerated Cellulose Film as Counter Electrode for Efficient Dye-Sensitized Solar Cells. *Cellulose* **2018**, *25* (9), 5113–5122. https://doi.org/10.1007/s10570-018-1913-1.

(109) Bella, F.; Pugliese, D.; Zolin, L.; Gerbaldi, C. Paper-Based Quasi-Solid Dye-Sensitized Solar Cells. *Electrochim. Acta* **2017**, *237*, 87–93. https://doi.org/10.1016/j.electacta.2017.03.211.

(110) Madaka, R.; Kanneboina, V.; Agarwal, P. Low-Temperature Growth of Amorphous Silicon Films and Direct Fabrication of Solar Cells on Flexible Polyimide and Photo-Paper Substrates. *J. Electron. Mater.* **2018**, *47* (8), 4710–4720. https://doi.org/10.1007/s11664-018-6344-0.

(111) Águas, H.; Mateus, T.; Vicente, A.; Gaspar, D.; Mendes, M. J.; Schmidt, W. A.; Pereira, L.; Fortunato, E.; Martins, R. Thin Film Silicon Photovoltaic Cells on Paper for Flexible Indoor Applications. *Adv. Funct. Mater.* **2015**, *25* (23), 3592–3598. https://doi.org/10.1002/adfm.201500636.

(112) Zhang, K.; Wang, S.; Yang, Y. A One-Structure-Based Piezo-Tribo-Pyro-Photoelectric Effects Coupled Nanogenerator for Simultaneously Scavenging Mechanical, Thermal, and Solar Energies. *Adv. Energy Mater.* **2017**, *7* (6), 1601852. https://doi.org/10.1002/aenm.201601852.

(113) Zhang, G.; Liao, Q.; Zhang, Z.; Liang, Q.; Zhao, Y.; Zheng, X.; Zhang, Y. Novel Piezoelectric Paper-Based Flexible Nanogenerators Composed of $BaTiO_3$ Nanoparticles and Bacterial Cellulose. *Adv. Sci.* **2016**, *3* (2), 1500257. https://doi.org/10.1002/advs.201500257.

(114) Zhang, G.; Liao, Q.; Ma, M.; Gao, F.; Zhang, Z.; Kang, Z.; Zhang, Y. Uniformly Assembled Vanadium Doped ZnO Microflowers/ Bacterial Cellulose Hybrid Paper for Flexible Piezoelectric Nanogenerators and Self-Powered Sensors. *Nano Energy* **2018**, *52*, 501–509. https://doi.org/10.1016/j.nanoen.2018.08.020.

(115) Gao, L.; Zhu, C.; Li, L.; Zhang, C.; Liu, J.; Yu, H.-D.; Huang, W. All Paper-Based Flexible and Wearable Piezoresistive Pressure Sensor. *ACS Appl. Mater. Interfaces* **2019**, *11* (28), 25034–25042. https://doi.org/10.1021/acsami.9b07465.

(116) Pu, X.; Guo, H.; Tang, Q.; Chen, J.; Feng, L.; Liu, G.; Wang, X.; Xi, Y.; Hu, C.; Wang, Z. L. Rotation Sensing and Gesture Control of a Robot Joint via Triboelectric Quantization Sensor. *Nano Energy* **2018**, *54* (September), 453–460. https://doi.org/10.1016/j.nanoen.2018.10.044.

(117) Invernizzi, F.; Dulio, S.; Patrini, M.; Guizzetti, G.; Mustarelli, P. Energy Harvesting from Human Motion: Materials and Techniques. *Chem. Soc. Rev.* **2016**, *45* (20), 5455–5473. https://doi.org/10.1039/C5CS00812C.

(118) Chen, S.; Gao, C.; Tang, W.; Zhu, H.; Han, Y.; Jiang, Q.; Li, T.; Cao, X.; Wang, Z. Self-Powered Cleaning of Air Pollution by Wind Driven Triboelectric Nanogenerator. *Nano Energy* **2015**, *14*, 217–225. https://doi.org/10.1016/j.nanoen.2014.12.013.

(119) Fan, X.; Chen, J.; Yang, J.; Bai, P.; Li, Z.; Wang, Z. L. Ultrathin, Rollable, Paper-Based Triboelectric Nanogenerator for Acoustic Energy Harvesting and Self-Powered Sound Recording. *ACS Nano* **2015**, *9* (4), 4236–4243. https://doi.org/10.1021/acsnano.5b00618.

(120) Cheng, G.-G.; Jiang, S.-Y.; Li, X.; Li, K.; Zhang, Z.-Q.; Ding, J.-N.; Wang, Y.; Yuan, N.-Y. A Contact Electrification Based Wind Generator. *Sens. Actuators, A* **2018**, *280*, 252–260. https://doi.org/10.1016/j.sna.2018.07.043.

(121) Guo, H.; Yeh, M.-H.; Zi, Y.; Wen, Z.; Chen, J.; Liu, G.; Hu, C.; Wang, Z. L. Ultralight Cut-Paper-Based Self-Charging Power Unit for Self-Powered Portable Electronic and Medical Systems. *ACS Nano* **2017**, *11* (5), 4475–4482. https://doi.org/10.1021/acsnano.7b00866.

(122) Han, M.; Zhang, X.; Zhang, H. *Flexible and Stretchable Triboelectric Nanogenerator Devices : Toward Self-Powered Systems*; Wiley-VCH, 2019.

(123) Oyola-Reynoso, S.; Tevis, I. D.; Chen, J.; Chang, B. S.; Çinar, S.; Bloch, J.-F.; Thuo, M. M. Recruiting Physisorbed Water in Surface Polymerization for Bio-Inspired Materials of Tunable Hydrophobicity. *J. Mater. Chem. A* **2016**, *4* (38), 14729–14738. https://doi.org/10.1039/C6TA06446A.

(124) Lessing, J.; Glavan, A. C.; Walker, S. B.; Keplinger, C.; Lewis, J. A.; Whitesides, G. M. Inkjet Printing of Conductive Inks with High Lateral Resolution on Omniphobic "R F Paper" for Paper-Based Electronics and MEMS. *Adv. Mater.* **2014**, *26* (27), 4677–4682. https://doi.org/10.1002/adma.201401053.

(125) Dennerlein, J. T.; Diao, E.; Mote, C. D.; Rempel, D. M. In Vivo Finger Flexor Tendon Force While Tapping on a Keyswitch. *J. Orthop. Res.* **1999**, *17* (2), 178–184. https://doi.org/10.1002/jor.1100170205.

(126) Pu, X.; Tang, Q.; Chen, W.; Huang, Z.; Liu, G.; Zeng, Q.; Chen, J.; Guo, H.; Xin, L.; Hu, C. Flexible Triboelectric 3D Touch Pad with Unit Subdivision Structure for Effective XY Positioning and Pressure Sensing. *Nano Energy* **2020**, *76* (May), 105047. https://doi.org/10.1016/j.nanoen.2020.105047.

(127) Chang, B. S.; Boddupalli, A.; Boyer, A. F.; Orondo, M.; Bloch, J.-F.; Bratlie, K. M.; Thuo, M. M. Effect of Surface Morphologies and Chemistry of Paper on Deposited Collagen. *Appl. Surf. Sci.* **2019**, *484*, 461–469. https://doi.org/10.1016/j.apsusc.2019.04.131.

(128) Oyola-Reynoso, S.; Tevis, I. D.; Chen, J.; Chang, B. S.; Çinar, S.; Bloch, J.-F.; Thuo, M. M. Recruiting Physisorbed Water in Surface Polymerization for Bio-Inspired Materials of Tunable Hydrophobicity. *J. Mater. Chem. A* **2016**, *4* (38), 14729–14738. https://doi.org/10.1039/C6TA06446A.

(129) Glavan, A. C.; Martinez, R. V.; Subramaniam, A. B.; Yoon, H. J.; Nunes, R. M. D.; Lange, H.; Thuo, M. M.; Whitesides, G. M. Omniphobic "R F Paper" Produced by Silanization of Paper with Fluoroalkyltrichlorosilanes. *Adv. Funct. Mater.* **2014**, *24* (1), 60–70. https://doi.org/10.1002/adfm.201300780.

(130) Zhou, Y. S.; Liu, Y.; Zhu, G.; Lin, Z.-H.; Pan, C.; Jing, Q.; Wang, Z. L. In Situ Quantitative Study of Nanoscale Triboelectrification and Patterning. *Nano Lett.* **2013**, *13* (6), 2771–2776. https://doi.org/10.1021/nl401006x.

(131) Glavan, A. C.; Martinez, R. V.; Maxwell, E. J.; Subramaniam, A. B.; Nunes, R. M. D.; Soh, S.; Whitesides, G. M. Rapid Fabrication of Pressure-Driven Open-Channel Microfluidic Devices in Omniphobic RF Paper. *Lab Chip* **2013**, *13* (15), 2922. https://doi.org/10.1039/c3lc50371b.

(132) Yu, Y.; Wang, X. Chemical Modification of Polymer Surfaces for Advanced Triboelectric Nanogenerator Development. *Extrem. Mech. Lett.* **2016**, *9*, 514–530. https://doi.org/10.1016/j.eml.2016.02.019.

(133) Shu Fang, L.; Tsai, C. Y.; Xu, M. H.; Wu, S. W.; Lo, W. C.; Lu, Y. H.; Fuh, Y. K. Hybrid Nano-Textured Nanogenerator and Self-Powered Sensor for on-Skin Triggered Biomechanical Motions. *Nanotechnology* **2020**, *31* (15), 155502. https://doi.org/10.1088/1361-6528/ab6677.

(134) Sala de Medeiros, M.; Chanci, D.; Moreno, C.; Goswami, D.; Martinez, R. V. Waterproof, Breathable, and Antibacterial Self-Powered e-Textiles Based on Omniphobic Triboelectric Nanogenerators. *Adv. Funct. Mater.* **2019**, *29* (42). https://doi.org/10.1002/adfm.201904350.

(135) FDA. *Bacteriological Analytical Manual, Revision A*, 8th Ed.; Food and Drug Administration, 1998.

(136) Lara, H. H.; Ayala-Núñez, N. V.; del Turrent, L. C. I.; Padilla, C. R. Bactericidal Effect of Silver Nanoparticles against Multidrug-Resistant Bacteria. *World J. Microbiol. Biotechnol.* **2010**, *26* (4), 615–621. https://doi.org/10.1007/s11274-009-0211-3.

(137) Nguyen, V.; Yang, R. Effect of Humidity and Pressure on the Triboelectric Nanogenerator. *Nano Energy* **2013**, *2* (5), 604–608. https://doi.org/10.1016/j.nanoen.2013.07.012.

(138) Shen, J.; Li, Z.; Yu, J.; Ding, B. Humidity-Resisting Triboelectric Nanogenerator for High Performance Biomechanical Energy Harvesting. *Nano Energy* **2017**, *40* (August), 282–288. https://doi.org/10.1016/j.nanoen.2017.08.035.

(139) Niu, S.; Liu, Y.; Zhou, Y. S.; Wang, S.; Lin, L.; Wang, Z. L. Optimization of Triboelectric Nanogenerator Charging Systems for Efficient Energy Harvesting and Storage. *IEEE Trans. Electron Devices* **2015**, *62* (2), 641–647. https://doi.org/10.1109/TED.2014.2377728.

(140) Wang, S.; Lin, L.; Wang, Z. L. Nanoscale Triboelectric-Effect-Enabled Energy Conversion for Sustainably Powering Portable Electronics. *Nano Lett.* **2012**, *12* (12), 6339–6346. https://doi.org/10.1021/nl303573d.

(141) Ghomian, T.; Mehraeen, S. Survey of Energy Scavenging for Wearable and Implantable Devices. *Energy* **2019**, *178*, 33–49. https://doi.org/10.1016/j.energy.2019.04.088.

(142) Waterhouse, A.; Leslie, D. C.; Lightbown, K.; Antonoff, D.; Lightbown, S.; Dimitrakakis, N.; Hicks-Berthet, J. B.; Leslie, C. N.; Super, M.; Ingber, D. E.; et al. Rapid Coating Process Generates Omniphobic Dentures in Minutes to Reduce C. Albicans Biofouling. *ACS Biomater. Sci. Eng.* **2019**, *5* (2), 420–424. https://doi.org/10.1021/acsbiomaterials.8b01214.

(143) Xiong, J.; Lin, M.-F.; Wang, J.; Gaw, S. L.; Parida, K.; Lee, P. S. Wearable All-Fabric-Based Triboelectric Generator for Water Energy Harvesting. *Adv. Energy Mater.* **2017**, *7* (21), 1701243. https://doi.org/10.1002/aenm.201701243.

(144) Hasan, J.; Crawford, R. J.; Ivanova, E. P. Antibacterial Surfaces: The Quest for a New Generation of Biomaterials. *Trends Biotechnol.* **2013**, *31* (5), 295–304. https://doi.org/10.1016/j.tibtech.2013.01.017.

(145) Kim, K. N.; Chun, J.; Kim, J. W.; Lee, K. Y.; Park, J.-U.; Kim, S.-W.; Wang, Z. L.; Baik, J. M. Highly Stretchable 2D Fabrics for Wearable Triboelectric Nanogenerator under Harsh Environments. *ACS Nano* **2015**, *9* (6), 6394–6400. https://doi.org/10.1021/acsnano.5b02010.

(146) Schneegass, S.; Amft, O. Introduction to Smart Textiles. In *Introduction to Smart Textiles*; Springer, Cham, 2017; pp 1–15. https://doi.org/10.1007/978-3-319-50124-6_1.

(147) Wang, G.; Wang, L.; Mark, L. H.; Shaayegan, V.; Wang, G.; Li, H.; Zhao, G.; Park, C. B. Ultralow-Threshold and Lightweight Biodegradable Porous PLA/MWCNT with Segregated Conductive Networks for High-Performance Thermal Insulation and Electromagnetic Interference Shielding Applications. *ACS Appl. Mater. Interfaces* **2018**, *10* (1), 1195–1203. https://doi.org/10.1021/acsami.7b14111.

(148) Zuo, B.; Dai, L.; Wu, Z. Analysis of Structure and Properties of Biodegradable Regenerated Silk Fibroin Fibers. *J. Mater. Sci.* **2006**, *41* (11), 3357–3361. https://doi.org/10.1007/s10853-005-5384-z.

(149) Zhu, K.; Tu, H.; Yang, P.; Qiu, C.; Zhang, D.; Lu, A.; Luo, L.; Chen, F.; Liu, X.; Chen, L.; et al. Mechanically Strong Chitin Fibers with Nanofibril Structure, Biocompatibility, and Biodegradability. *Chem. Mater.* **2019**, *31* (6), 2078–2087. https://doi.org/10.1021/acs.chemmater.8b05183.

(150) Rogers, J. A.; Someya, T.; Huang, Y. Materials and Mechanics for Stretchable Electronics. *Science*. March 26, 2010, pp 1603–1607. https://doi.org/10.1126/science.1182383.

(151) Park, S. Il; Shin, G.; McCall, J. G.; Al-Hasani, R.; Norris, A.; Xia, L.; Brenner, D. S.; Noh, K. N.; Bang, S. Y.; Bhatti, D. L.; et al. Stretchable Multichannel Antennas in Soft Wireless Optoelectronic Implants for Optogenetics. *Proc. Natl. Acad. Sci.* **2016**, *113* (50), E8169–E8177. https://doi.org/10.1073/pnas.1611769113.

(152) Xie, Z.; Ji, B.; Huo, Q. Mechanics Design of Stretchable Near Field Communication Antenna With Serpentine Wires. *J. Appl. Mech.* **2018**, *85* (4), 45001–45002. https://doi.org/10.1115/1.4039102.

(153) Park, S. Il; Brenner, D. S.; Shin, G.; Morgan, C. D.; Copits, B. A.; Chung, H. U.; Pullen, M. Y.; Noh, K. N.; Davidson, S.; Oh, S. J.; et al. Soft, Stretchable, Fully Implantable Miniaturized Optoelectronic Systems for Wireless Optogenetics. *Nat. Biotechnol.* **2015**, *33* (12), 1280–1286. https://doi.org/10.1038/nbt.3415.

(154) Wessendorf, A. M.; Newman, D. J. Dynamic Understanding of Human-Skin Movement and Strain-Field Analysis. *IEEE Trans. Biomed. Eng.* **2012**, *59* (12), 3432–3438. https://doi.org/10.1109/TBME.2012.2215859.

(155) Sadri, B.; Goswami, D.; Sala de Medeiros, M.; Pal, A.; Castro, B.; Kuang, S.; Martinez, R. V. Wearable and Implantable Epidermal Paper-Based Electronics. *ACS Appl. Mater. Interfaces* **2018**, *10* (37), 31061–31068. https://doi.org/10.1021/acsami.8b11020.

(156) Eskandarian, L.; Lam, E.; Rupnow, C.; Meghrazi, M. A.; Naguib, H. E. Robust and Multifunctional Conductive Yarns for Biomedical Textile Computing. *ACS Appl. Electron. Mater.* **2020**, *2* (6), 1554–1566. https://doi.org/10.1021/acsaelm.0c00171.

(157) Park, S.-J.; Kim, B.-J. Carbon Fibers and Their Composites. In *Springer Series in Materials Science*; Springer Verlag, 2015; Vol. 210, pp 275–317. https://doi.org/10.1007/978-94-017-9478-7_8.

(158) Liu, Z.; Shang, S.; Chiu, K.; Jiang, S.; Dai, F. Fabrication of Silk Fibroin/Poly(Lactic-Co-Glycolic Acid)/Graphene Oxide Microfiber Mat via Electrospinning for Protective Fabric. *Mater. Sci. Eng. C* **2020**, *107*, 110308. https://doi.org/10.1016/j.msec.2019.110308.

(159) Shrestha, S.; Shrestha, B. K.; Lee, J.; Joong, O. K.; Kim, B.-S.; Park, C. H.; Kim, C. S. A Conducting Neural Interface of Polyurethane/Silk-Functionalized Multiwall Carbon Nanotubes with Enhanced Mechanical Strength for Neuroregeneration. *Mater. Sci. Eng. C* **2019**, *102*, 511–523. https://doi.org/10.1016/j.msec.2019.04.053.

(160) Xu, Z.; Shi, L.; Yang, M.; Zhu, L. Preparation and Biomedical Applications of Silk Fibroin-Nanoparticles Composites with Enhanced Properties - A Review. *Mater. Sci. Eng. C* **2019**, *95*, 302–311. https://doi.org/10.1016/j.msec.2018.11.010.

(161) William J. Chappell, Dohyuk Ha, Henry Mei, P. P. I. Magnetic Resonance Coupling Arrangement. US10044227B2, 2018.

(162) Bailey, W. H.; Harrington, T.; Hirata, A.; Kavet, R. R. O. B.; Keshvari, J.; Klauenberg, B. J.; Legros, A.; Maxson, D. P.; Osepchuk, J. M.; Reilly, J. P.; et al. Synopsis of IEEE Std C95.1™-2019 "IEEE Standard for Safety Levels With Respect to Human Exposure to Electric, Magnetic, and Electromagnetic Fields, 0 Hz to 300 GHz." *IEEE Access* **2019**, *7*, 171346–171356. https://doi.org/10.1109/ACCESS.2019.2954823.

(163) Ghamari, M. A Review on Wearable Photoplethysmography Sensors and Their Potential Future Applications in Health Care. *Int. J. Biosens. Bioelectron.* **2018**, *4* (4), 195. https://doi.org/10.15406/ijbsbe.2018.04.00125.

(164) Hoilett, O. S.; Twibell, A. M.; Srivastava, R.; Linnes, J. C. Kick LL: A Smartwatch for Monitoring Respiration and Heart Rate Using Photoplethysmography. In *2018 40th Annual International Conference of the IEEE Engineering in Medicine and Biology Society (EMBC)*; IEEE, 2018; Vol. 2018-July, pp 3821–3824. https://doi.org/10.1109/EMBC.2018.8513356.

(165) Fujita, D.; Suzuki, A. Evaluation of the Possible Use of PPG Waveform Features Measured at Low Sampling Rate. *IEEE Access* **2019**, *7*, 58361–58367. https://doi.org/10.1109/ACCESS.2019.2914498.

(166) Motin, M. A.; Karmakar, C. K.; Palaniswami, M. PPG Derived Heart Rate Estimation During Intensive Physical Exercise. *IEEE Access* **2019**, *7*, 56062–56069. https://doi.org/10.1109/ACCESS.2019.2913148.

(167) MILLASSEAU, S. C.; KELLY, R. P.; RITTER, J. M.; CHOWIENCZYK, P. J. Determination of Age-Related Increases in Large Artery Stiffness by Digital Pulse Contour Analysis. *Clin. Sci.* **2002**, *103* (4), 371–377. https://doi.org/10.1042/cs1030371.

(168) Botsis, J.; Gmür, T.; Wisnom, M. R.; Pierron, F. Composites Part A: Applied Science and Manufacturing. **2012**. https://doi.org/10.1016/j.compositesa.2012.08.001.

(169) Lipomi, D. J.; Vosgueritchian, M.; Tee, B. C. K.; Hellstrom, S. L.; Lee, J. A.; Fox, C. H.; Bao, Z. Skin-like Pressure and Strain Sensors Based on Transparent Elastic Films of Carbon Nanotubes. *Nat. Nanotechnol.* **2011**, *6* (12), 788–792. https://doi.org/10.1038/nnano.2011.184.

(170) Vincent, J. *Structural Biomaterials: Third Edition*; 2012.

(171) Barman, S. Das; Reza, A. W.; Kumar, N.; Karim, M. E.; Munir, A. B. Wireless Powering by Magnetic Resonant Coupling: Recent Trends in Wireless Power Transfer System and Its Applications. *Renew. Sustain. Energy Rev.* **2015**, *51*, 1525–1552. https://doi.org/10.1016/j.rser.2015.07.031.

(172) Ghamari, M. A Review on Wearable Photoplethysmography Sensors and Their Potential Future Applications in Health Care. *Int. J. Biosens. Bioelectron.* **2018**, *4* (4), 195. https://doi.org/10.15406/ijbsbe.2018.04.00125.

(173) Luebke, T.; DL Wiesemann - US Patent 5, 877,618; 1999, undefined. *Hand Held Non-Contact Voltage Tester*.

(174) Su, C.-I.; Lai, T.-C.; Lu, C.-H.; Liu, Y.-S.; Wu, S.-P. Yarn Formation of Nanofibers Prepared Using Electrospinning. *Fibers Polym.* **2013**, *14* (4), 542–549. https://doi.org/10.1007/s12221-013-0542-4.

(175) Persano, L.; Camposeo, A.; Tekmen, C.; Pisignano, D. Industrial Upscaling of Electrospinning and Applications of Polymer Nanofibers: A Review. *Macromol. Mater. Eng.* **2013**, *298* (5), 504–520. https://doi.org/10.1002/mame.201200290.

PUBLICATIONS

Sala de Medeiros, M., Goswami, D., Chanci, D., Moreno, C., and Martinez, R. V. (**2021**). "Washable, Breathable, and Stretchable e-Textiles Wirelessly Powered by Omniphobic Silk-based Coils." Nano Energy – Accepted.

Sala de Medeiros, M., Daniela Chanci, and Ramses V. Martinez. (**2020**)."Moisture-insensitive, self-powered paper-based flexible electronics." Nano Energy. https://doi.org/10.1016/j.nanoen.2020.105301

Sala de Medeiros, M., Chanci, D., Moreno, C., Goswami, D., and Martinez, R. V. (**2019**). "Waterproof, breathable, and antibacterial self-powered e-textiles based on omniphobic triboelectric nanogenerators." Advanced Functional Materials, 29(42). https://doi.org/10.1002/adfm.201904350

Sadri, B., Goswami, D., **Sala de Medeiros, M.**, Pal, A., Castro, B., Kuang, S., and Martinez, R. V. (**2018**). "Wearable and implantable epidermal paper-based electronics." ACS Applied Materials & Interfaces, 10(37), 31061-31068. https://doi.org/10.1021/acsami.8b11020

Castro, B., **Sala de Medeiros, M.**, Sadri, B., and Martinez, R. V. (**2018**). "Portable and power-free serodiagnosis of Chagas disease using magnetic levitating microbeads." Analyst, 143(18). https://doi.org/10.1039/C8AN01374H